Università degli Studi di Ferrara

DOTTORATO DI RICERCA IN FISICA

CICLO XXVIII

COORDINATORE Prof. Guidi Vincenzo

LAUE LENSES TO FOCUS X- AND GAMMA-RAY BEAMS FOR MEDICAL APPLICATIONS

Settore Scientifico Disciplinare FIS/01

Dottorando
Dott. Paternò Gianfranco

Tutore
Prof. Guidi Vincenzo

Anni 2013/2015

Articles published during the Ph.D. which this thesis relies on.

I G. Paternò, V. Bellucci, R. Camattari and V. Guidi - *Design study of a Laue lens for nuclear medicine* - Journal of Applied Crystallography (2015) 48:125-137, 10.1107/S1600576714026235

II G. Paternò, M. Marziani, R. Camattari V. Bellucci, A. Mazzolari, M. Gambaccini and V. Guidi - *Laue lens to focus an X-ray beam for radiation therapy* - in press in Journal of Applied Crystallography (2016)

III R. Camattari, G. Paternò, A. Battelli, V. Bellucci, P. Bastie and V. Guidi - *High-efficiency focusing of hard X-rays exploiting the quasi-mosaic effect in a bent germanium crystal* - Journal of Applied Crystallography (2014) 47:799-802, 10.1107/S1600576714005056

IV A. Mazzolari, R. Camattari, V. Bellucci, G. Paternò, C. Scian, G. Mattei and V. Guidi - *Manufacturing of advanced bent crystals for Laue Optics for Gamma ObservationS (LOGOS)* - Nuclear Instruments and Methods in Physics Research B 355 (2015) 297-300, http://dx.doi.org/10.1016/j.nimb.2015.03.048

V V. Bellucci, R. Camattari, V. Guidi, A. Mazzolari, G. Paternò, G. Mattei, C. Scian and L. Lanzoni - *Ion implantation for manufacturing bent and periodically bent crystals* - Applied Physics Letters 107, 064102 (2015), http://dx.doi.org/10.1063/1.4928553

VI R. Camattari, G. Paternò, V. Bellucci, A. Mazzolari, M. Romagnoni, and V. Guidi - *Optical elements for hard X-rays based on sandblasting* - submitted to Journal of Applied Crystallography (2016)

Articles published during the Ph.D. as side products of this thesis.

- R. Camattari, G. Paternò, V. Bellucci and V. Guidi - *Quasi-mosaicity of (311) planes in silicon and its usage in a high-focusing Laue lens* - Experimental Astronomy (2014) 38:417-431, 10.1007/s10686-014-9429-7

- R. Camattari, G. Paternò, V. Bellucci, V. Guidi, M. Jentschel and P. Bastie - *High-efficiency diffraction and focusing of X-rays through asymmetric bent crystalline planes* - Journal of Applied Crystallography (2015) 48:297-300, 10.1107/S1600576714024960

Contents

Introduction

Cancer is a leading cause of death worldwide, accounting for 8.2 million deaths in 2012 [1]. Cancer mortality can be reduced if cases are detected and treated early. Some of the most common cancer types, such as breast cancer, cervical cancer, oral cancer and colorectal cancer have high cure rates when detected early and treated according to best practices. However, a tumour in a early stage of evolution has a very small size and could be located near radiosensitive organs. Therefore, high-resolution techniques are required to accurately detect and effectively treat such small tumours.

Going deeper in understanding the processes of carcinogenesis would represent a further step forward in the fight against cancer. A non-invasive imaging system that allows in vivo assessment of biological and biomolecular interactions would permit to get insight into the complex events contributing to the induction of DNA damage, repair, mutagenesis, and carcinogenesis [2]. While these kind of studies can be performed using conventional radionuclide imaging techniques such as single-photon emission tomography (SPECT) and positron emission tomography (PET), these techniques are inherently limited to spatial resolutions of 1-2 mm [3]. The image resolution could be increased by using an optics capable of focusing the γ-ray emitted by radionuclides. As the index of refraction of all materials is $\lesssim 1$ for high-energy photons, common refractive optics can not be used [4]. A possible solution is to exploit the total external reflection of γ-rays that take place when they impinge on the surface of a medium at a small glancing angle. A radionuclide imaging system based on such kind of reflective optics was developed for small animals [5, 6]. This device is theoretically capable of achieving sub-millimetre spatial resolution with 1×10^{-5} efficiency for γ-photons at 27.5 keV emitted by ^{125}I. However, since the critical angle for total reflection is inversely proportional to the photon energy and a medical device has to be as compact as possible, this approach is not suitable for performing radionuclide studies exploiting γ-lines at higher energy, such as the intense line at 140.5 keV emitted by the ^{99m}Tc, which is the most used general purpose radioisotope.

A Laue lens is an optics potentially capable of overcoming this limit. It is composed of an

ensemble of crystals, usually disposed as concentric rings, that exploit Bragg diffraction in Laue configuration to focus a relatively large number of the photons emitted by a high-energy source into a small focal spot [7]. Due to focusing, a precise mapping of the radioactivity distribution inside a small volume can be obtained. Therefore, this device could be exploited to perform high-resolution radionuclide imaging both for small-animals and humans.

The same optical device can be also used for treating tumour through radiotherapy. Radiotherapy consists in imparting a radiation dose to a target volume in order to destroy cancer cells. Any radiotherapy treatment aims to maximize the dose to the tumour, minimizing at the same time the irradiation of neighbouring healthy tissues. Among radiotherapy treatments, hadron therapy uses charged particles beams, namely protons or positive ions, to achieve the aforementioned goal. Indeed, they have a finite range of penetration in a tissue and a high amount of energy released at the end of their track. However, hadron therapy is not easily available, because it requires very large investments in equipment and huge machines [8]. Thus, only a limited number of patients can access to the high-quality treatment provided by hadron therapy. Conventional radiotherapy is more accessible since it relies on compact electron linear accelerator producing photon beams in the MeV energy range to reach the tumour and spare the skin. However, such technique is not comparable with the hadron therapy in terms of dose deposition accuracy. A device capable of focusing X-rays would allow concentrating the dose toward the tumour sparing at the same time the surrounding normal tissues. Indeed, due to focusing, the photon flux would increase with the penetration depth and would reach the maximum at the focal point. The combination of this effect with the photon absorption by the tissues would give rise to a depth-dose profile showing a pronounced peak at the focal depth and a rather rapid fall-off beyond this point. This dose distribution is somewhat similar to that achievable with hadron therapy. The phenomenon of diffraction occurring in the crystals composing a Laue lens can be exploited to focus an X-ray beam. In particular, it is possible to use a conventional X-ray tube with peak voltage up to 250 kV as a source of radiation and exploit a Laue lens to concentrate as much radiation as possible toward the focal point of the lens, where the tumour mass is located. Thus, it would be possible to reach a high precision in the dose delivery with an equipment orders of magnitude less expensive if compared to the cost of a facility for hadron therapy and even less expensive than the equipment for traditional radiotherapy based on MeV X-ray beams.

The work presented in this thesis concerns the study and the realization of Laue lenses devoted to medical applications. The thesis is divided into 5 chapters plus 2 appendices. The first chapter deals with the basic concepts of diffraction of high-energy radiation in

various types of crystals, i.e., perfect, mosaic, and curved diffracting planes (CDP) crystals. The second chapter contains an overview of the usage of bent crystals in modern physics and of the techniques used to fabricate them. Some innovative bending methods developed at the Sensor and Semiconductor Laboratory (SSL) of Ferrara in the framework of the INFN-LOGOS project are described in detail. Furthermore, an experiment devoted to the demonstration of the focusing capabilities of a bent crystal is described. In the third chapter, a detailed study and the design principles of a Laue lens for nuclear medicine are presented. The study was carried out through a specifically written ray tracer, called LAUENM. The imaging capabilities of the designed lenses were assessed with diverse configurations of the source. In these cases, the images recorded by a real detector were simulated. The fourth chapter aims to demonstrate the effectiveness and versatility of a system for radiation therapy based on a Laue lens. Two series of simulations were carried out. The first series was performed employing a custom made Monte Carlo software, called LAUETHER to calculate the phase space of the diffracted photons in a plane at an arbitrary distance from the lens. The second series of simulations was performed through GAMOS, a Monte Carlo particle tracking code, to calculate the dose distribution inside a voxelized water phantom due to the beam diffracted by a proposed Laue lens. Various conditions of irradiation were considered. The fifth chapter is dedicated to describe a first prototype of Laue lens for radiotherapy developed at the SSL. The result of an experimental test performed at the LARIX laboratory of Ferrara is also shown and a comparison with the simulations is given. In Appendix A, a brief treatment of the theory of linear elasticity is provided. Appendix B contains a description of the algorithms used in the LAUENM code and the demonstration of the focusing/defocusing properties of CDP crystals.

Chapter 1

Diffraction of high-energy radiation in crystals

1.1 Structure of crystals

An ideal crystal can be viewed as the infinite repetition of identical structural units, called *basis*. The spatial distribution of the basis can be described through a set of points called *lattice*. It is possible to define the lattice using three vectors, $\boldsymbol{a_1}\ \boldsymbol{a_2}\ \boldsymbol{a_3}$, such that the arrangement of the atoms in the crystal is the same when viewed at the point $\boldsymbol{r}$ or at each point $\boldsymbol{r'}$,

$$\boldsymbol{r'} = \boldsymbol{r} + u_1\boldsymbol{a_1} + u_2\boldsymbol{a_2} + u_3\boldsymbol{a_3}, \tag{1.1}$$

where $u_1\ u_2\ u_3$ are three arbitrary integer numbers. Vectors $\boldsymbol{a_i}$ represent the *lattice constants*. The volume built on these vectors is called *unit cell*. The unit cell is therefore the smallest unit of volume that contains all of the structural and symmetry information to build-up the macroscopic structure of the lattice by translation. The positions of the atoms inside the unit cell are described by the set of atomic positions measured from a lattice point. Lattice and base define the crystal, as the basis indicates the positions occupied by different atoms in the cell and their type, while the reticle provides the information on the periodicity of the crystal. The fundamental characteristic of crystals is their invariance, for appropriate translations and rotations, of their physical properties, such as the optical, chemical, electrical, and elastic properties. The space group that identifies each type of crystal defines these degrees of freedom. Base and lattice are not uniquely defined, there are endless equivalent combinations to describe the same crystal. A cell is called *primitive* if it contains only one lattice point.

Silicon and germanium have the crystalline structure of the diamond, which is based on

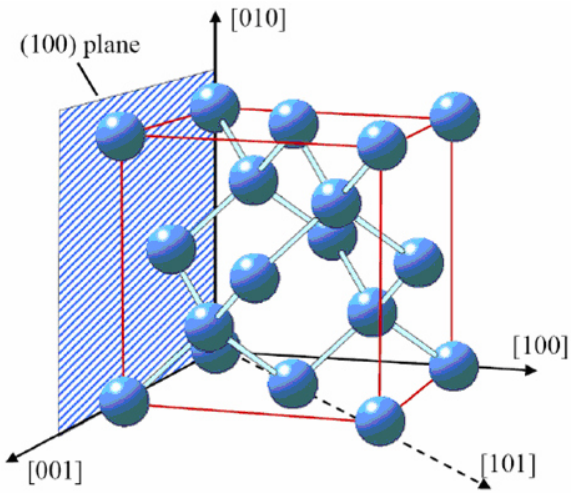

Figure 1.1: Conventional cubic cell of silicon.

the tetrahedral bond between the atoms of the crystal. Each atom forms covalent bonds with 4 identical neighbouring atoms. The bonds are characterized by the same length and angular separation and define a tetrahedral structure. However, such type of structure involves some of the features of the cubic symmetry. Indeed, it can be described through a face-centred cubic (fcc) lattice with bi-atomic basis composed of identical atoms positioned at the point of coordinates (0,0,0) and (a/4,a/4,a/4), where a is the lattice constant (5.43 $\mathring{A}$ for Si) and identifies the side of the *conventional cubic cell* (Fig. 1.1). This crystalline structure can also be represented as two interpenetrating fcc lattices shifted with respect to one another by the vector (a/4,a/4,a/4).

The crystallographic directions and planes are fictitious entities that connect the atoms in a crystal. Depending on the density of atoms and on the type of bonds, the chemical-physical properties may change along different directions and planes. Directions and planes can be identified within a crystal through three integers hkl, called *Miller indices*. They are defined as the reciprocals of the fractional intercepts which the lattice plane makes with the vector defining the conventional cell. If we consider a crystal with a cubic conventional cell and the planes make intercepts of a/h, a/k, a/l with the axes, then the Miller indices of that plane are (hkl), written in parentheses. If a plane is parallel to a given axis, its fractional intercept on that axis goes to infinity and the corresponding Miller index is taken as zero. If a fractional intercept is negative, it is labeled with an overlined symbol. If the Miller indices $[hkl]$ are shown in square brackets, they give the direction of a vector orthogonal of the plane with the same indices. As an example, in Fig. 1.1 a lattice plane and some directions are shown.

1.2 Generalities on diffraction in crystals

X- and γ-ray diffraction is a coherent effect carried out by parallel atomic planes within a crystalline material. Incident photons are scattered by the electrons in the crystal. Reflected waves interfere constructively, giving rise to a diffracted beam, provided that their paths through the crystal leads to a phase shift which is multiple of the wavelength. This condition occurs if the Bragg's law is satisfied:

$$2d_{hkl}sin\theta_B = \lambda, \tag{1.2}$$

where d_{hkl} is the spacing between atomic planes, θ_B the angle subtended by the incoming photon trajectory and the diffracting lattice planes, and λ the wavelength of the radiation. The Bragg angle, θ_B, depends on the orientation of the lattice planes. Indeed, for a crystal having a cubic conventional cell, such as Cu, GaAs, Si, or Ge, the spacing between planes can be expressed as

$$d_{hkl} = \frac{a}{\sqrt{h^2 + k^2 + l^2}}, \tag{1.3}$$

where a is the lattice constant of the crystal and h, k, l are the Miller indices of the planes. Since $\lambda = h_p c/E$, where h_p is the Planck's constant, c the speed of light in vacuum, and E the energy of the radiation, by combining equations (1.2) and (1.3), it follows

$$sin\theta_B = \frac{h_p c\sqrt{h^2 + k^2 + l^2}}{2aE}. \tag{1.4}$$

Two diffraction geometries are possible. In the first case, called Bragg (reflection) geometry and depicted in Fig. 1.2.a, the diffracted beam comes out from the same crystal surface on which the incident beam impinges. Conversely, in the Laue (transmission) geometry, depicted in Fig. 1.2.b, the diffracted beam comes out from the surface opposite to that onto which the incident beam impinges. For high-energy photons, such as those emitted by a radiotracer, the Bragg angle is very small and the crystal has to be large to diffract even a small-size beam. For this reason, the Laue geometry represents a more convenient choice.

1.3 Diffraction in perfect crystals

The diffracted beam intensity depends on the crystal features and can be obtained from the dynamical theory or from the kinematic theory of diffraction [9]. The dynamical theory, as developed by Darwin, takes into account the interaction of X-rays with matter by solving recurrence equations that describe the balance of partially transmitted and partially reflected

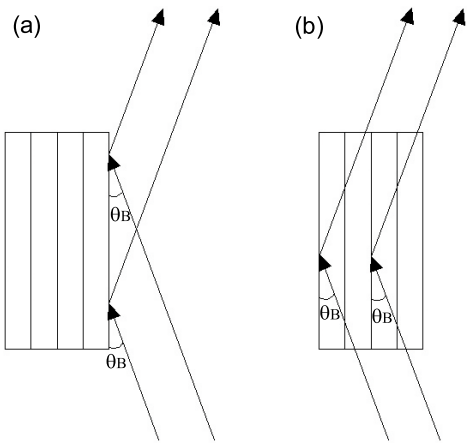

Figure 1.2: Diffraction geometries. a) Bragg geometry: the diffracted beam comes out from the same crystal surface on which the incident beam impinges. b) Laue geometry: the diffracted beam comes out from the surface opposite to that on which the incident beam impinges.

waves at each lattice plane [10, 11]. On the contrary, the kinematic theory assumes that each photon is scattered only once. The total diffracted amplitude is simply obtained by adding the individual amplitudes diffracted by each diffracting centre, taking into account only the geometrical phase differences between them and neglecting the interaction of the radiation with matter. Even if the kinematic theory is less rigorous than the dynamical theory, it gives correct results when a thin perfect crystal or a highly-distorted crystal is considered. An exhaustive treatment of the subject, in both perfect and distorted crystals, can be found in specialized books [4] or in review articles [12, 13, 14]. Here, only the concepts that are relevant for the study of a Laue lens are recalled.

The *reflectivity* of a crystal is defined as the ratio of the diffracted beam intensity over the incident beam intensity. Instead, *diffraction efficiency* is defined as the ratio of the diffracted beam intensity over the transmitted beam intensity when no diffraction occurs.

For a radiation of energy E and a crystal with lattice planes (hkl), equation (1.4) provides the incidence angle θ at which diffraction occurs. Actually, both kinematic and dynamical theories predict a range around the Bragg angle θ_B for which the intensity of the diffracted beam is different from zero. If we consider a perfect crystal under Laue symmetrical geometry[1], the *rocking curve*, i.e. the reflectivity (or the diffraction efficiency) plotted as a function of $\Delta\theta = \theta - \theta_B$ shows a narrow peak (see Fig. 1.3). Its width at Half Maximum (FWHM) is called *Darwin width* δ

$$\delta = 2\frac{d_{hkl}}{\Lambda_0}, \tag{1.5}$$

[1]In Laue symmetrical geometry, the angle between the lattice plane and the crystal surface is exactly 90°.

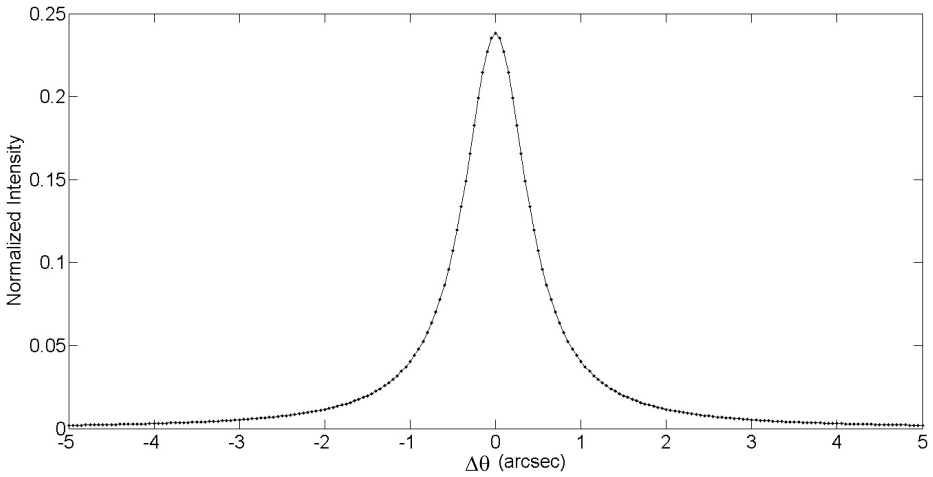

Figure 1.3: Rocking curves for flat Ge crystal with a thickness of 1 mm and using (111) lattice planes to diffract 140.5 keV photons.

where Λ_0 is defined as the *extinction length*

$$\Lambda_0 = \frac{\pi V_c \cos\theta_B}{r_e \lambda |C||F_{hkl}|}, \tag{1.6}$$

V_c being the volume of the crystal elementary cell ($V_c = a^3$ for a cubic cell), r_e the classical electron radius, λ the wavelength of the radiation, C the polarization factor, and F_{hkl} the structure factor. For an unpolarized beam, the polarization factor is $C = (1 + \cos^2\theta_B)/2$. The structure factor quantifies the scattering efficiency of an elementary cell of the crystal, by taking into account the repartition of electrons in space and the vibration of lattice ions via the so-called Debye-Waller factor [15].

The Darwin width defines the angular acceptance of a flat crystal, as well as the energy bandwidth since Bragg's law, under small-angle approximation, gives an inverse proportionality between diffraction angle and photon energy. At the energies of interest for medical applications (50 - 250 keV), typical values for δ are of the order of 1 arcsec. Furthermore, because of the re-diffraction of the beam, the diffraction efficiency of a thick flat crystal can be expressed as

$$\eta_D = \frac{1}{2(1 + (2\Delta\theta/\delta))^2}, \tag{1.7}$$

therefore the reflectivity of a thick flat crystal is pinned to 1/2 [9]. A crystal can be regarded as thick if $T_0 \gg \Lambda_0$, T_0 being the thickness of crystal traversed by radiation. Since in our case Λ_0 is small, this condition is almost always fulfilled. The integrated reflectivity is the integral of the reflectivity over the angular acceptance (and energy bandwidth) of the crystal [16]. Since this quantity results to be very poor for a flat perfect crystal, different types of crystals have been considered by the scientific community for the applications and in

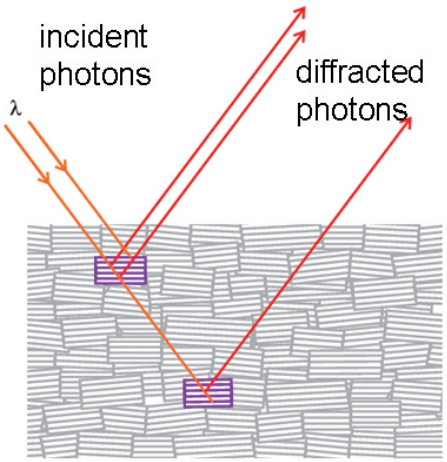

Figure 1.4: Sketch of a mosaic crystal.

particular for the realization of a Laue lens. Their features are summarized in the next sections.

1.4 Diffraction in mosaic crystals

Unlike an ideal crystal, a real crystal presents imperfections due to its growth condition, and it can be better modeled through the Darwin's Model [15]. This model, known also as mosaic model, regards the crystal as an ensemble of microscopic ideal crystals, the crystallites, slightly misaligned to each other (see Fig. 1.4) according to an angular distribution, which is usually a Gaussian function

$$W(\Delta\theta) = 2\sqrt{\frac{\ln 2}{\pi}}\frac{1}{m}e^{-\ln 2(\frac{\Delta\theta}{m/2})^2}. \tag{1.8}$$

The FWHM of this distribution m is called *mosaicity*, or mosaic spread, of the crystal. The reflectivity, under symmetric Laue condition, is

$$R = \frac{1}{2}(1 - e^{2\sigma T_0})e^{-\mu T_0/\cos\theta_B}, \tag{1.9}$$

T_0 being the thickness traversed by the beam, μ the linear absorption coefficient of the crystal, and

$$\sigma = W(\Delta\theta)Q. \tag{1.10}$$

Q is the integrated intensity diffracted by an individual crystallite per unit of thickness. From the dynamical theory of diffraction, Q can be written as

$$Q = \frac{\pi^2 d_{hkl}}{\Lambda_0^2 \cos\theta_B} f(A). \tag{1.11}$$

Under small-angle approximation, which is valid above 100 keV, the function $f(A)$ can be written as

$$f(A) = \frac{2I_0(2A)}{2A}. \tag{1.12}$$

I_0 is the integral, from 0 to $2A$, of zero-order Bessel function. A is defined as

$$A = \frac{\pi t_0}{\Lambda_0 \cos\theta_B}, \tag{1.13}$$

t_0 being the thickness of crystallites. $f(A)$ is approximately 1, which is its maximum value, when $t_0 \ll \Lambda_0$, namely when the dynamical theory tends to the kinematic theory.

The reflectivity of a mosaic crystal is the product of two terms. The first one is the diffraction efficiency of the crystal, the second one takes into account the absorption of the beam. As can be seen by the equation (1.9), reflectivity peaks at $\Delta\theta = 0$. The peak height is at most 1/2 as in the case of a perfect crystal.

The FWHM of the rocking curve, Ω, is proportional to the mosaicity of the crystal and can be written as

$$\Omega = m\sqrt{\frac{-\ln(-\frac{1}{\alpha}\ln(\frac{1}{2}(1+e^{-\alpha})))}{\ln 2}}, \tag{1.14}$$

where α is a dimensionless coefficient given by

$$\alpha = 4\pi^2\sqrt{\frac{\ln 2}{\pi}}\frac{d_{hkl}T_0}{\Lambda_0^2 m}. \tag{1.15}$$

Even though peak reflectivity is at most 1/2, a mosaic crystal with large mosaicity (it can be several tens of arcsec) may exhibit a large integrated reflectivity. For this reason, such crystals were chosen for the realization of the first prototypes of Laue lens for nuclear medicine [17, 18].

1.5 Diffraction in crystals with curved diffracting planes

Another type of crystal is the so-called Curved Diffracting Planes (CDP) crystal. In a CDP crystal, a stress induces a curvature in the whole lattice structure according to the elastic properties of the material. Due to the curvature, there is an angular dispersion of

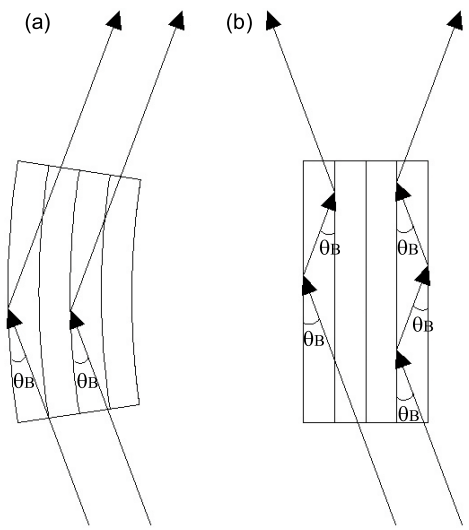

Figure 1.5: Diffraction in CDP and perfect crystals. a) In a CDP crystal, due to the continuous change of the incident angle, re-diffraction is unlikely. b) In a perfect crystal the beam is reflected many times, limiting the reflectivity to 50%.

the lattice planes within the crystal. The continuous change in the orientation of the lattice planes makes it unlikely to have re-diffraction inside the crystal and the reflectivity limit of 50% disappears (Fig. 1.5). Thus, CDP crystals have the potential to achieve a better performance with respect to both perfect and mosaic crystals.

There are many ways to fabricate a CDP. The easiest one is by means of an external device (holder) that applies a bending moment to the crystal [19]. This method has been in use since decades for the realization of high-efficiency monochromators employed in synchrotron high-energy X-ray beamlines [20, 21]. However, the use of a holder implies additional weight and space-occupation. These problems represent a severe limitation to the use of such a crystal as a component of a Laue lens for medical applications. Thus, the crystal curvature is required to be self-standing. For this purpose, various methods have been proposed by the scientific community. An overview of the most used and the most innovative techniques are reported in chapter 2.

Diffraction in curved crystal can be studied through Takagi-Taupin's equations [22, 23]. They are hyperbolic partial derivative equations obtained from Maxwell's equations in a deformed periodic medium. In the general case, these equations cannot be solved explicitly and a numerical approach has to be used. Alternatively, for slightly curved crystal, the so-called PPK theory can be adopted. Such theory, based on geometrical optics principles, has been developed independently by Penning and Polder [24], and by Kato [25]. In the

PPK theory the distortion of the diffracting planes is described by the strain gradient β,

$$\beta = \frac{\Lambda_0}{cos^2\theta_B}\frac{\partial^2(\mathbf{h}\cdot\mathbf{u})}{\partial s_0 \partial s_h}, \tag{1.16}$$

where s_0 and s_h are units vectors, parallel to the incident and to the diffracted beams respectively. $\mathbf{h}$ is the reciprocal lattice vector of the reflection hkl and $\mathbf{u}$ the displacement vector. If the curvature of a crystal is uniform, it is possible to demonstrate [26] that the strain gradient assumes the simpler form

$$\beta = \frac{\Omega}{T_0\delta/2}, \tag{1.17}$$

Ω being the angular distribution of the lattice planes, T_0 the thickness of the crystal, and δ the Darwin width given by equation (1.5). The angular distribution of the lattice plane is directly proportional to the crystal curvature. Indeed, it is

$$\Omega = \frac{T_0}{R_C}, \tag{1.18}$$

where R_C is the radius of curvature of the crystal.

The rocking curve of a curved crystal follows a rectangular distribution with width Ω. The height of the plateau, which corresponds to the peak reflectivity, depends on the curvature of the diffracting planes as well. In the general case, reflectivity cannot be expressed in a closed-form. However, for a highly-curved crystal, an extension of the PPK theory exists that provides the reflectivity under Laue symmetric condition for diffraction [26]. It holds

$$R = (1 - e^{\frac{-\pi^2 d_{hkl}}{\Lambda_0^2}\frac{T_0}{\Omega}})e^{-\frac{\mu T_0}{\cos\theta_B}}. \tag{1.19}$$

A crystal can be regarded as highly-curved when the following condition for the strain gradient is met

$$\beta > \beta_c = \frac{\pi}{2\Lambda_0}. \tag{1.20}$$

Such condition is fulfilled if the radius of curvature of the diffracting planes R_C is smaller than the critical value $R_{C_c} = 4\Lambda_0/\pi\delta$.

If $R_C > R_{C_c}$, a multi-lamellar model can be used for the calculation of the crystal diffraction efficiency [27]. A multi-lamellar model which takes into account the re-diffraction of the beam is reported in [28]. Such model merges the results provided by equation (1.19) for highly-curved crystals with the results provided by the dynamical theory for flat thick crystals.

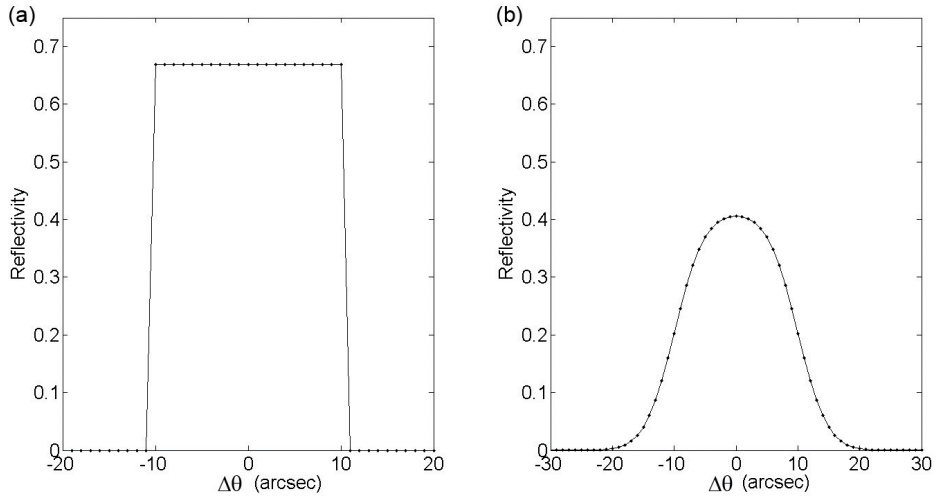

Figure 1.6: Theoretical rocking curves for a mosaic and a CDP Ge crystal with the same thickness $T_0 = 1$ mm and angular acceptance $\Omega = 20$ arcsec and using (111) lattice planes to diffract 140.5 keV photons. a) CDP crystal with radius of curvature $R_C = 10.3$ m. b) Mosaic crystal with mosaicity $m = 13.6$ arcsec.

In Fig. 1.6 the rocking curves for a mosaic and a CDP crystal with the same angular acceptance are compared. Peak reflectivity of a CDP crystal, as calculated by equation (1.19), does not suffer from the 50% limitation. Hence, CDP crystals can have a very high integrated reflectivity, resulting very good candidates for the realization of a Laue lens.

Chapter 2

Usage and fabrication of bent crystals

2.1 Usage of bent crystals

Manufacturing and development of bent crystals are making progress in different physical fields. Indeed, bent crystals can be used as optical elements for neutron, X- and γ-rays as well as optical elements for the manipulation of charged particle beams. In fact, by exploiting diffraction of high-energy radiation in bent crystals, many modern applications and tools have been developed, such as monochromators for X-ray beamlines [20], hard X-ray focusing system for astrophysical [29] and nuclear medicine [18] purposes, and neutron beam controller with wide angular acceptance [30]. On the other hand, owing to the strong electric field generated by ordered atoms in a bent crystal, it is possible to manipulate charged particle trajectories via coherent effects such as channeling and volume reflection [31, 32]. Bent crystals have already been proposed to be used in collimation systems [33], for beam steering [34], and extraction [35]. Radiation emission due to curved trajectories of charged particles in bent crystals was studied in order to yield photon production through bremsstrahlung, channeling radiation, parametric X-ray radiation (PXR), and undulator use [36].

2.1.1 Bending techniques

In sight of the great interest by these scientific communities, several techniques for producing proper curved crystals have been developed, each of which has positive and negative aspects. One of the first methods that was used for bending consists is the use of a mechanical mean, i.e., by deforming a crystal through an external device [19, 37]. Using an holder

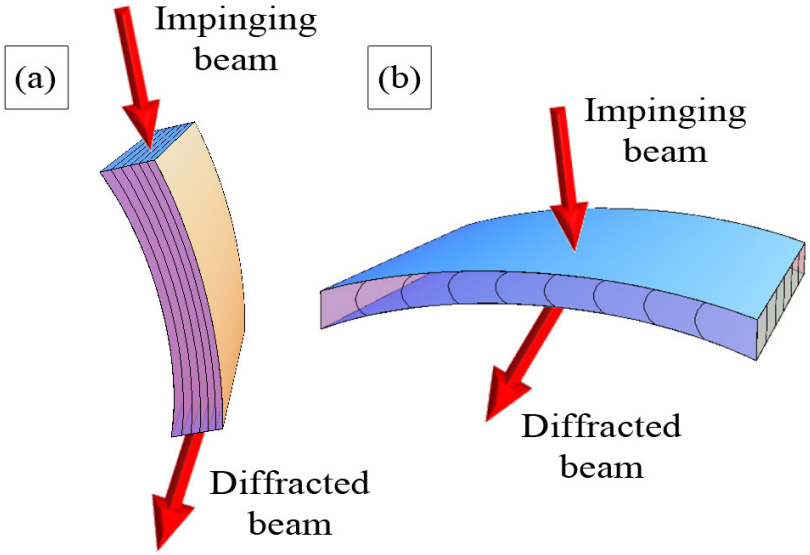

Figure 2.1: (a) geometry 1. (b) geometry 2. Red arrows represent an X-ray beam. Courtesy of Camattari [43].

for bending can be an optimal solution unless there are limitations due to constraints as encumbrance, weight, or miniaturization. In such latter cases, self-standing bent crystals are mandatory. A self-standing bent crystal can be obtained by applying a thermal gradient to a perfect crystal [38]. A bent crystal can also be obtained by concentration-gradient techniques, i.e. by growing a two-component crystal with graded composition along the growth axis [39]. These techniques have reported good results during experiments; however, such bent crystals are not easy to manufacture, thus they are not suitable for mass production. A self-standing curved crystal can be obtained by a controlled surface damage through a mechanical process performed on one side of a crystal, such as the lapping process [40] and the "grooving method" [41]. These technique are suitable for mass production, but cause non-negligible damage in the crystals.

Within the frame of the INFN-LOGOS project, various new approaches have been developed at Sensor and Semiconductor Laboratory (SSL) of Ferrara to fabricate self-standing bent crystals. The most promising for the realization of optical elements for a Laue lens are based on carbon fibre deposition, ion implantation and sandblasting. The details of these method are exposed in the next section. Before that, the concept of quasi-mosaicity is introduced, because of its importance in modern physics [42].

2.1.2 CDP and quasi-mosaic crystals

Crystals with curved diffracting planes can be exploited to diffract a photon beam in Laue condition according to two different configurations. In the first one, shown in Fig.

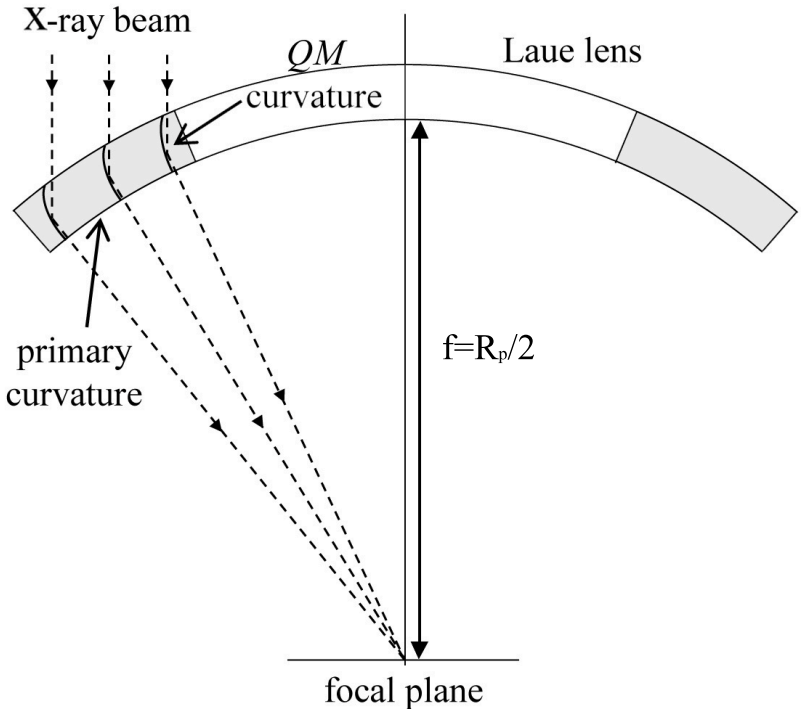

Figure 2.2: Schematic representation of a cross section of a Laue lens based on QM crystals. Gray rectangles represent the crystals. The primary curvature leads to a secondary curvature of the planes affected by quasi-mosaicity. In this configuration the QM diffracting planes are perpendicular to the main surface of the plates. The primary curvature allows focusing diffracted radiation onto the focal plane, while the QM curvature increases the integrated diffraction efficiency. Courtesy of Camattari [43].

2.1.a and called *geometry 1*, the crystals are oriented with their major faces "parallel" to the photon direction and are bent directly along the side traversed by the photon beam. In the second configuration, shown in Fig. 2.1.b and called *geometry 2*, the samples expose their largest surface to the photon flux. In this case, the curvature of the diffracting planes is obtained exploiting the quasi-mosaic (QM) effect, which is an effect due to the crystal elastic anisotropy. Under very specific orientations, as a crystal is bent to a primary curvature by external forces, another curvature (secondary curvature) arises within the crystal, i.e., the QM curvature [44]. This effect is fully explained by the theory of linear elasticity in an anisotropic medium, a brief treatment of which is presented in Appendix A. Crystals exploiting planes bent through the QM effect to diffract a photon beam are called "QM crystals".

A Laue lens composed of QM crystals is an arrangement of curved plates whose primary curvature lies on a spherical cap of radius R_P, while the QM curvature allows diffraction with CDPs. Due to Bragg diffraction, focusing of each QM sample converges on a focal spot at a distance $f = R_P/2$ on the symmetry axes of the cap (see Fig. 2.2). This types of Laue

lens is best suited for an astrophysical application. In fact, in this case, the focal length f is of the order of tens of meters and the external radius of the lens can reach a few meters. As consequence, the use of CDP crystals in geometry 1 would require the fabrication and the setting up of a large number of such crystals to cover the whole lens. Quasi-mosaicity allows the focusing of the photon flux in a spot smaller than the crystal size. For a quasi-mosaic crystal, the primary curvature is responsible for focusing, while the secondary (QM) curvature increases the diffraction efficiency [45]. Thus, since the secondary curvature can control the size of the focal spot, QM crystals allow focusing with high resolution. As a result, the sensitivity of a Laue lens devoted to astrophysics could be increased [46]. In medical applications, the transversal size of the crystals has to be small because of the short focal length and therefore, Laue lenses are generally envisaged to exploit CDP crystals in geometry 1. Indeed, in chapters 3 and 4, which deal with the design study of Laue lenses for nuclear medicine and radiotherapy respectively, geometry 1 is implicitly assumed. However, in chapter 5, a prototype of Laue lens for radiotherapy exploiting QM Si crystals (geometry 2) is described. QM crystals were used because the prototype was conceived as a concept demonstrator for low energy photons. Therefore, the number of sample used was small and the their thickness traversed by the X-ray beam had not to be large.

2.2 Innovative methods to fabricate bent crystals

Three new methods aimed at producing self-standing bent crystals are presented in this section. They are based on carbon fibre deposition, ion implantation, and sandblasting respectively. These techniques have been developed at Sensor and Semiconductor Laboratory (SSL) of Ferrara within the frame of the INFN-LOGOS project.

2.2.1 Deposition of a carbon fibre film

The deposition of thin films may be a viable technique to obtain self-standing bent crystals with a controlled and uniform curvature [47]. The curvature induced by film deposition is already well known in microelectronics as a drawback of device manufacturing. The stress due to deposition of the most common materials has been measured, and it is usually minimized during device manufacturing. This stress can be maximized with a different application of the knowledge of the processes. The study of this stress with the aim of inducing a large and uniform curvature in crystals is the argument of this section. Finally, experimental evidences of a silicon crystal bent through carbon fibre deposition are given.

Silicon micromachining techniques provides a wide range of processes to deposit thin

and thick films on silicon substrates. Deposition techniques are divided in two large areas: chemical and physical depositions. Chemical depositions involves a fluid or gas precursor which undergoes a chemical change at a solid surface, leaving a solid layer. Physical deposition uses thermodynamic, mechanical, or electromechanical means to produce a thin film of solid. The largest part of depositions techniques are carried out at elevated temperatures. For example, dissociation of the precursors used in chemical depositions are typically reached placing the sample in a heated reaction chamber. In physical deposition, instead, the material to be deposited is placed in an energetic, entropic environment, so that particles of material escape from its surface. Facing this source is a cooler surface which draws energy from these particles as they arrive, allowing them to form a solid layer. In order to allow the particles to travel as freely as possible, the whole system is kept in a vacuum deposition chamber. As a consequence of cooling of the sample from the deposition temperature to room temperature, thermal stress generates in the film and in the substrate, causing a permanent deformation of the sample.

Provided that the stress in the substrate and in the deposited film are not too high to cause delamination of the film from the substrate or even cracks in the film or in the substrate, deposition of thin or thick films allows achievement of a self-standing bent structure, removing the need of a mechanical bender, providing in this way space saving samples of reduced weight.

Deposition of a film of carbon fibre may be an effective method to bend thick crystals. Self-standing mono-crystals up to 5 mm thick can be produced because of the elevated value of carbon fibre stiffness. The method is expected to work with different kinds of crystals, such as silicon, germanium, gallium arsenide, copper, and others. Moreover, the method is fully compatible with mass production. Indeed, a batch of hundreds of crystal tiles takes about one hour for fibre deposition in autoclave.

Experimental method and results

A silicon crystal was bent through the deposition of a thick film of carbon fibre. The sample was shaped at the Sensor and Semiconductor Laboratory (SSL) of Ferrara, Italy, through a high precision dicing saw (DISCO^{TM} DAD3220). Its dimensions were 20×20×5 mm. The largest surfaces were oriented as (111) planes. Such orientation was chosen because in order to have isotropic elastic constants. A photo of the sample is shown in Fig.2.3.

The carbon fibre deposition was exploited to obtain an asymmetric laminate capable of producing a curvature of the substrate. This is mainly due to the cross ply stacking sequence, whose differential shrinkage and stiffness along two perpendicular directions causes

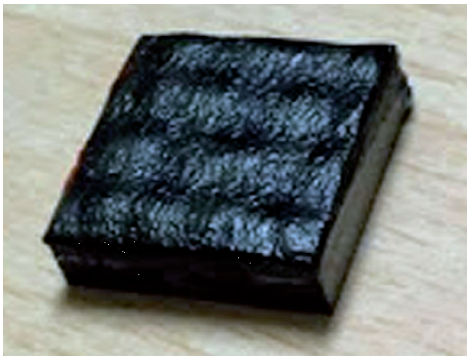

Figure 2.3: Photo of the crystal plate. The carbon fibre film is visible.

Table 2.1: Main features of the sample and the beam

Sample size (mm)	20×20×5
Thickness traversed by X-rays (mm)	20
Diffraction geometry	1
Diffracting planes	(111)
Beam energy (keV)	150
Beam width (μm)	50×50
Beam monochromaticity (ΔE/E)	2x10^{-3}

the bending of the laminate during the curing cycle. For standard composite production, this phenomenon is avoided by balancing the plies deposition, in order to avoid unwanted internal stresses, which may bend the substrate as side effect. Instead, for our purpose, we tried to maximize this effect. The film of fibres consisted of four layers of carbon fibre fabric. The direction of the fibres in each layer was perpendicular to that of the neighbouring layers. Each fibre was characterized by an intermediate elastic modulus of $E = 230$ GPa in weft direction and an ultra high elastic modulus of $E = 600$ GPa in the warp direction. The fibres were bound to the crystals with an autoclave cure cycle at a temperature of $135°C$ and pressure of 6 bar.

The curvature of the sample was tested through hard X-ray diffraction at beamline ID15A of the European Synchrotron Radiation Facility (ESRF, Grenoble, France). The beam was set at the highest energy with enough luminosity, namely 150 keV, whereas the beam width was 50×50 μm^2 wide. A monochromator was used to obtain a resolution of ΔE/E = 2x10^{-3}. The sample and beam parameters are listed in Tab.2.1.

The characterization of the samples was carried out by performing rocking curves (RCs), namely by recording either the transmitted or diffracted beam intensity while the crystal was being rotated in the beam around the position where the Bragg condition was satisfied. The full width at half maximum (FWHM) of the RC was a direct measurement of the angular distribution of the diffracting planes. Fig.2.4 shows the experimental result.

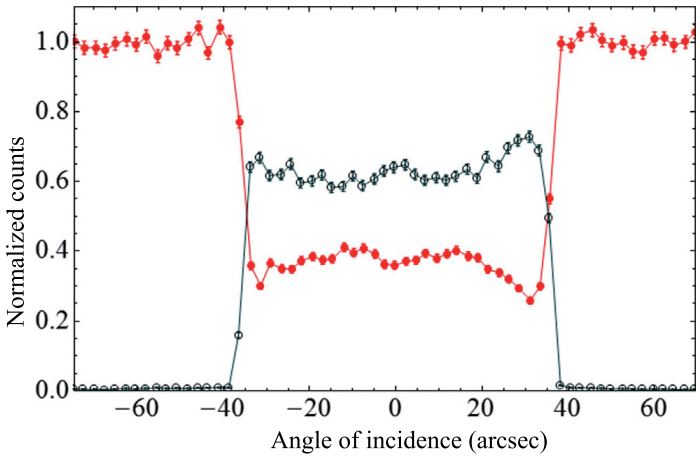

Figure 2.4: Experimental result. Filled red circles plot the intensity of the transmitted beam, whereas empty blue circles plot the intensity of the diffracted beam.

The angular spread Ω, namely the FWHM of the RC, is 72± 2 arcsec. Since the traversed length L was 20 mm, the radius of curvature R of the sample is $R = L/\Omega \approx 57 \pm 2$ m. The RC is flat-topped, which means that the sample curvature was homogeneous. The diffraction efficiency turns out to be 63±6%, which is a value not attainable with a standard mosaic crystal. Such characteristics make this sample suitable to be used as an optical element for a Laue lens. The main drawback of the proposed method is that the technique does not permit producing small bent crystals, and thus it is not suitable for the applications where miniaturized samples are required.

The sample and the experimental set-up reported here are the same as those reported in [47]. However, the samples characteristics were not completely identical. Indeed, the sample described here was bent using different carbon plies, namely the weight and the density of the carbon fibre were higher. As a consequence, a larger curvature was achieved. Here, the total thickness of the carbon-fibre film was about 600 μm. It can be concluded that it is possible to control the curvature of the sample by adjusting the parameters of the carbon fibre deposition. An analytical model, based on the linear theory of elasticity, is under development.

2.2.2 Ion implantation

Ion implantation can be exploited to produce self-standing bent crystals. Ion implantation has been used in the semiconductor industry for several decades [48]. A drawback of this process for semiconductor manufacturing was the production of stress in the implanted material [49]. This early disadvantage was later turned into a technology for the correction of stresses in thin films and substrates. Implanting high-energy ions into a substrate imparts

compressive stresses, causing controllable deformation of the substrate. For example, ion implantation has been used for the correction of shape errors in X-ray stepper masks [50], X-ray mirrors [51], and MEMS (Micro Electro-Mechanical Systems) deformable mirrors [52].

Sample preparation and simulation

In this section, we describe a macroscopic monocrystalline Si plate uniformly bent by ion implantation, with self-standing curvature. The sample is 10×10 mm large and 0.2 mm thick. Si is an anisotropic material, thereby the deformation due to ion implantation may result in a non-uniform curvature even if the induced stress field was uniform. Nevertheless, (111) Si lattice planes have isotropic elastic constants. For this reason, a (111) oriented wafer was chosen for the production of the sample.

The sample was implanted using He^+ at the INFN Laboratories of Legnaro (Padova, Italy). Helium ions were accelerated to an energy of 150 keV and directed normally toward the sample surface. The current density of the ion beam was 1 μA/cm^2. The beam flux was found to be temporally and spatially uniform within 5% over an area of 150 mm of diameter. The dose implanted into the sample resulted 2×10^{16} atoms/cm^2.

He^+ was chosen because light ions interact with the substrate nuclei only near the stop point, thereby minimizing the lattice damage. Indeed, considering the mass and the initial energy of the ions, the main mechanism through which the ions lost energy was the interaction with the electrons [53]. SRIM [54] simulations indicate for 150 keV He^+ ions in Si an initial electronic stopping of about 250 eV/nm and a nuclear one of 2 eV/nm. During this slowing-down process, ions are deflected very little and move in an almost straight line, causing few dislocations in the crystalline lattice. The energy lost per unit of path is described by the Bragg curve [55], which has a peak near the final point of the trajectory where the ion velocity is low and the transferred momentum is maximum. At this point, the interactions of the implanted ions with the nuclei of the substrate become significant and the number of dislocations in the crystalline lattice increases. Under the conditions of implantation aforementioned, the depth distribution of implanted He^+ ions was simulated through the SRIM program (see Fig.2.5). The ions projected range resulted $Rp = 0.88$ μm with a straggling of $\sigma = 0.14$ μm. When stopped, the ions cause the amorphization of the substrate and thus its swelling [56]. As a result, the implantation process is capable of imparting a sub-surface stress, creating a tensile layer buried in the substrate structure [57].

The buried layer of amorphous material extends below the sample surface within $\pm3\sigma = 0.84$ μm. This layer represents 0.42% of the total volume of the crystal, namely it is a very thin layer. For this reason, the crystals can be considered "defect-free" for the applications

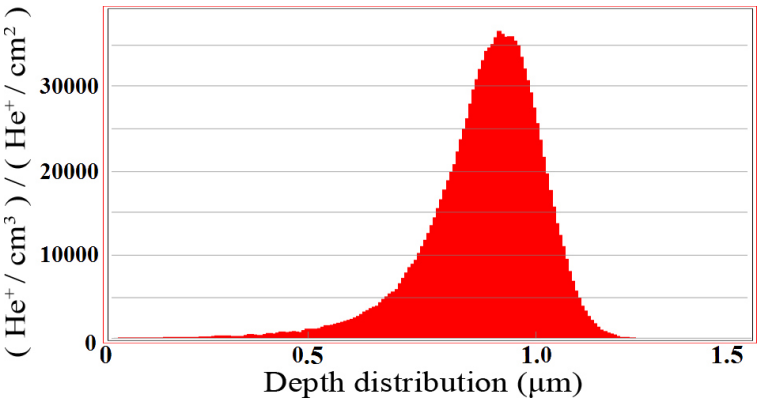

Figure 2.5: Depth distribution of implanted He^+ ions in a monocrystalline Si substrate simulated through the SRIM program.

that require a high lattice quality of the crystal bulk.

Fig.2.6.a shows the deformation of the sample as measured using an optical profilometer (VEECO^{TM} NT1100). The sample resulted uniformly bent with a curvature radius of 10.5±1.0 meters. This curvature is the largest achieved in literature for a macroscopic Si sample implanted with ions under the MeV energy.

The amorphous-Si phase is metastable and may transform into crystalline-Si. The transformation rate is strongly dependent on temperature and presents an Arrhenius-like behaviour with an activation energy of 2.7 eV. At temperatures below ∼300°C, the amorphous to crystal transition is kinetically inhibited [58]. Thus, to prove the stability of the obtained curvature, we submitted the sample to a 300°C annealing process 3 hours long and then we measured again the curvature, founding it unchanged. This operation was performed at SSL using a Lenton ECF 12/6 chamber furnace.

Since the amorphized portion of the sample acts as a tensile film, the Stoney formalism for an equi-biaxial plane stress regime can be applied [59]:

$$\sigma_f = \frac{E_s}{6(1-\nu_s)} \frac{h_s^2}{h_f} \frac{1}{R} \tag{2.1}$$

where h_s and h_f are the thickness of the substrate and of the tensile film, respectively. E_s and ν_s are the Young's modulus and Poisson's ratio of the substrate, σ_f the film tensile stress, and R is the local radius of curvature. Since the exact value of the film thickness is not known, the integrated stress in the film $S = \sigma_f h_f$ has been used in the computation. Since R = 10.5 m, using the Stoney's formula it can be inferred that ion implantation induced an integrated stress S of 145.4 ± 14.0 Pa×m.

The effect of ion implantation was then simulated through Straus7 finite element (FE) package [60]. An equivalent Si layer 1 μm thick and with a tensile stress of 145.4 MPa

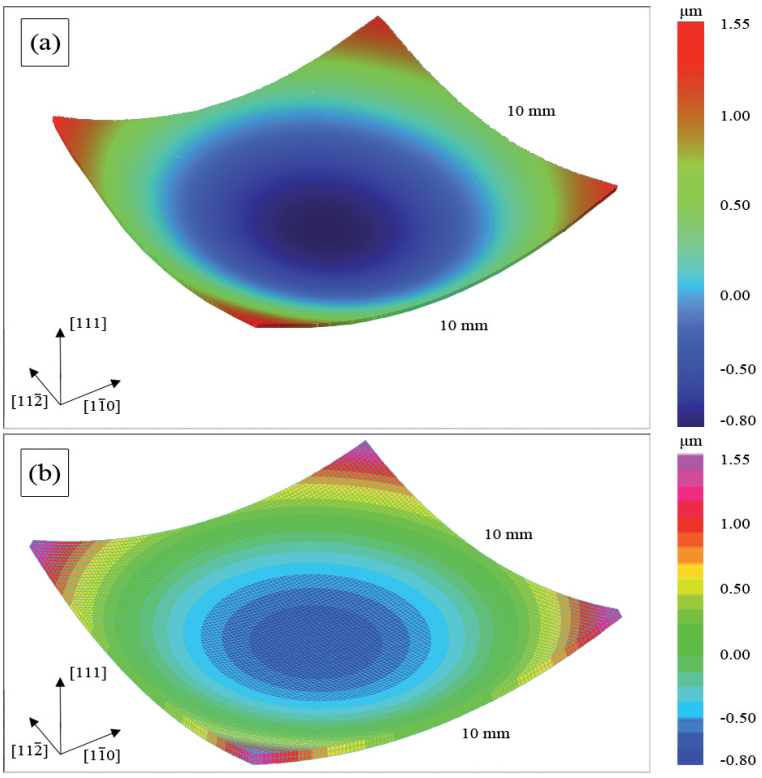

Figure 2.6: Square sample bent to a spherical curvature using ion implantation. The surface that did not undergo the implantation process is displayed. (a) Morphological surface of the sample measured through interferometric profilometry. (b) Same sample simulated through FE analysis.

bonded to a Si crystal 10×10×0.2 mm with the same crystallographic orientation as the manufactured sample was simulated. A net and spherical curvature was obtained, with the radius of curvature being 10.7 m (see Fig.2.6.b).

The effect of ion implantation was finally analytically calculated through *AniCryDe* [61], imposing a couple of perpendicular moments per unit length

$$M_{[1\bar{1}0]} = M_{[11\bar{2}]} = \sigma_f h_f \frac{h_s + h_f}{2}, \tag{2.2}$$

to the crystal plate. In this case, the radius of curvature turned out to be 10.4 m.

X-ray analysis

The depth reached by the implanted ions is very small compared to the crystal thickness, that is 200 μm. Then, defects and dislocations do not affect the crystal bulk. In order to verify that the whole crystal structure is not altered and uniformly bent, the sample was tested by X-ray diffraction using a beam that passed through the entire crystal thickness, namely in transmission (Laue) geometry. The characterization was carried out

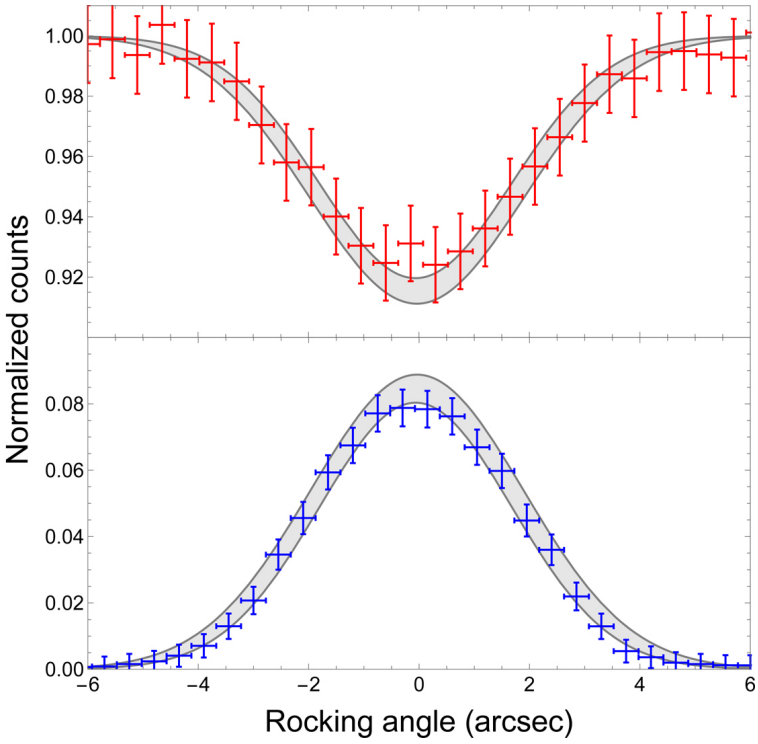

Figure 2.7: Rocking curves by X-ray diffraction. Experimental intensities for the diffracted (blue) and the transmitted (red) beam are plotted taking into account the experimental uncertainty. The gray areas represent the expected results as calculated by taking into account the uncertainty on the radius of curvature of the sample.

by performing rocking curves (RCs).

Curved crystalline planes were selected for the diffraction experiment because, in this case, the RCs contain information related to the crystalline quality of the bulk. Indeed, the full width at half maximum (FWHM) of the RCs for a perfect bent crystal is equal to the angle subtended by the curved diffracting planes, since the Bragg condition is met within the angular range defined by the diffracting plane curvature. If the crystal quality is deteriorated, the RCs would result broadened and the diffraction efficiency would decrease with respect to the theoretical value [12]. (311) planes were chosen because they are the curved lattice planes in Laue geometry with the highest diffraction efficiency. Here, (311) planes are in asymmetric configuration, holding an asymmetry angle $\phi = 58.52°$ from the (111) surface [62]. Thus, diffraction occurred according a configuration rotated by 58.52° with respect to the geometry 1.

Characterizations were performed at beamline ID15A of ESRF (Grenoble, France). A highly monochromatic and collimated beam was tuned to 150 keV by a two-reflection Laue Si (111) unbent monochromator. The monochromaticity was $\Delta E/E = 2\times10^{-3}$, the beam size was 50×50 μm. Diffraction analysis is shown in Fig.2.7. The expected diffraction efficiency was calculated taking into account an ideal bent crystal. The good agreement

between experimental data and theoretical expectations indicates that the crystallographic planes are homogeneously bent and the crystallographic quality preserved. The technique here proposed is precise and suited for miniaturization, however it requires an ion implanter and does not permit to bend crystals thicker than few hundreds of μm.

As an elective application of ion implantation to obtain a deformed crystal, we envisage the fabrication of a crystalline undulator (CU). A CU consists of a crystal whose planes are periodically bent with an amplitude much larger than the interplanar spacing. Such an undulator can be exploited as a generator of electromagnetic radiation by ultra-relativistic positrons channeling in the undulated planes of the CU [36]. Indeed, ion implantation can be used to produce precise bending of perfect crystals, leaving the bulk substantially defect-free, which is a necessary condition for channeling experiments. Moreover, ion implantation can be combined to photolithographic techniques, in order to produce micrometric pattern of implanted regions. In [63], we numerically simulated a Si CU, 5 mm long, 0.2 mm thick, and 1 mm wide; the undulating period was 1 mm. The same CU was realized through the grooving method and successfully tested using a proton beam [64]. These parameters fulfil the condition for an optimal undulator in the case of 15 GeV positrons.

2.2.3 Sandblasting

Sandblasting (or simply blasting) is a mechanical process that consists in driving a stream of abrasive material against a surface. A pressurized fluid, typically compressed air, is used to propel the blasting material. Sandblasting is commonly used to smooth a rough surface, roughen a smooth surface, shape a surface, or remove surface contaminants. Here, we propose to use sandblasting for producing self-standing bent crystals. Indeed, the thin damaged layer that originates at the surface of a blasted crystalline sample acts as a tensile film able to bent the crystal bulk. The advantages of this technique are that it is suitable for mass production, it is fast and economical, it does not add any materials to the crystal, and it permits to bend from thin to thick crystals, up to several mm. The drawback is that a thin layer of the material results damaged by the process itself. In particular, this type of self-standing bent crystal would be a very good solution if used as an optical element of a Laue lens for medical purpose or as an optical element for manipulating charged particles in the cases where contaminating materials are not allowed.

Experimental method and results

Several Si crystals were prepared and machined at SSL. The samples were shaped through a high precision dicing saw (DISCO^{TM} DAD3220) as squared tiles 10×10 mm wide, featuring

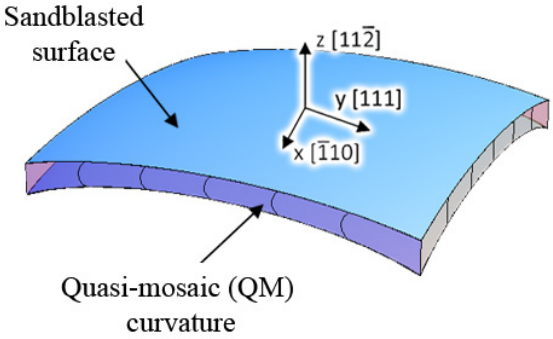

Figure 2.8: Schematic representation of the machined Si samples.

Table 2.2: Characteristics of the sandblasting process

Sample material	Si
Sample size (mm)	10×10
Sample thickness (mm)	0.5, 1.0, 2.0
Sandblaster	SAMAC
Compressed air consumption	560 lt/s @ 6 bar
Blasting medium	natron glass
Blasting size (μm)	1 - 50
Blasting density (g/cm^3)	2.3±0.3
Blasting hardness (Mohs)	6
Blasting distance (cm)	$\sim$ 10
Blasting time (s)	120

three different thicknesses, namely 0.5, 1.0, and 2.0 mm. In particular, three samples for each thickness were produced. The crystallographic orientations of the nine samples are shown in Fig.2.8.

The deformation of the samples was obtained by sandblasting of one of the largest surfaces of the tiles. The characteristics of the manufacturing process are listed in Tab.2.2. Then, the curvature of the samples was measured by using an optical profilometer (VEECO^{TM} NT1100) with 1 μm lateral and 1 nm vertical resolution. Since the machined surface is damaged, the profilometric characterization was carried out on the back face of the samples. The results of the profilometric measurements are listed in Tab.2.3.

The sandblasting process produced dislocations on the machined surface of the samples, the thickness of the damaged layer being dependent on the sandblasting process. This layer resulted in a plasticized thin film that bent the crystal. As in other contexts where a plasticized layer lays on the crystal surface, it is possible to model the layer as a compressive thin film. Indeed, the plasticized layer is capable of transferring coactive forces to the crystal bulk, thus producing an elastic strain field within the crystal. Therefore, the Stoney formalism for an equi-biaxial plane stress regime can be adopted. In order to take into

Table 2.3: Experimental and simulated results for the radius of curvature of the samples along the [111] direction.

Sample thickness	Interferometric measurements	Analytical calculation	Simulation with Straus7	Simulation with AniCryDe
0.5 mm	6.2±0.7 m	5.1±0.2 m	5.3±0.1 m	5.1±0.2 m
1.0 mm	20.6±1.8 m	20.4±0.6 m	20.8±0.4 m	20.3±0.7 m
2.0 mm	80.0±6.3 m	81.5±2.6 m	82.5±1.8 m	81.4±2.6 m

account the anisotropic behaviour of Si crystal, the Stoney formula can be written as in [65]:

$$\sigma_f = \frac{{h_s}^2}{6(S_{11}+S_{12})h_f}\frac{1}{R}, \tag{2.3}$$

where h_s and h_f are the thickness of the substrate and of the compressive film respectively, σ_f the film stress, R the curvature radius of the sample, and S_{ij} are the components of compliance tensor for anisotropic material referred to the (x, y, z) Cartesian system [66].

The film thickness was not directly measurable. It was estimated to be ~ 5 μm [67]. By fitting the experimental data with Eq.2.3, σ_f resulted 374±8 MPa. The effect of sandblasting was then simulated through *Straus7* finite element package. An equivalent damaged Si layer 5 μm thick and with a compressive stress of 374 MPa bonded to Si crystal tiles with the same size and crystallographic orientation as the manufactured samples was simulated. The output of the simulations is reported in Tab.2.3. The effect of sandblasting was finally evaluated using the software *AnyCriDe*, imposing a couple of perpendicular moments per unit length to the crystal plate $M_x = M_y = \sigma_f h_f \frac{h_s+h_f}{2}$. The simulation results are reported in Tab.2.3.

Since the simulations are in good agreement with the experimental data, the thin layer of damaged material can be appropriately considered as a compressive thin film.

X-ray analysis

To evaluate the crystalline quality, the samples were tested through γ-ray diffraction at the Institut Laue-Langevin (ILL, Grenoble, France) at DIGRA, that is a facility specifically built for characterizing instrumentation for astrophysics. The γ-ray beam energy was 181.931 keV and its monochromaticity was $\Delta E/E \approx 10^{-6}$. The beam flux was produced by neutron capture in a gadolinium target ($^{157}_{64}$Gd) inserted close to the nuclear reactor of ILL at a temperature of about 400°C. The beam divergence after a Si (220) monochromator was $\sim$ 3.5 arcsec, as measured by recording a rocking curve (RC) of the monochromator itself. The collimated beam size was 1×2 mm^2. A standard electrode coaxial Ge detector with

Table 2.4: Experimental and theoretical results for the rocking curves.

Parameter	Sample 1	Sample 2	Sample 2 (QM)
Traversed length (T_0 - mm)	10	10	2
Expected angular width (Ω)	30.0±3.0”	30.8±3.1”	3.7±0.2”
Measured angular width (Ω)	26.8±0.5”	28.5±1.0”	3.6±0.3”
Expected diffraction efficiency (η)	0.30±0.01	0.28±0.01	0.23±0.01
Measured diffraction efficiency (η)	0.27±0.03	0.24±0.03	0.25±0.02

25% relative efficiency was used.

Characterization of the samples was carried out by performing RCs. The crystals were analysed using two different geometries. In the first geometry, the beam passed through the sample along the [111] direction, traversing 10 mm of material (geometry 1). In this geometry, the curvature directly induced by the sandblasting process was measurable. In the second geometry, the beam passed through the shortest side of the crystal, i.e. along the [11-2] direction (geometry 2). In this configuration, it was possible to record the RC of the crystallographic planes bent by the quasi-mosaic (QM) effect [42]. Indeed, the (111) planes resulted bent by the QM effect, as shown in Fig.2.8.

The 2 mm thick samples were selected for X-ray analysis because they were able to show the highest reflectivity. In particular, two samples were tested in the geometry 1 (Fig.2.9.a and b), while the second sample was also measured using the geometry 2 (Fig.2.9.c).

By fitting the RCs with the dynamical theory of diffraction, it is possible to derive the sample curvature, the homogeneity of the curvature, and the quality of the crystal bulk. Indeed, the width of the RC is proportional to the bending angle of the sample and the RC peak is a measure of the crystal quality. The diffraction efficiency is given by the formula

$$\eta = 1 - e^{\frac{-\pi^2 T_0 d_{hkl}}{\Omega \Lambda_0^2}}, \tag{2.4}$$

where T_0 is the crystal thickness traversed by radiation, d_{hkl} the d-spacing of the diffracting planes (hkl), Λ_0 the extinction length as defined in chapter 1 for the Laue symmetric case, and Ω the bending angle of the curved diffracting planes. Experimental results and theoretical expectations are reported in Tab.2.4.

The results reported in Fig.2.9.c are here explained. From the theory of elasticity, the ratio between the QM curvature radius, R_{QM}, and the superficial (primary) curvature radius (R_P = 72.2 m), is $\frac{R_{QM}}{R_P}$= 2.61 for the (111) planes, thus $R_{QM} = 2.61 R_p$ = 188.5 m [42]. Here, the QM curvature corresponded to an angular spread of 2.19 arcsec for the (111) planes. Diffraction efficiency was expected to be 94.7%. The RCs reported in Fig.2.9.c

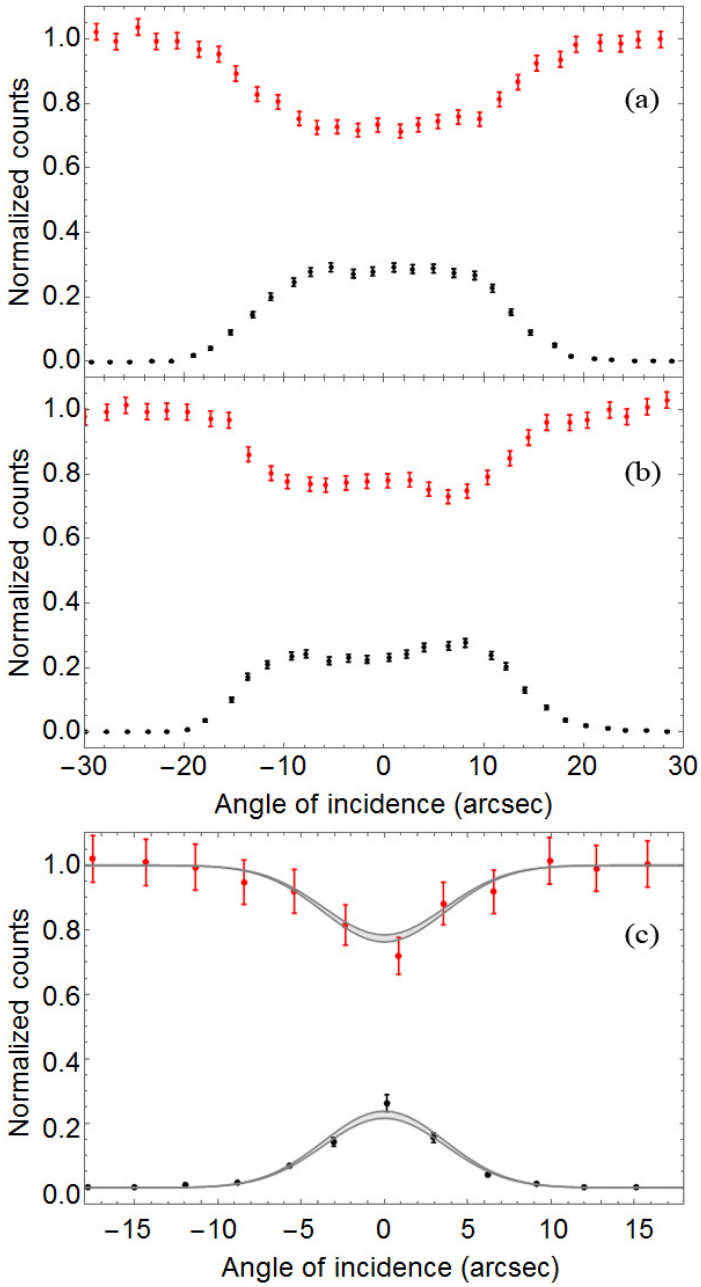

Figure 2.9: Rocking curves; black dots represent the diffracted beam, red dots the transmitted beam. (a) sample 1 in the geometry 1 (primary curvature); (b) sample 2 in the geometry 1 (primary curvature): (c) sample 2 in the geometry 2 (QM curvature). Grey areas represent the theoretical expectation.

shows a peak far lower than the prediction of the dynamical theory of diffraction. However, there are some factors that have to be taken into consideration. Indeed, the measured RC was the convolution of three functions. The first function was a uniform distribution due to the diffracting QM planes, 2.19 arcsec wide and 0.947 in height. The second function represented the spread owing to the primary curvature, which was a uniform distribution 2.85 arcsec wide and 1 in height. Indeed, the beam had a finite size of 1 mm along the x direction; thus, the primary curvature resulted in a rotation of the diffracting planes by 2.85 arcsec. The third function took into account the resolution of the experimental setup, which was represented by a Normal distribution with standard deviation equal to 3.5 arcsec. As a result, the RC was a symmetric function with 3.66 arcsec as standard deviation and peak equal to 0.238. The grey area in Fig.2.9.c represents the theoretical expectation, taking into account the uncertainty on the primary curvature of the sample. The values reported in Tab.2.4 for the QM case take into account all the contributions in the convolution.

In summary, Figs.2.9.a, b, and c highlight very good agreement between theoretical expectations and experimental results; thus, the method did not compromise the quality of the crystal bulk. Therefore, the samples produced using the sandblasting method can be profitably used as X-ray optical elements and as charged particle beam steerer.

2.3 Focusing capabilities of a bent crystal

In this section, an experiment devoted to the demonstration of the focusing capabilities of a bent crystal is described. In particular, a QM Ge sample was produced through the grooving method [65] and characterized through X-ray diffraction. Exploiting the quasi-mosaic effect, it was possible to combine high intensity of the diffracted beam due to the curvature of the diffracting planes with the focusing due to the primary curvature. The focusing effect was assessed by recording on a detector the image of the sample due to the diffraction of a polychromatic and divergent hard X-ray beam.

Sample production and characterization

Production and morphological characterization of a bent Ge sample was carried out at SSL. A sketch of the sample is shown in Fig. 2.10.

A commercially available pure Ge wafer was diced to form a plate of 10×30×2 mm using a high-precision dicing saw (DISCO^{TM} DAD3220). A permanent curvature was induced through the manufacture of a grid of superficial grooves on one of the largest surfaces of the plate. The surface grooving produced a permanent plastic deformation in a thin layer of the

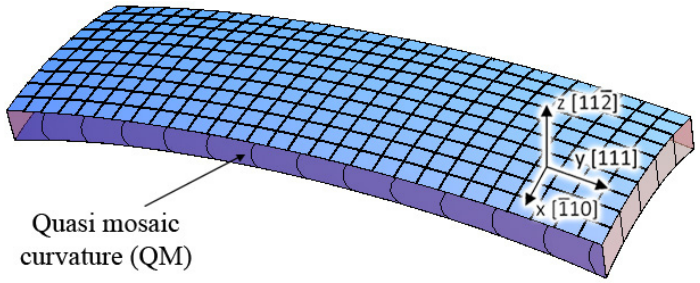

Figure 2.10: Sketch of the Ge sample. Crystallographic orientations and grooves are highlighted, with the coordinate system used.

Table 2.5: Crystal features

Material	Germanium
Tile size (mm)	10×30×2
Blade type	G1A 320
Blade width (μm)	250
Blade rotation (rpm)	3000
Blade speed (mm/s)	0.1
Diamond grain size μm	5
Groove depth (μm)	1550 ± 5
Number of grooves	9×28
Groove step (mm)	1
Primary radius of curvature R_p along y axis (m)	38.9 ± 1.9
QM radius of curvature R_{QM} (m)	92.9 ± 4.6
QM angular spread Ω_{QM} (arcsec)	4.4 ± 0.2

crystal beneath the grooves, the extension of the plasticized layer being about 5 μm [41, 65]. Such plasticized layer transferred coactive forces into the crystal bulk, thus producing an elastic strain field within the crystal. The curvature was measured by using an optical profilometer (VEECO^{TM} NT1100) with 1 μm lateral and 1 nm vertical resolution. Main features are reported in Tab.2.5.

Exploiting the QM effect, it was possible to obtain two curvatures of two different family of crystallographic planes. The grooves generated a primary curvature of the largest surfaces of the plate, which are parallel to the (11$\overline{2}$) planes of the crystal. As a result, quasi-mosaicity induced a secondary curvature of the (111) planes within the crystal, as shown in Fig. 2.10. The primary (R_p) and the QM (R_{QM}) curvature radii are linked by a ratio that depends on the material and the crystallographic orientations concerned [45]. For the case of concern, this ratio is 2.39. Thus, being $R_p = 38.9$ m, R_{QM} turns out to be 92.9 m.

The structural characterization of the sample was performed through X-ray diffraction at beamline ID15A of the ESRF (Grenoble, France). A highly monochromatic beam was set at 150 or 300 keV. The characterization of the samples was carried out by performing

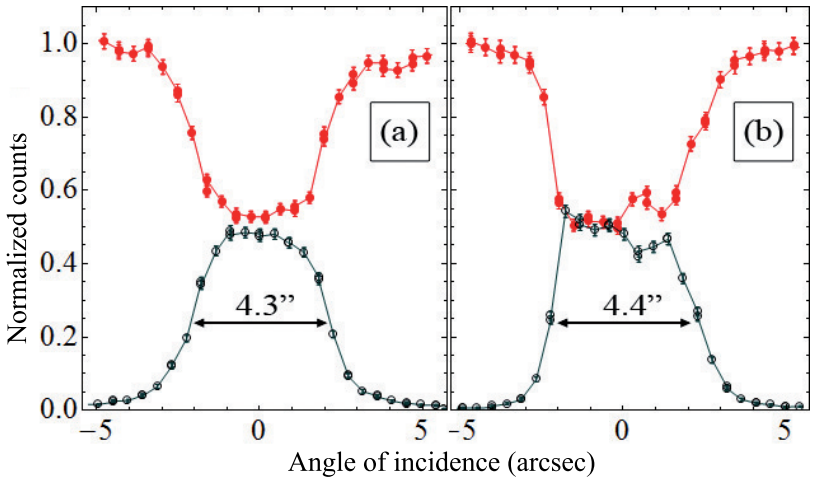

Figure 2.11: RCs of crystal. The filled red circles plot the intensity of the transmitted beam, whereas the empty blue circles plot the intensity of the diffracted beam. (a) Beam energy at 150 keV. (b) Beam energy at 300 keV.

rocking curves. The beam size was 50×50 μm wide, impinging on a region of the sample free of the grooves. Rocking curves are shown in Fig. 2.11.a and b.

The FWHM of the RCs is a direct measurement of the angular distribution of the (111) diffracting planes. Since the sample was 2 mm thick, the FWHM of the angular spread was expected to be 4.4 arcsec. This value was well verified through analysis of broadening of the RCs at both beam energies. The reflectivity was about 50% for both cases, though the expected values were 100% at 150 keV and 95% at 300 keV. We observed an effect similar to that in [68, 69], namely diffraction efficiency was pinned at 50% if the diffraction occurred in a layer of material rich in defects and cracks. This effect was interpreted in [69] as a sort of partial mosaicization of the sample due to the grooving process. From a microstructural point of view, the material close to the grooves is subjected to contact with numerous particles of the blade at the same moment, which cause different contact pressures and produce different depth of cut due to their different shape and size. Thus, metallization, plastic deformation and brittle fracture may occur simultaneously [67]. The scarce knowledge of the distribution of dislocations, defects and cracks in the structure due to the grooving process makes it infeasible any attempt to predict analytically the diffraction efficiency. However, recorded values of diffraction efficiency are quite satisfactory, being higher than any other performance relying on mosaic crystals.

Focusing of an X-ray beam

In order to highlight the focusing effect driven by the sample curvature, the crystal was analysed through a diverging and polychromatic X-ray source at Institut Laue-Langevin

Table 2.6: Experimental and detector parameters an their uncertainty

parameter	mean value	uncertainty
Source-to-sample distance L_S (m)	4.45	0.04
Sample-to-detector distance L_D (m)	variable	0.02
Source-to-collimator distance (m)	3.03	0.03
Collimator-to-sample distance (m)	1.42	0.01
Collimator width (mm)	9.5×9.5	0.1
$\overline{CO}$ (mm)	45	1
Portion of crystal hit by the beam l (mm)	14.5	0.6
Source diameter a (mm)	1.0	0.1
Mean Bragg angle θ_B (degree)	0.58	negligible
Beam divergence ε (degree)	0.100	0.004

Table 2.7: The detector: high-resolution and sensitive X-ray image intensifier coupled with a CCD camera

Number of pixels	512×512
Size of each pixel (mm)	0.35×0.35
Acquisition time	few seconds

(ILL, Grenoble, France) [70, 71]. The diffractometer used a high-voltage and fine-focus X-ray tube designed for industrial radiography, the X-ray energy range being between 80 and 420 keV. The beam impinged onto the sample with an angle depending on the position at the entry face of the crystal. Thus, X-rays with different energies were diffracted towards the image point, which depended on the curvature of the crystal. A sketch of the experimental configuration is shown in Figs. 2.12.a and 2.12.b.

Diffraction of (111) planes was firstly analysed with the beam impinging on the crystal surface as in Fig. 2.12.a. Then, the crystal was rotated by 180° around the x axis (see Fig. 2.12.b). The geometrical parameters are reported in Tab. 2.6, whereas the detector is described in Tab. 2.7. Considering the geometrical configuration, the energy range of diffracted beam turned out to be 160-227 keV.

The crystal behaved as a cylindrical lens because the focusing effect occurred only in the scattering plane. Diffraction of a polychromatic and divergent beam produces a line on the detector [72]. The FWHM of the intensity profile, taken on a cross section perpendicular to the line, depends on several parameters. In the case of a perfect crystal and the sample-to-detector distance L_D equal to source-to-sample distance L_S, the width size depended only on the X-ray source size and on the crystal thickness traversed by the beam. Conversely, a curved crystal can concentrate the diffracted X-rays at either smaller or larger distance.

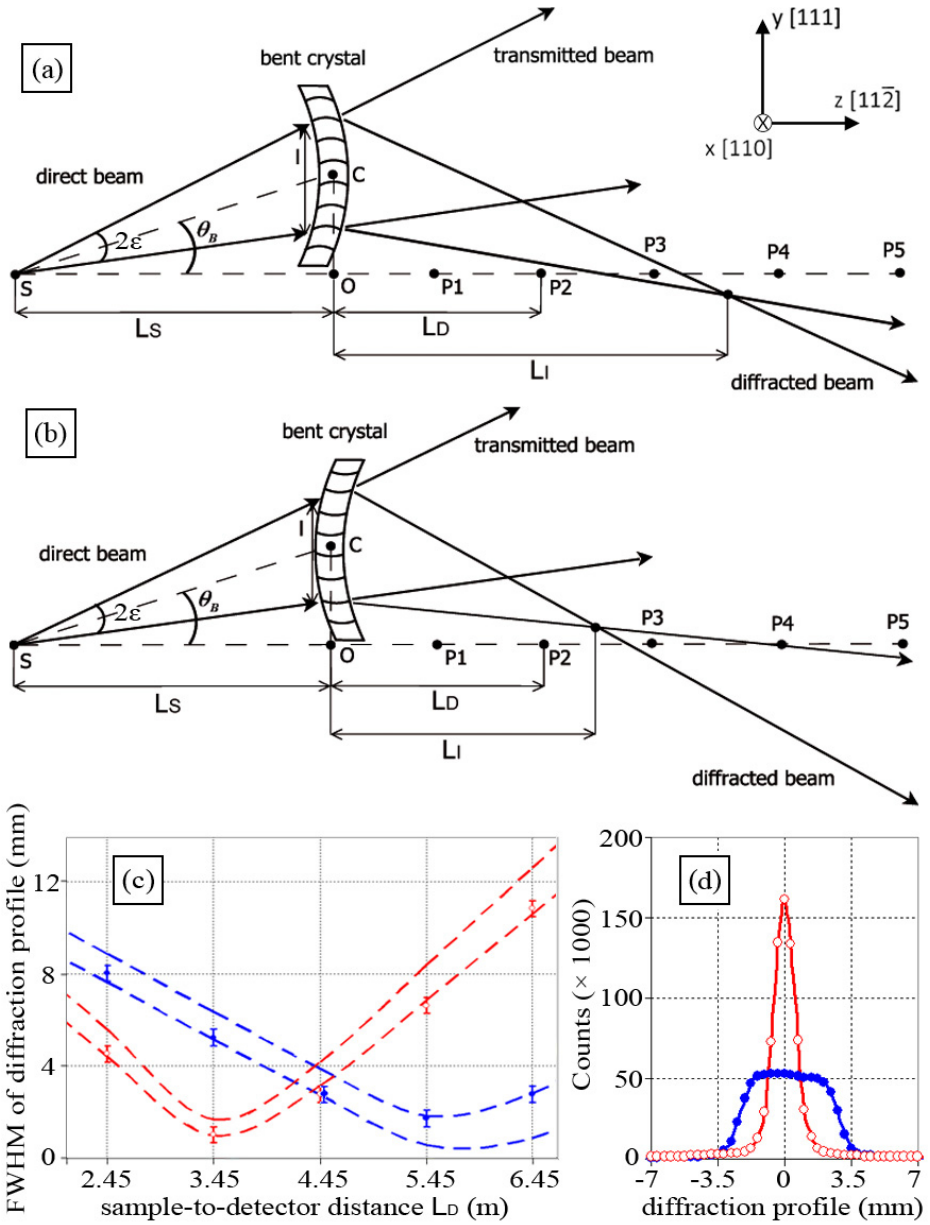

Figure 2.12: Schematic representation of the experiment with a divergent polychromatic X-ray beam and the bent crystal with the QM curvature in Laue symmetric geometry. Depending on the sign of R_P, the image distance increases (a) or decreases (b). (c) FWHM of diffraction profile plotted as a function of sample-to-detector distance L_D. Blue filled circles plot the measured width related to (a) and red empty circles plot the measured width related to (b). Dashed lines enclose the range of the theoretical width calculated using Eq. 2.6 and considering the uncertainty over parameters. (d) Diffraction profile with detector in position P2 ($L_D = 3.45$ m). Blue filled circles refer to (a), red empty circles refer to (b).

Indeed, under the small-angle approximation, it is possible to obtain

$$\frac{1}{L_i} = \frac{1}{L_S} + \frac{2}{R_P} \tag{2.5}$$

where L_i is the image distance of a bent crystal with primary radius of curvature equal to R_p. The plate divides the space into a convex and a concave region[1]. We set $R_P < 0$ when the incident beam comes from the part of plane topologically convex (Fig. 2.12.a), while $R_P > 0$ in the opposite case (Fig. 2.12.b).

To evaluate the focusing capability of the sample, we recorded the FWHM of the diffracting profile on the detector, that is

$$FWHM = \sqrt{a^2 + \left(\left|2t\theta_B + 2L_D\frac{t}{R_{QM}}\right| + l\left|1 - \frac{L_D}{L_i}\right|\right)^2} \tag{2.6}$$

where a is the source diameter, t the sample thickness traversed by the beam, l the size of the beam on the crystal surface and R_{QM} the radius of curvature of the QM diffracting planes. In this case $R_{QM} < 0$ when the incident beam comes from the part of plane topologically convex with respect to the QM diffracting planes (Fig. 2.12.a), while $R_{QM} > 0$ in the opposite case (Fig. 2.12.b). The term $2L_D\frac{t}{R_{QM}}$ represents the contribution of quasi-mosaicity, which can modify the FWHM of the spot but not the distance L_i. If $L_D = L_S$ it is possible to obtain the formula described in [73, 74].

The image distance was $L_i = 5.77$ m for Fig. 2.12.a and $L_i = 3.62$ m for Fig. 2.12.b. In order to verify the effect of the crystal curvature, the detector was positioned at 5 different points indicated with $P1$, $P2$, $P3$, $P4$, $P5$ in Figs. 2.12.a and 2.12.b, while L_S was kept fixed. L_D was increased by steps of 1.00 m, starting from 2.45 m for $P1$ to 6.45 m for $P5$. In Fig. 2.12.c the width of the measured diffraction profiles were plotted as a function of L_D, in agreement with their theoretical expectations. Finally, Fig. 2.12.d shows the measured diffraction profiles with $L_D = 3.45$ m ($P2$).

[1] We adopted the mathematical definition of convexity

Chapter 3

Laue lenses for nuclear medicine

3.1 Motivations

The techniques of diagnostic nuclear medicine, namely scintigraphy, Single Photon Emission Computed Tomography (SPECT), and Positron Emission Tomography (PET), represent some of the best methods for medical imaging [75]. While X-ray based Computed Tomography (CT) and Magnetic Resonance Imaging (MRI) provide accurate images of anatomical districts, diagnostic nuclear medicine permits the analysis of some metabolic processes and an early recognition of tumour masses.

More specifically, in a CT exam, the patient's body is irradiated through an external X-ray beam emitted by an X-ray tube capable of rotating around the bed. Since the X-rays are absorbed by tissues basically depending on their density, a *morphological imaging* can be performed by detecting the not absorbed radiation through a detector positioned behind the patient. In nuclear medicine, a molecule directly involved in a specific metabolic process is marked with a short-lived radioactive atom. Such compound, called radiopharmaceutical or radiotracer, is given, generally by injection, to the patient and accumulates in a specific organ or anatomical district. The most used radiotracers are shown in Table 3.1. They are γ-emitters for scintigraphy and SPECT, and β^+-emitters for PET. In the PET case, positrons annihilate with electrons producing two 511 keV back-to-back photons. Therefore, with both kinds of radiotracers, a concentration map of the metabolic activity, i.e. a *functional imaging*, can be obtained by detecting the emitted photons. Scintigraphy and SPECT performances are heavily influenced by the collimator positioned before the detector and used to discriminate the direction of the photons. This element leads to a trade-off between efficiency and spatial resolution. Typical values for resolution of conventional SPECT and PET are 5-15 mm and 3-5 mm respectively [75]. In the PET case there is an intrinsic

Table 3.1: Typical radioisotopes used in diagnostic nuclear medicine

Nuclide	Radiotracer	Decay mode	Decay product	$T_{1/2}$	E_γ [keV]	SPECT/PET	Usage
^{99m}Tc	$NaTcO_4$	IT	^{99}Tc	6.02 h	140.5	*SPECT*	*general purpose*
^{67}Ga	*Ga citrate, Ga nitrate*	EC	^{67}Zn	78.3 h	93, 185, 300	*SPECT*	*tumour imaging*
^{111}In	*I salts*	EC	^{111}Cd	67.8 h	171, 245	*SPECT*	*brain study, intestinal disturbs*
^{123}I	NaI	EC	^{67}Te	13.2 h	159	*SPECT*	*thyroid study*
^{201}Tl	*Tl salts*	EC	^{201}Hg	73.1 h	135, 167	*SPECT*	*diagnosis of coronary artery disease*
^{18}F	*FDG, F-DOPA*	β^+	^{18}O	109.8 min	511	*PET*	*oncology, neurology*
^{15}O	O_2, CO_2, CO	β^+	^{15}N	2.03 min	511	*PET*	*neurology*
^{11}C	CO_2, CO, HCN, CH_3I	β^+	^{11}B	20.38 min	511	*PET*	*cardiology*
^{13}N	NH_3	β^+	^{13}C	9.96 min	511	*PET*	*cardiology*

limitation due to the path of the positrons within the tissue before their annihilation [76]. If a resolution close to 1 mm is required, a pinhole SPECT is typically employed [77]. Nevertheless, this technique allows investigating a limited region and shows a resolution-efficiency trade-off. Therefore, the conventional techniques suffer from low spatial resolution and low signal-to-noise ratio for a small radioactive source, e.g. a tumour in its initial stage of development.

In radionuclide imaging of small animals, a sub-millimetre spatial resolution can be achieved at the cost of an increased complexity by using a multipinhole system, namely several tens of pinholes that image onto a single detector [78, 79]. However, it is still unknown whether these multipinhole methods can achieve spatial resolutions in the range of 100 μm. Furthermore, this type of system is hardly adaptable for human imaging because of the geometrical constraints required to reach peak performance.

In radionuclide imaging, the image resolution and quality can be actually increased by using an efficient focusing device. Since the real part of the index of refraction of all materials is approximately equal to 1 for high-energy photons, the use of common optical elements is prevented [4].

The desired effect can be obtained by using a Laue lens, namely a device that exploits diffraction in crystals to concentrate a large number of photons onto a small area of a detector. This optics has been initially studied for the realization of a high-energy telescope [7] and subsequently has also been proposed to be used in nuclear medicine [17]. Fig. 3.1 schematically shows the configuration of a diagnostic system exploiting a Laue lens.

Some prototypes of Laue lens for nuclear medicine have already been realized [18]. However, they provide at the most the same image resolution achievable with a conventional PET. Thus, there is the need to further improve the lens performance in such a way that

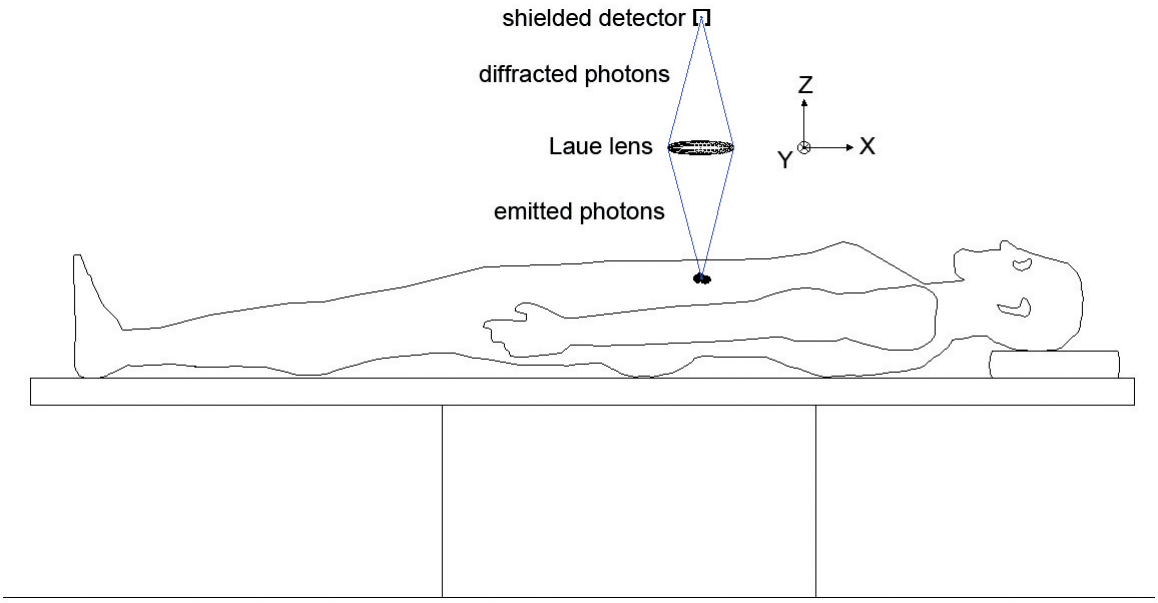

Figure 3.1: Schematic representation of a nuclear diagnostic system equipped with a Laue lens. A fraction of the γ-rays emitted by the radiotracer localized in a specific area of the patient's body are focused on the detector through diffraction in the crystals of the lens.

its clinical use can actually become convenient.

In this chapter, a detailed study and the design principles for a Laue lens devoted to nuclear medicine is presented. The proposed method allows obtaining high-resolution images of small radioactive sources. The resolution can be one order of magnitude better than the level attainable in conventional nuclear medicine exams.

3.2 Lens design principles

The design principles of a Laue lens for astrophysics have been well defined in the literature, see for instance [80, 81, 82]. Even though the requirements of a lens for nuclear medicine and a lens for astrophysics are the same, the design approach differs significantly. Indeed, in the astrophysical case, polychromatic hard X- or γ-rays come from very distant sources and can be considered to be parallel when they impinge on the crystals of the lens. Conversely, in the nuclear medicine case one has to deal with a monochromatic and divergent beam, since γ-photons are emitted in any direction by the radioactive source lying inside the patient's body.

3.2.1 Geometry of the system

A lens composed of concentric rings of crystals is shown in Fig. 3.2.a. It lies at a distance L_S from a γ-ray point source and L_D from a detector. L_S and L_D are called object distance

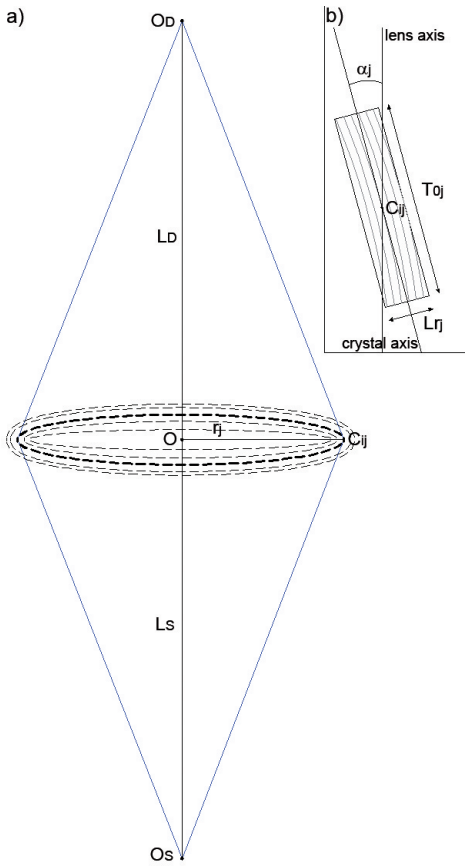

Figure 3.2: Schematic representation of the geometry of the system. a) A point source is positioned in O_S, the lens is placed at a distance L_S from the source and a detector, centered in O_D, is at a distance L_D from the lens. A generic ring of the lens is highlighted, $\overline{OC_{ij}} = r_j$ is the radius of the ring. The crystals of each ring are assumed to be ideantical. b) Detail of the crystal i in the ring j. T_{O_j} is the thickness of the crystal traversed by the photons. α_j is the angle between the crystal axis and the lens axis. In the calculation, we assume that $\alpha_j = 0$.

and image distance respectively. With an appropriate design, the lens can focus the photons toward the image point O_D, providing a point-to-point imaging.

First, the energy E of the monochromatic source and the object distance L_S have to be set. Then, the lens geometry can be determined. The lens is formed by N rings, each of them exploiting a different set of crystalline planes and/or a different crystalline material. The crystals of each ring are assumed to be identical. To obtain the diffraction of the photons, the radius of the j-th ring, r_j, has to be set according to

$$L_S = \frac{r_j}{\tan(\theta_{B_j} - \alpha_j)}, \tag{3.1}$$

where α_j is the angle between the crystal axis and the lens axis (see Fig. 3.2.b). The photons diffracted by each crystal are focused toward the point 0_D if the image distance is

set to

$$L_D = \frac{r_j}{\tan(\theta_{B_j} + \alpha_j)}. \tag{3.2}$$

Under small-angle approximation, $\tan\theta_{B_j} \approx \sin\theta_{B_j} \approx \theta_{B_j}$, it is possible to obtain the same equation for thin lenses in visible optics [83]

$$\frac{1}{L_S} + \frac{1}{L_D} = \frac{1}{f}, \tag{3.3}$$

where f is the focal length of the lens, namely the distance from the ring to the focus for a distant source

$$f = \frac{r_j}{\tan(2\theta_{B_j})}. \tag{3.4}$$

The source-to-detector distance, $L_S + L_D$, is minimum when $\alpha_j = 0$, namely when the crystals are perfectly aligned with the lens axis. Since the system should be as compact as possible, hereinafter we will assume that this condition is fulfilled. Moreover, we will always use the small-angle approximation. Therefore, it follows that

$$\frac{r_j}{\theta_{B_j}} = L_D = L_S. \tag{3.5}$$

By combining equations (3.5) and (1.4), the radius of the j-th ring can be written as

$$r_j = \frac{h_p c}{2a}\frac{L_S}{E}\sqrt{h^2 + k^2 + l^2}. \tag{3.6}$$

Therefore, once the material and the lattice plane (hkl) used for a ring have been set, the ring radius is determined. The higher the Miller indices the larger the ring radius. For what concerns the arrangement of the crystals in each ring, we assume the polygonal arrangement that best approximates the ring, i.e. the polygon inscribed in the circle with radius $(r_j - L_{r_j}/2)/\cos(\pi/n_j)$. To determine the number of crystals in each ring, the tangential length L_{t_j} and the radial length L_{r_j} have to be set. The latter has been already shown in Fig. 3.2.b, while L_{t_j} is the size of the side orthogonal to the plane of the figure. The number of crystals in each ring, n_j, turns out to be

$$n_j = \frac{\pi}{\arctan\left(\frac{L_{t_j}}{2r_j - L_{r_j}}\right)}. \tag{3.7}$$

Not all the lattice planes (hkl) can be selected for a given material and size because different crystals would occupy approximately the same position in the lens. This limitation becomes more severe as L_S decreases.

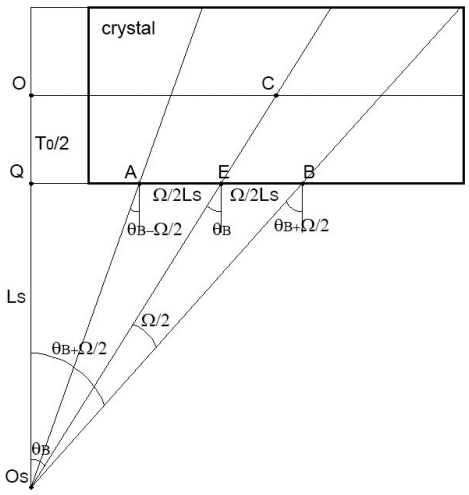

Figure 3.3: Schematic representation of a crystal in a generic ring (not to scale). $\overline{OC} = r$ is the radius of the ring. The crystal diffracts the photons emitted with a polar angle θ within the range $[\theta_B - \Omega/2, \theta_B + \Omega/2]$, where Ω is the crystal acceptance.

3.2.2 Efficiency calculation

Type and thickness of the crystals have to be set to optimize the lens performance. An important figure of merit is the lens efficiency. It is defined as the ratio between the number of photons with energy E diffracted per second by the lens and the number of photons with energy E emitted per second by the source. The latter quantity is given by the product of the source activity and the probability of emission of the considered γ-line. Even if the lens efficiency is a dimensionless quantity, it can be expressed in cps/Bq, which is the unit of measurement used in nuclear medicine. Indeed, the number of counts per second (cps) of the signal on the detector is equal to the number of photons diffracted per second by the lens, provided that the air absorption is neglected, an ideal detector is considered, and the counts due to the background and to the not coherently scattered photons are subtracted. Furthermore, in nuclear medicine the ratio described above is often called sensitivity. Thus, for our purposes, the two terms are considered as synonyms.

The efficiency of the lens is strictly related to the integrated reflectivity of the crystals that compose the lens. Let us consider Fig. 3.3, which sketches a crystal in a generic ring. The crystal diffracts only the photons emitted with a polar angle θ belonging to the interval $[\theta_B - \Omega/2, \theta_B + \Omega/2]$. Ω is the angular acceptance of the crystal and is considered to be equal to the FWHM of its rocking curve. This is exact if a CDP crystal is considered, but is only an approximation for a mosaic crystal. Likewise, the integrated reflectivity of a mosaic crystal is considered to be simply the product of the peak reflectivity and the angular acceptance as in the case of a CDP crystal. These approximations allow us to

develop our analytical calculation in the same way for both types of crystal. It is possible to notice that not all the crystal volume diffracts the photons emitted by a point source. Equivalently, not all the surface on which the photons impinges acts as collecting area. Since $\overline{O_S Q} = \overline{O_S O} - \overline{QO} = L_S - T_0/2 \approx L_S$, by considering the 2 triangles $O_S\hat{Q}E$ and $O_S\hat{Q}B$, it can be calculated that $\overline{AE} = \overline{EB} = \Omega/2L_S$. Therefore, the collecting area of the crystal is $L_S\Omega L_t$. Since $L_S\Omega < L_r$, the collecting area is smaller than the geometric area $L_r L_t$. The collecting area of each ring is equal to the number of crystals n_j times their collecting area

$$A_{c_j} = n_j L_S \Omega_j L_{t_j}. \tag{3.8}$$

The effective area of each ring is defined as the collecting area of the ring times the reflectivity of the crystals. The effective area of the lens is the sum of the effective area of the N rings

$$A_{eff} = \sum_{j=1}^{N} A_{eff_j} = \sum_{j=1}^{N} A_{c_j} R_j, \tag{3.9}$$

R_j being the peak reflectivity of the crystals in the j-th ring. If $\dot{N}_S$ is the number of γ-photons per second emitted by the point source, the photon flux on the lens is $\dot{\Phi}_L = \frac{\dot{N}_S}{4\pi L_S^2}$. Hence, the number of photons per second diffracted by the lens is $\dot{N}_D = \dot{\Phi}_L A_{eff}$. Therefore, the efficiency of the lens can be written as

$$\epsilon = \frac{\dot{N}_D}{\dot{N}_S} = \frac{A_{eff}}{4\pi L_S^2} = \frac{1}{4\pi L_S^2} \sum_{j=1}^{N} A_{c_j} R_j. \tag{3.10}$$

It follows that

$$\epsilon = \frac{1}{2} \sum_{j=1}^{N} \frac{n_j L_{t_j}}{2\pi L_S} \Omega_j R_j = \frac{1}{2} \sum_{j=1}^{N} \frac{n_j L_{t_j}}{2\pi r_j} \theta_{B_j} \Omega_j R_j. \tag{3.11}$$

Since

$$\frac{n_j L_{t_j}}{2\pi r_j} \approx 1, \tag{3.12}$$

we obtain

$$\epsilon = \sum_{j=1}^{N} \epsilon_j = \frac{1}{2} \sum_{j=1}^{N} \theta_{B_j} \Omega_j R_j. \tag{3.13}$$

The efficiency of a ring is approximately given by

$$\epsilon_j = \frac{1}{2} \theta_{B_j} \Omega_j R_j. \tag{3.14}$$

In a first approximation, ϵ_j does not depends on L_S, nor on n_j, nor on the surface on which the photons impinge. Indeed, by raising the object distance, a larger number of crystals

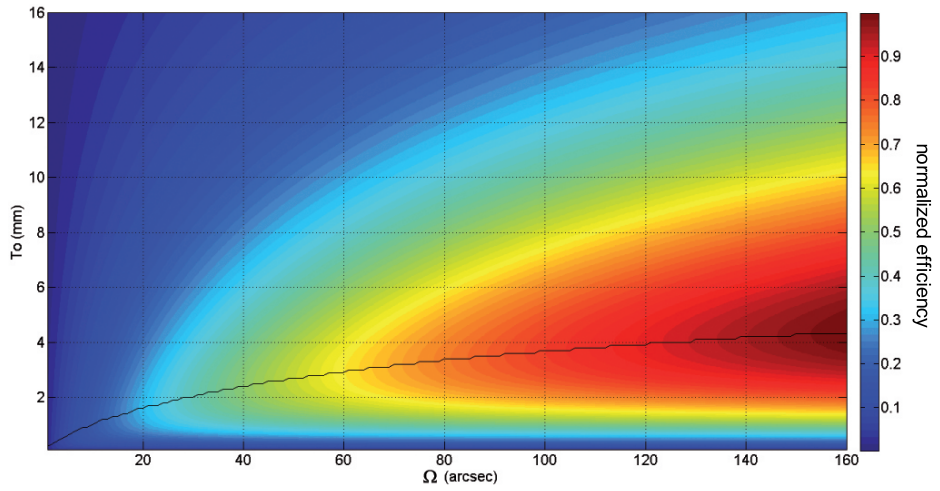

Figure 3.4: Normalized efficiency at 140.5 keV of a ring exploiting the planes (111) of Ge crystals, as a function of the thickness and the acceptance of the crystals. The solid black lines gives the optimum thickness as a function of the acceptance Ω.

can be arranged in each ring. Thus, an increase in A_{eff} can be obtained. However, this gain is approximately compensated for by the decrease in the photon flux hitting the lens. Conversely, ϵ_j depends on the Bragg angle, on the acceptance, and on the thickness of the crystals. For a ring of crystals of a given material and a given set of lattice planes, Ω_j and T_{0_j} are 2 free parameters that can be chosen to maximize the efficiency of the ring.

To proceed further in the analysis, highly-curved crystals are considered. In this case, dropping the subscript j and using equation (1.19), the efficiency of a generic ring assumes the form

$$\epsilon = \frac{1}{2}\theta_B\Omega(1 - e^{\frac{-\pi^2 d_{hkl}}{\Lambda_0^2}\frac{T_0}{\Omega}})e^{\frac{-\mu T_0}{\cos\theta_B}}. \tag{3.15}$$

Since $\cos\theta_B \approx 1$, efficiency depends almost linearly on θ_B. However, by equation (1.4) it follows that a higher value of the Bragg angle implies higher indices and hence higher value of Λ_0, leading to a decrease in the ring efficiency. For this reason, the outermost rings in the lens gives a small contribution to the overall efficiency. As a result, it is not convenient to increase the number of rings over a certain value, which depends on the specific case. Otherwise, there would be only an increase in the lens complexity without an appreciable increase in the lens efficiency.

Fig. 3.4 plots the efficiency at 140.5 keV of a ring exploiting the planes (111) of Ge crystals. The acceptance has to be as high as possible to maximize the efficiency of the ring. Moreover, for each value of Ω, there is a relatively narrow range of thickness T_0 for which the efficiency attains its maximum value.

Another parameter which is generally used to quantify the diffraction capability in the

whole lens, especially those for astrophysics, is the lens diffraction efficiency, which has not to be confused with the crystals diffraction efficiency. The lens diffraction efficiency is defined as the ratio between the number of photons per second diffracted by the lens $\dot{N}_D$ and number of photons per second incident on the lens $\dot{N}_L$. It turns out

$$\epsilon_D = \frac{\dot{N}_D}{\dot{N}_L} = \frac{A_{eff}}{A_L}, \tag{3.16}$$

where $A_L = \sum_{j=1}^{N} n_j L_{t_j} L_{r_j}$ is the geometric area of the lens.

3.2.3 Point Spread Function calculation

The Point Spread Function (PSF), i.e. the system response to a point-like source, is the physical quantity that fully characterizes an imaging system. Indeed, the image of a extended source is obtained by the convolution of its spatial distribution and the PSF of the system [84]. The PSF of the system is given by the convolution of the PSF of each individual element that contributes to the formation of the image. In our case, only the lens and the detector contribute to the formation of the image. Thus, for an ideal detector, the PSF of the system coincides with the PSF of the lens. The spatial resolution of the system is defined as the FWHM of its PSF. This quantity affects the capability to distinguish small details of the image and hence has to be as small as possible.

An ideal situation would be if the crystals, other than possessing the curvature of the planes of diffraction, were bent to perfectly fit in the ring in which they are positioned (sagittal focusing [83]). In this case, a perfect focusing into a single point could be achieved. Unfortunately, due to mechanical stiffness of the crystals, this condition cannot be met and each crystal focuses only in one direction. Therefore, on the image plane, where the detector is positioned, the distribution function of the incoming photons is spread out around the center O_D. This spread, and hence the lens resolution, depends on several parameters.

If the lens is composed of highly-curved crystals disposed under Laue symmetric geometry, the photon trajectories and their distribution on the detector can be calculated. Because of the variation of the orientation of the lattice planes due to the curvature, a photon penetrates into the crystal until the zone where the Bragg condition is satisfied. Such a zone is narrow enough that the photon trajectory undergoes a kink [26]. Therefore, each photon is diffracted only once and then proceeds along its trajectory undergoing normal absorption. These are the conditions provided by the kinematic theory.

Let us consider the situation sketched in Fig. 3.5. A photon impinges on the surface of a crystal with azimuthal angle equal to zero. The coordinates of the diffraction point in a

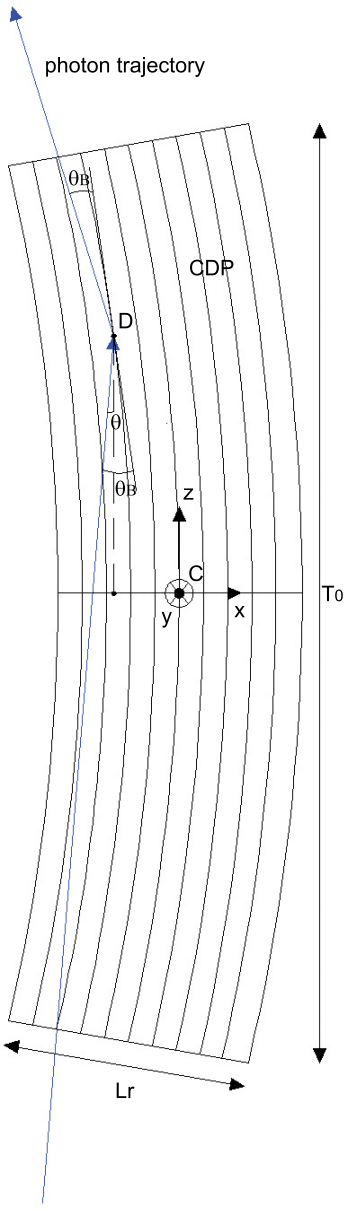

Figure 3.5: Schematic representation of diffraction in a highly-curved crystal under Laue symmetric geometry. The kink of the trajectory is due to the large variation of the lattice planes orientation over a distance equal to the extinction length.

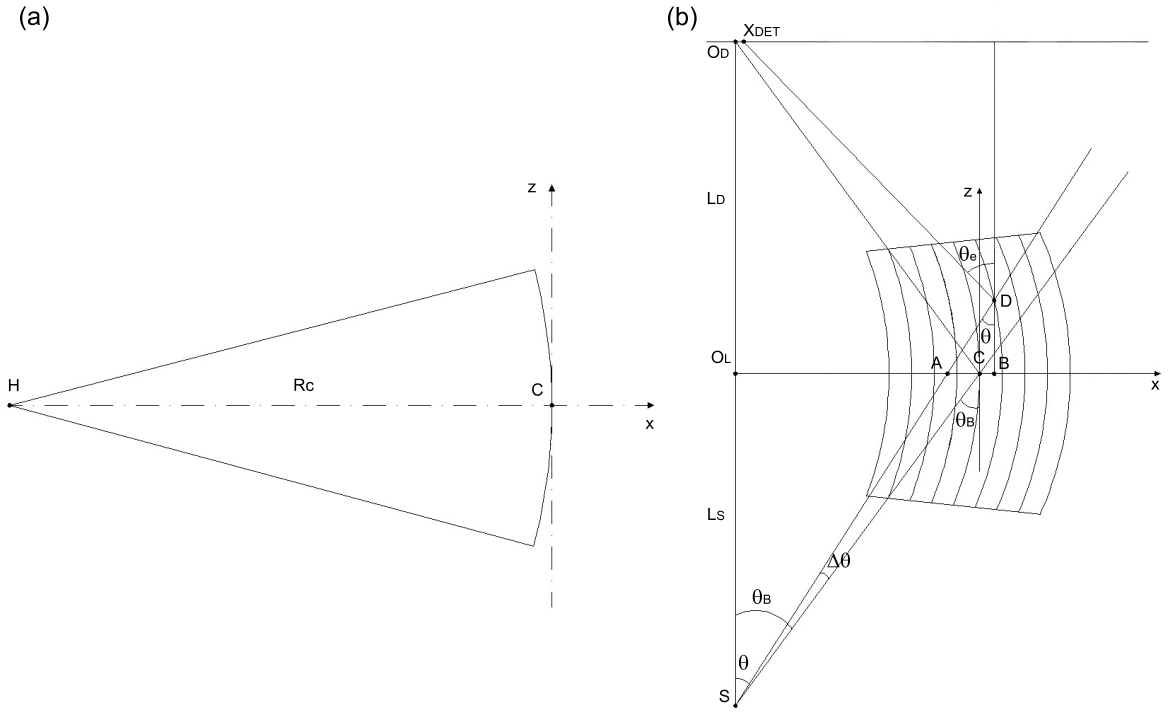

Figure 3.6: Diffraction in a highly-curved crystal under Laue symmetric geometry. (a) $R_C = \overline{HC}$ is the radius of curvature of the diffracting planes. (b) Trajectory of the photons with azimuthal angle equal to zero.

frame with origin at crystal centre can be calculated as

$$y_D = 0, \tag{3.17}$$

$$z_D = -\frac{T_0}{\Omega}\Delta\theta, \tag{3.18}$$

$$x_D = -\Delta\theta(\frac{T_0}{\Omega}\theta - L_S). \tag{3.19}$$

The equation that expresses the z-coordinate of the diffraction point z_D can be demonstrated as follows. Curved diffracting planes under Laue symmetric geometry can be described through $x = k - z^2/(2R_C)$, where k is a real parameter and $\overline{HC} = R_C = T_0/\Omega$ the radius of curvature of the diffracting planes (Fig. 3.6.a shows the plane obtained if $k = 0$). This equation represents a family of parabolas with the x-axis as the symmetry axis. The variation of orientation of the diffracting planes due to the curvature, along the direction of propagation of the photon beam, is $dx/dz = -z/R_C \approx \alpha$. By identifying α with $\Delta\theta = \theta - \theta_B$ we have equation (3.18). The expression of x_D can be obtained through a series of trigonometric calculations. In fact, from Fig. 3.6.b, it follows that $x_D = \overline{CB} = \overline{AB} - \overline{AC}$. Since $\overline{AB} \approx z_D\theta$ and $\overline{AC} = \overline{O_LC} - \overline{O_LA} = \theta_B L_S - \theta L_S = -\Delta\theta L_S$, we have $x_D = z_D\theta + \Delta\theta L_S$ and, substituting the expression of z_D, equation (3.19). It is worth noting that, if $\Delta\theta = 0$, diffraction occurs at the origin of coordinates, namely at the middle of the crystal, as ex-

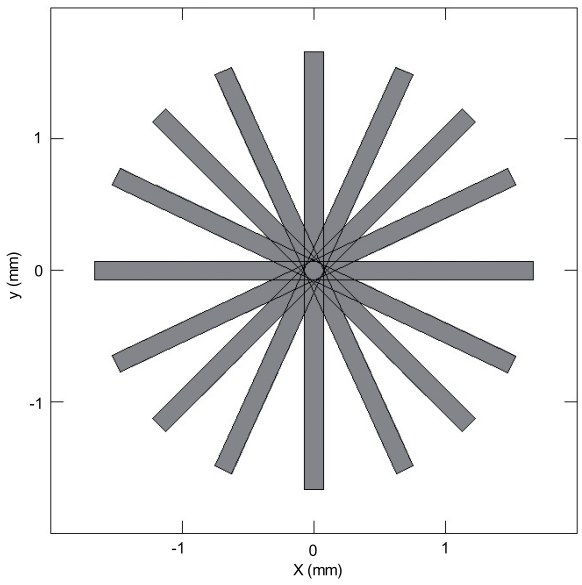

Figure 3.7: Composition of the crystal images on the plane at a distance $L_D = L_S$ from the lens. A lens composed of 1 ring with 16 crystals is considered. Assuming a perfect alignment, the images of crystals located in diametrically opposite points overlap perfectly.

pected.

The distance of the arrival point of the photons on the detector, with respect to O_D, turns out to be

$$x_{DET} = r + x_D - (L_D - z_D)\theta_e, \tag{3.20}$$

where r is the radius of the ring to which the crystal belongs and $\theta_e = \theta_B - \Delta\theta$. Since $L_D = L_S$, by considering all the possible values for the polar angle θ, the image obtained on the detector is a line of width $|2T_0\theta_B - 2\Omega L_S|$. Due to the focusing effect provided by curved diffracting planes, this value is lower than the radial size of the crystal L_r. Furthermore, including in our analysis the photon azimuthal angle, it is possible to see that a point source produces a rectangle with sides $|2T_0\theta_B - 2\Omega L_S|$ and $2L_t$ as an image of each crystal (see Appendix B). The PSF of the lens can be estimated by taking into account such contribution for all crystals in each ring (see Fig. 3.7). In the next section, a specific lens will be considered and its PSF shown. The FWHM of the PSF depends on the object distance, on the Bragg angle of each ring, on thickness and on the acceptance of the crystals. Conversely, the tails of the PSF are basically determined by the tangential side of the crystals.

The PSF can also be calculated if the lens is composed of mosaic crystals [85]. In this case, the width of the image spot is at least equal to the radial size of the crystals L_r and becomes larger, due the so-called mosaic defocusing, as L_S increases over the value $\sqrt{2\ln(2)}L_r/m$, m being the mosaicity of the crystals [15]. Therefore, the image resolution attainable with a lens composed of CDP crystals is much better than for a lens composed

of mosaic crystals.

A parameter that combines efficiency and focusing capability of a lens is the focusing factor G. It is defined as [81]

$$G = f_{ph}\frac{A_{eff}}{A_D}, \tag{3.21}$$

A_{eff} being the effective area of the lens and A_D the area of the spot on the detector that contains a fraction f_{ph} of photons reflected by the lens.

3.2.4 Field Of View estimation

The Field Of View (FOV) of the lens is the portion of space within which a source has to lie so that it can be correctly reproduced on the image plane. In particular, we consider only the portion of space within which the lens response is stationary, namely it does not depend on the source position. This issue can be precisely addressed by a numerical simulation. However, an estimation can be performed as follows. Let us consider a Laue lens composed of crystals of the same type and size. Let us also assume that $L_r \leq L_t$. If a point source is positioned in O_S, the lens provides a point-to-point imaging with a blur given by the the lens resolution. If the point source is moved away from O_S, the lens diffracts the photons with no efficiency loss nor blur increase only if the transaxial displacement is approximatively lower than $L_r/2$. Beyond this distance, diffraction may not occur for some polar angles within the nominal acceptance range. Indeed, through a modified version of equation (3.19) which includes the source shift and the azimuthal angle contribution (see Appendix B), it is possible to calculate that the diffraction point lies outside the crystal. Since the lens transaxial FOV is approximately given by the radial side of the crystals, there is a trade-off between the need for small L_r (to enable the diffraction from all the desired planes) and the need for a large value of L_r (to magnify the transaxial FOV). The axial FOV of the lens is far broader than the transaxial one. Indeed, it is approximatively equal to $\Omega_1 L_S/\theta_{B_1}$, θ_{B_1} being very small.

3.2.5 Response of the lens vs. energy

A lens designed for a specific monochromatic source can be also used with different sources. Indeed, equation (3.6) settles a proportionality relationship between E and L_S. Thus, if the source energy changes, the object and the image distances have to be set accordingly. However, the lens efficiency and resolution change as well.

The efficiency worsens at high energy. Indeed, the crystal thickness should be increased to maintain a high value of reflectivity. Furthermore, even if one considers the optimum

Table 3.2: Features of the proposed Laue lens

E	140.5 keV
L_S	0.25 m
L_D	0.25 m
N	10
crystals	Ge (CDP)
T_0	5.0 mm
L_t	1.0 mm
L_r	1.0 mm
R_C	11.5 m
Ω	90 arcsec

thickness, the lower Bragg angle leads to an increase in Λ_0 and hence to a decrease in diffraction efficiency at high energy. Such decrease is stronger than the increase in the absorption factor and, as a result, the reflectivity decreases.

The shape of lens PSF also changes with energy. Indeed, it depends on L_S and on the Bragg angles of each ring and, in turn, these physical quantities vary with energy. As will be shown in the next section, there is an energy range within which the resolution assumes its best value. However, this condition leads to a smaller fraction of photons enclosed by a circle with diameter equal to the FWHM of the PSF.

3.3 Proposal of a high-resolution lens

In this section, the design of a Laue lens for high-resolution diagnostic nuclear medicine using the 140.5 keV γ-lines from ^{99m}Tc is illustrated. The object distance L_S is set to 25 cm.

We consider a lens composed of 10 rings of CDP Ge crystals whose transaxial size is 1.0 $\times$ 1.0 mm. Furthermore, we take under consideration crystals with a radius of curvature of 11.5 m. In the previous section, it has been shown that each ring should be composed of crystals with different thicknesses. However, in this case, the optimum thickness does not change very much from one ring to another. Thus, for the sake of simplicity, we set the thickness of all the crystals to be 5.0 mm. Their angular acceptance turns out to be 90 arcsec. Finally, we consider a symmetric Laue geometry and a perfect crystals alignment. The features of the lens are summarized in Table 3.2.

For each ring, the lattice planes, the radius, and number of crystals exploited are listed in Table 3.3. By using such diffracting planes, the lens assumes the geometry depicted in Fig. 3.8. The lens is very compact, having a diameter of 3.4 cm. Through equation (3.11), the lens efficiency turns out to be about 1×10^{-5}, which is lower than the levels for SPECT and PET and is indeed comparable to that of a pinhole SPECT. The efficiency of the proposed

Table 3.3: Rings of proposed Laue lens

ring	lattice planes	number of crystals	radius
1	(111)	18	3.38 mm
2	(220)	31	5.52 mm
3	(400)	45	7.80 mm
4	(422)	56	9.56 mm
5	(440)	66	11.04 mm
6	(620)	74	12.35 mm
7	(444)	81	13.53 mm
8	(642)	88	14.61 mm
9	(800)	95	15.63 mm
10	(751)	103	16.92 mm

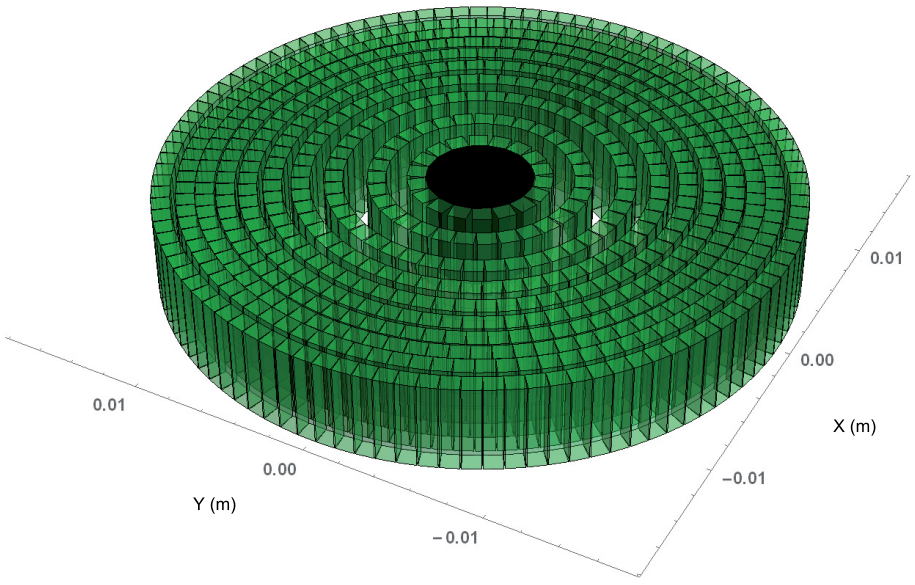

Figure 3.8: Perspective view of the designed lens. The black central disk represent an absorber that stops the direct beam near the lens axis. The photons passing through the voids between the rings do not reach the sensitive volume of the detector.

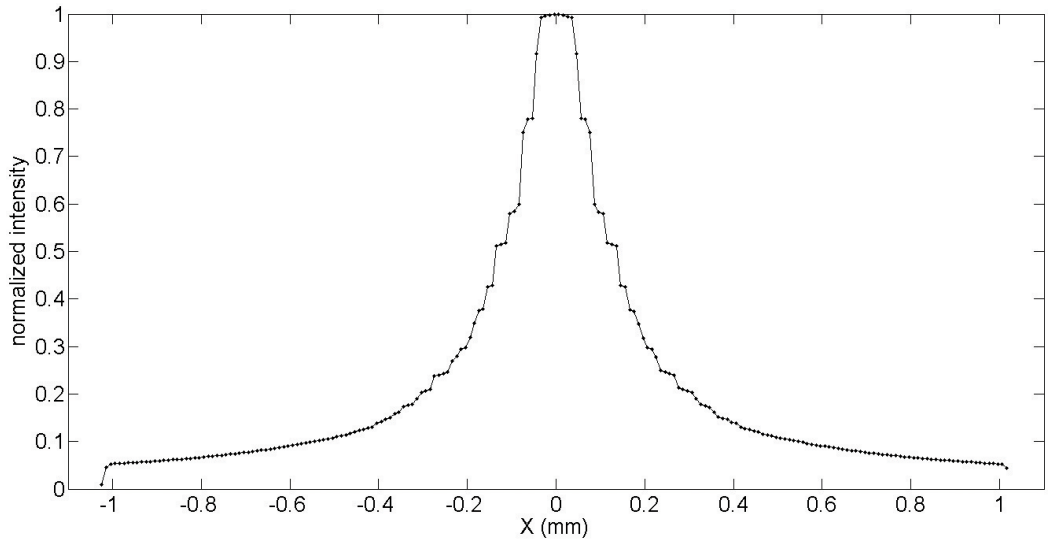

Figure 3.9: Section of the lens PSF along the X axis of the image plane.

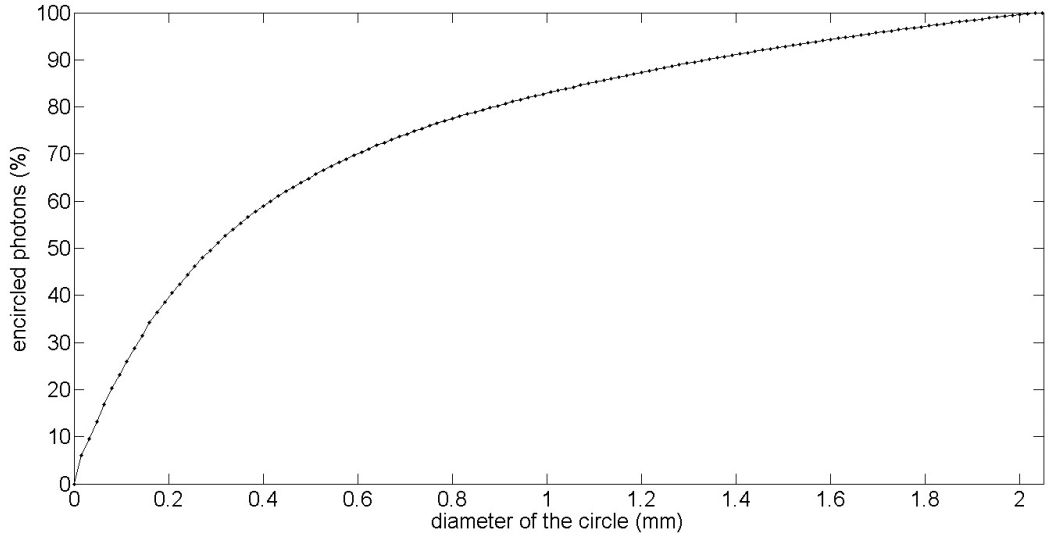

Figure 3.10: Fraction of the diffracted photons enclosed by a circle of increasing diameter.

lens is also of the same order of magnitude if compared with the already realized prototypes [17, 18].

By application of the method exposed in the previous section, the PSF of the lens can be calculated. It is a function of the 2 coordinates on the image (detector) planes. However, due to the nearly perfect rotational symmetry of the lens, a section along any axis can be considered. Fig. 3.9 shows the section of the PSF along the X axis.

The majority of the photons are focused near to the image point O_D. Indeed, the FWHM of the curve is 0.30 mm and the number of the diffracted photons enclosed by circle whose diameter is 0.30 mm is about 50%. Furthermore, a spot of 0.84 mm contains 80% of the diffracted photons. Fig. 3.10 plots the fraction of the diffracted photons, f_{ph}, enclosed by a

Table 3.4: Lens performance at 140.5 keV

Number of crystals	657
Lens diameter	3.4 cm
Filling Factor	71%
Diffraction efficiency	1.2%
Efficiency	1×10^{-5}
Resolution	0.30 mm
f_{ph} at 0.30 mm	50%
$d_{80\%}$	0.84 mm
$G_{80\%}$	8

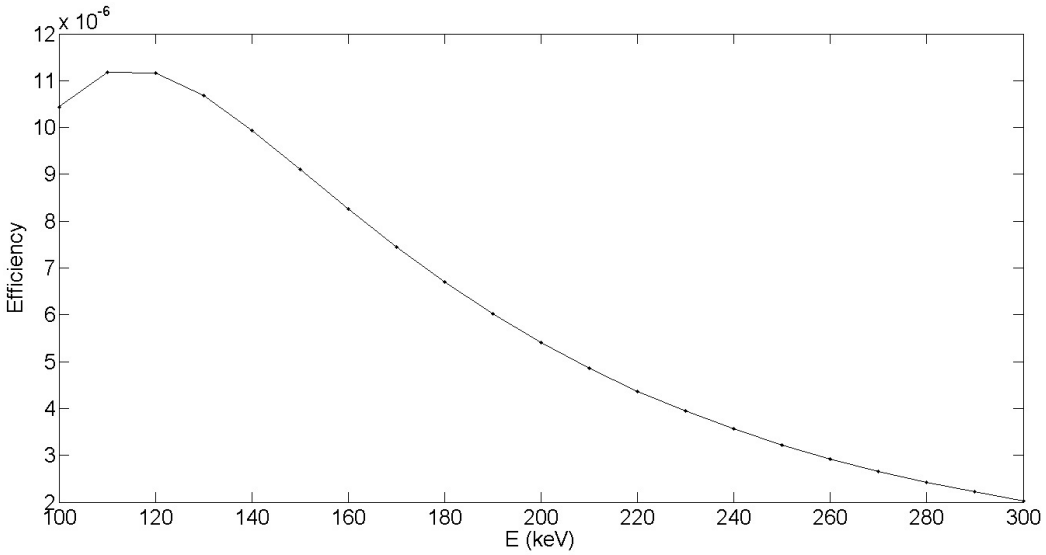

Figure 3.11: Efficiency of the lens as a function of source energy.

circle of increasing diameter $d_{f_{ph}}$.

Due to the focusing power of the lens, a very low blur in the image of a point source is guaranteed. A resolution of 0.30 mm would be an outstanding performance for a technique in nuclear medicine. This value is one order of magnitude better than that obtainable with PET and it can be only approached by some pinhole SPECTs, but in such cases, the efficiency would be far lower than for the lens described here.

The lens performance at 140.5 keV is summarized in Table 3.4.

Finally, the efficiency and the resolution of the lens as a function of energy are shown in Fig. 3.11 and Fig. 3.12 respectively. As claimed in the previous section, the efficiency decreases monotonically at high-energy due to the decrease in reflectivity of the crystals.

The PSF of the lens varies vs. energy because of the variation of L_S and of the Bragg angle relative to each ring. When the condition for best resolution occurs, a smaller fraction of diffracted photons is enclosed by a circle with diameter equal to the FWHM of the PSF. Furthermore, the diameter of a circle enclosing 80% of diffracted photons is larger.

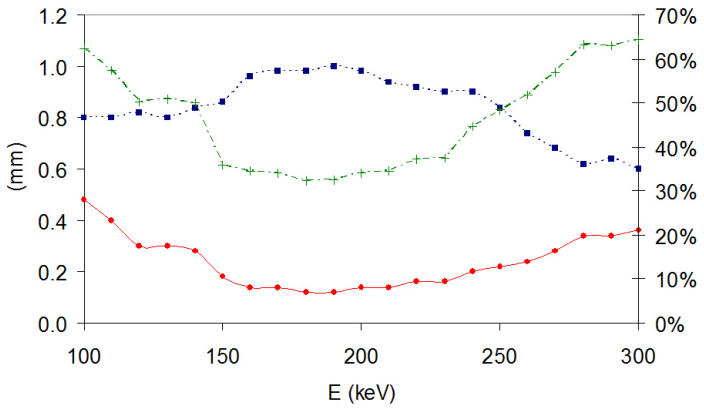

Figure 3.12: Characteristic parameters of the lens PSF as a function of the source energy. Red circles joined by the red solid line plots the resolution (FWHM of the PSF) of the lens (mm). Green crosses joined by the green dot-dashed line plots the fraction of photons enclosed by a circle whose diameter is equal to the FWHM of the lens PSF. Blue squares joined by the blue dotted line plots the diameter of the circle (mm) that encloses 80% of diffracted photons.

It can be argued that the lens is still usable when other monochromatic sources are considered. Naturally, the best performance is achieved at the energy for which the lens has been designed.

3.4 Imaging capabilities of a Laue lens for nuclear medicine

In order to achieve an in-depth knowledge about the imaging capabilities of a Laue lens for nuclear medicine, several Monte Carlo simulations were performed through a custom-made code named LAUENM (see Appendix B for details). The code, which is implemented in Matlab language [86], enables one to design the lens and to simulate the diffraction process. The lens can be composed of crystals of different material and different structure (CDP or mosaic). The code is modular and each module faces a particular task. A specific module manages the photon source, which can take various shapes and activity distributions. The photons are emitted randomly in direction. The same module works out the lens geometry starting from the input parameters set by the user. The main processing module manages the interaction of the photons with the crystals and calculates the arrival point of the photons on the detector. Finally, a post-processing module, taking into account the detector feature, computes the obtained image and all the figures of merit regarding the lens.

A series of simulations were carried out considering a lens with 10 rings composed of 5 mm thick CDP Ge crystals with 1.0 × 0.5 mm traversal size and curved diffracting planes with a radius of curvature radius of 11.5 m.

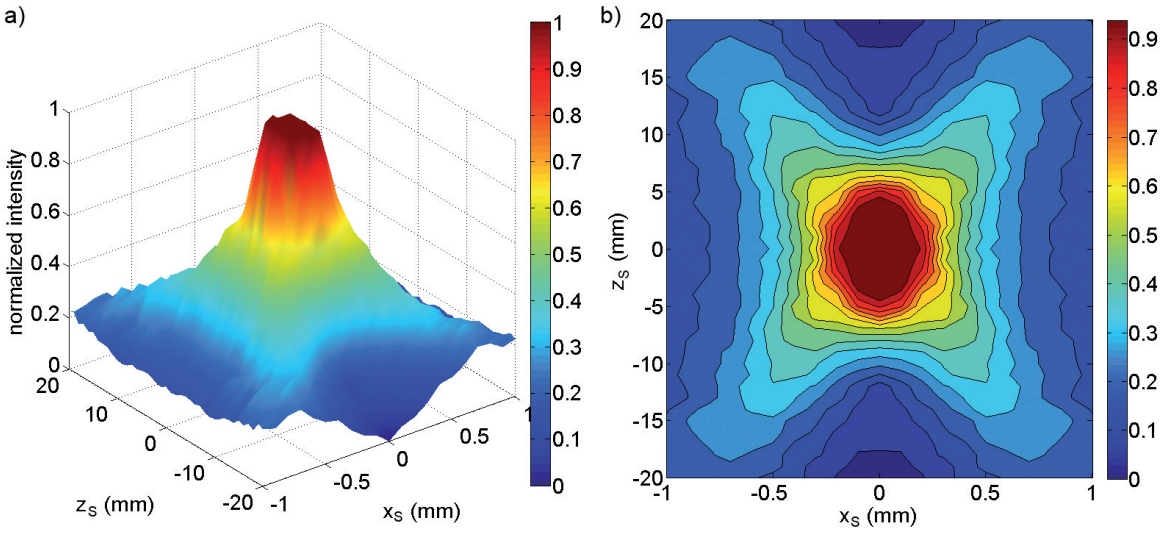

Figure 3.13: a) Normalized efficiency of a lens composed of crystals with 1.0 × 0.5 mm traversal size as a function of x_S and z_S. b) Contour of the normalized lens efficiency.

First, the lens FOV was calculated as follows. The lens efficiency was recorded as a function of the position of a point source. In particular, the source was moved along a transaxial direction and along the axial direction, namely along the axes x_S and z_S of a frame centred at O_S. Fig. 3.13 plots the normalized lens efficiency as a function of x_S and z_S. It is possible to recognize that within a transaxial distance equal to 0.25 mm from O_S there is no efficiency decrease. This distance corresponds to $L_r/2$. The axial distance within which there is no efficiency decrease is approximatively equal to 4.0 mm, which corresponds to $\Omega_1 L_S/2\theta_{B_1}$. It is worth noting that over these distances the response does not vanish, but undergoes a progressive loss accompanied by an increase in the photon spread. This affects the ability of obtaining a correct image of the source. Hence, the FOV of the lens has to be considered limited to the value within which the normalized efficiency is 1, to be capable of reconstructing the image of an extended source. Fig. 3.14 summarizes the images obtained when various source configurations are considered. The background and the not coherently scattered photons are neglected and an ideal detector with 100% efficiency and 40 × 40 μm^2 pixel is considered. Fig. 3.14.a plots the image obtained in the nominal configuration, i.e. with a point source positioned in O_S. Fig. 3.14.b plots the image related to a point source positioned in y_S = -0.2 mm, which is a point inside the FOV of the lens. It can be seen that an exact image of the source is reproduced on the detector. Fig. 3.14.c plots the image related to a point source positioned in x_S = +0.4 mm, a point outside the FOV of the lens as defined above. In this case is still possible to recognize that the peak of the photon distribution is centred at X = +0.4 mm. However, there is a broadening of the peak and an asymmetry in the tails, which are much more extended in the opposite direction with respect

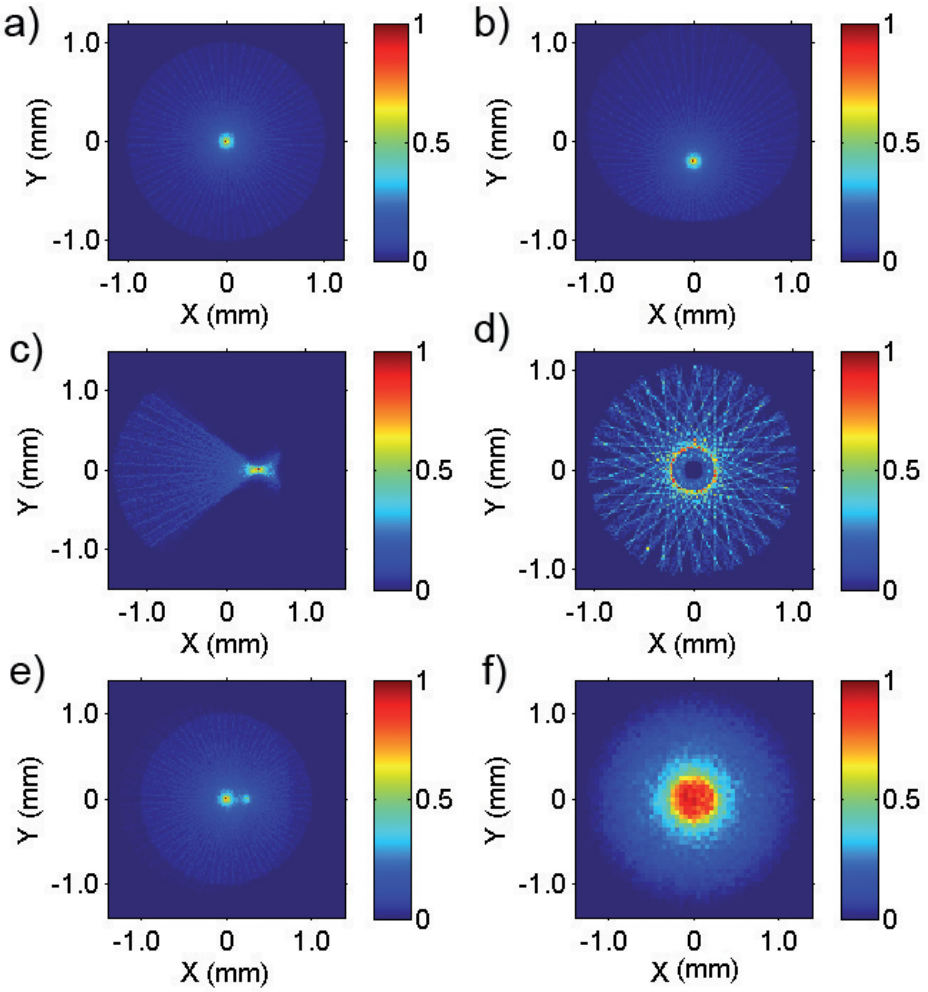

Figure 3.14: Images, on a ideal detector, provided by a lens composed of crystals with 1.0 × 0.5 mm traversal size. Various source configuration are considered. a) Point source positioned in O_S. b) Point source moved 0.2 mm transversely (along y_S) with respect to O_S. c) Point source moved 0.4 mm transversely (along x_S) with respect to O_S. d) Point source moved 10 mm axially (along z_S) with respect to O_S. e) Two point sources of different activity are considered, one in O_S and the second, having an activity equal to one half with respect to the former, moved 0.25 mm along x_S. f) Circular source with a radius of 0.32 mm.

to the source shift and are almost absent in the perpendicular direction. This asymmetry makes it very difficult to reconstruct the image when an extended source is considered. In Fig. 3.14.d the point source is moved 10 mm axially with respect to O_S, thus it is outside the FOV. Due to the fact that the part of the crystals closer to the lens axis does not diffract almost any photon, a central hole appears, making the image reconstruction impossible. In Fig. 3.14.e 2 point sources with different activity are considered. One is centred at O_S and the other, having an activity equal to one half with respect to the former, is moved 0.25 mm along x_S. Both the sources are perfectly resolved and the activity difference is perceptible. Indeed, both the sources are inside the FOV and are separated by a distance larger than the spatial resolution. Finally, in Fig. 3.14.f it is shown the image of a circular source with a radius of 0.32 mm, which is correctly reproduced.

3.5 Lens-detector coupling

Even if is not the purpose of this work treating the design of the detector used to record the image of the radioactivity distribution inside the patient's body, it is important to highlight the required features and indicate a possible solution.

As previously mentioned, the image recorded by the detector is the convolution of the lens response with the PSF of detector itself. Since the main reason to employ a Laue lens in diagnostic nuclear medicine is to provide high-resolution functional images, it follows that the detector must have a spatial resolution better than that of the lens to not spoil the lens imaging performance. Furthermore, the detector efficiency, namely the number of detected photons over the number of photons impinging on the detector sensitive volume, must be as high as possible at the energy range of interest (100 - 300 keV). Since the transaxial FOV of the lens is narrow, the sensitive area of the detector is required to be relatively small.

Diverse detection strategies can be adopted, pixelated solid state detectors composed of materials with high density and atomic number represent a possible solution. CdTe or CZT (Cadmium Zinc Telluride) pixel detectors were recently proposed for the realization of the focal plane detector for a focusing telescope based on a Laue lens, as they combine high absorption efficiency and good spectral resolution while operating at room temperatures [87, 88]. A detection efficiency of about 50% at 200 keV can be obtained with a thickness of 5-6 mm, while Ge detectors would require a far larger thickness and a proper cooling system.

CdTe/CZT pixel detectors can be also used for medical applications. In order to have a high spatial resolution, the pixel size should be of the order of 100-200 μm. One important

issue that could spoil the spatial resolution is due to Compton scattering. The Compton cross section in CZT crystals at 200 keV is approximately one third of the total cross section. Therefore, the effect of Compton scattering is important at this energy, however it is not really the factor limiting the spatial resolution. Indeed, these kind of events can be recognized with a good reliability and therefore can be corrected by using a logic of coincidence or anti-coincidence. Actually, the main limitation on the achievable spatial resolution is due to the charge sharing effect. Indeed, the cloud of carriers generated due to the photon interaction tends to enlarge by diffusion during the movement under the influence of the collecting electric field. The size of the cloud depends on the distance that the charges travel before being collected and therefore on both the configuration of the collecting field and on thickness of the sensitive volume. The charges could be collected from multiple adjacent electrodes (pixels) and therefore the actual spatial resolution could worsen. However, by using a ratio of the pixel size over the thickness of the order of 0.1 and a sufficiently intense electric field, the spreading of the cloud of carriers can be limited to a value significantly lower than the pixel size. Therefore, the achievable spatial resolution is comparable to the pixel size or better [89].

A further improvement can be achieved by using a more sophisticated detection strategy based on layers of Double Sided Strip Detectors (DSSDs). Because they are position sensitive, these detectors are able to reconstruct the lens response [90].

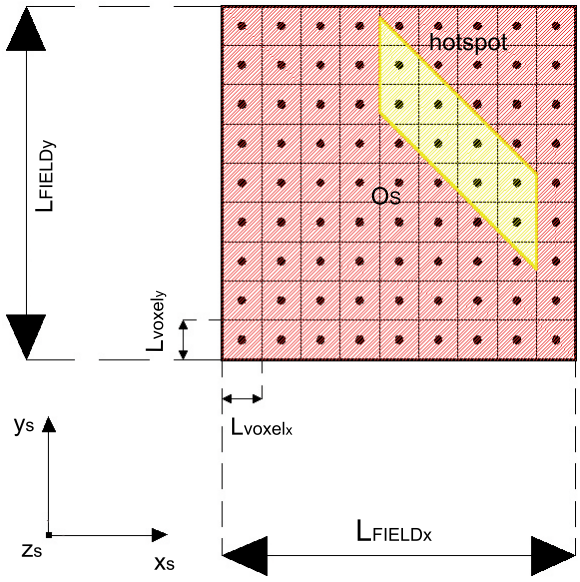

Figure 3.15: Schematic representation of the simulated radioactivity distribution in a portion of the patient's body equal to lens FOV. $L_{FIELD_x} = L_{FIELD_y} = 1$ mm, $L_{VOXEL_x} = L_{VOXEL_y} = 0.11$ mm.

3.6 Images provided by the proposed lens in realistic cases

In order to further highlight the potentiality of a Laue lens for radionuclide imaging, in this section, we show the images recorded by a real detector as they result from the simulations performed considering particular distributions of radioactivity lying inside the patient's body. Two significant cases are treated. The first case involve a complex activity distribution within a portion of space equal to the FOV the lens. In the second case, an extended source requiring a scan to be imaged is considered. In both cases, the optics is the lens proposed in section 2.3 and the source of radiation is the 140.5 keV line from ^{99m}Tc. For the first case the, effect of crystal misalignment is assessed.

3.6.1 Complex activity distribution within the FOV of the lens

Let us consider the source (region under analysis) shown in Fig. 3.15. It is a uniform field of radiation with transversal dimensions L_{FIELD_x} and L_{FIELD_y} both equal to 1 mm and axial dimension equal to 10 mm. Thus, the source is entirely contained within the lens FOV. Inside this volume, there is a small asymmetric region having sharp edges and an activity concentration 10 times higher than the remainder of the volume. The goal of our analysis is to assess how this hotspot is imaged by the lens on a detector with finite efficiency and resolution. The remainder of the volume emits a background radiation, thus it is called background region. In the simulations, the region under analysis is divided in

9×9 voxels with size $0.11 \times 0.11 \times 10$ mm. Each voxel is modeled as a point source isotropically emitting 140.5 keV photons.

In order to estimate the time required to obtain a high-quality image, some concepts have to be introduced. First of all, one has to consider that there is a limitation to the amount of radiotracer that can be given to the patient due to radioprotection constraints. Moreover, only a fraction of the injected activity accumulates in a given tissue. The ratio of the activity in a given tissue over the total injected activity is called *uptake*. Generally speaking, a tumour retains a higher activity concentration because of the increased vascularization, reaching 500 $\mu Ci/cc$ [16].

The hotspot and the background activities can be calculated once the amount of injected radiotracer and the uptake values are known. Concerning the injected activity, we can assume a value of 10 mCi (370 MBq), which is typical for ^{99m}Tc. Furthermore, we can hypothesize an uptake of 0.05 and 0.005 for the hotspot and the background region respectively. In the case of concern, the source has an overall volume of 0.01 cc, whereas the hotspot has a volume of about 0.001 cc. The mean uptake of the region under analysis is

$$\overline{u} = \frac{u_{hs}V_{hs} + u_bV_b}{V}, \tag{3.22}$$

where V is the volume of the region, u_{hs} and u_b are the uptake values for the hotspot and the background respectively, while V_{hs} and V_b are their volumes. The activity of the hotspot A_{hs} and of the background A_b can be calculated solving the following simultaneous equations

$$A_{hs} + A_b = \overline{u}A_i, \tag{3.23}$$

$$\frac{A_{hs}/V_{hs}}{A_b/V_b} = \frac{u_{hs}}{u_b}, \tag{3.24}$$

A_i being the injected activity. The solution of the system is

$$A_{hs} = \frac{n_{hs}u_{hs}}{n_{hs}u_{hs} + n_bu_b}\overline{u}A_i, \tag{3.25}$$

$$A_b = \frac{n_bu_b}{n_{hs}u_{hs} + n_bu_b}\overline{u}A_i, \tag{3.26}$$

where n_{hs} and n_b are the number of voxels of the hotspot and of the background region respectively. The activity involved in the region under analysis is $A = \overline{u}A_i = 37$ kBq. The activities per voxel of the hotspot and of the background region are $A_{hs}/n_{hs} = 2.3$ kBq and $A_b/n_b = 0.23$ kBq respectively. These values are used in LAUENM simulations. Since

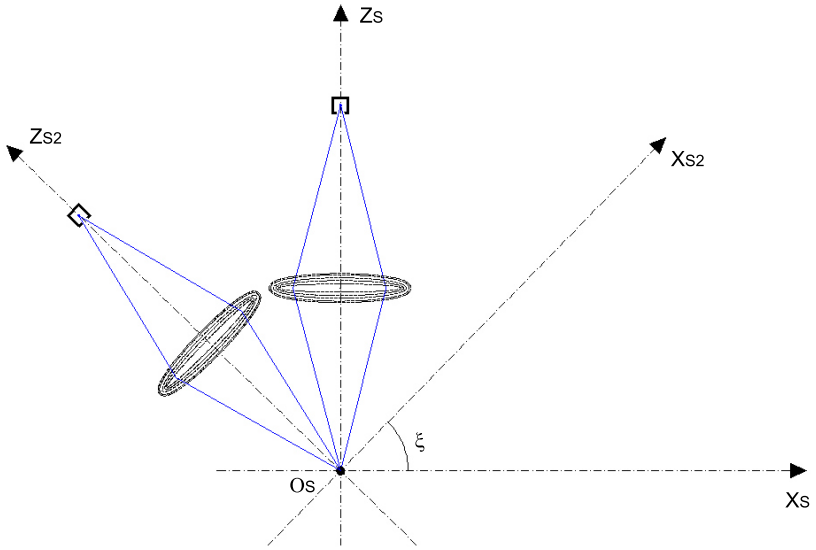

Figure 3.16: Sketch of a diagnostic system composed of two Laue lenses aimed at the same point in order to improve the detection efficiency.

they are quite low and the lens efficiency is 1×10^{-5}, several identical lenses (and detectors) working in parallel according to the scheme depicted in Fig. 3.16 are required in order to obtain a high-quality map of the radioactivity distribution of the region under analysis in a reasonable amount of time.

In order to perform realistic simulations, the effect of Compton scattered photons by the crystals and the effect of the background on the detector are also taken into account. The number of Compton scattered photons reaching the detector is roughly estimated as follows. The geometric area of each ring is approximately given by

$$A_g \simeq \pi((r + L_r/2)^2 - (r - L_r/2)^2) = 2\pi r L_r, \tag{3.27}$$

r being the ring radius and L_r the crystal radial size. Since the flux on a lens is $\dot{\Phi}_L = \frac{\dot{N}_S}{4\pi L_S^2}$, where $\dot{N}_S$ is the number of photons emitted per second by the source, the photons impinging per second on each ring is

$$\dot{N}_g = A_g \dot{\Phi}_L = \frac{r L_r}{2 L_S^2}, \tag{3.28}$$

where L_S is the source-to-lens distance. The number of photons scattered per second by each ring is

$$\dot{N}_c = \dot{N}_g (1 - e^{-\mu_c T_0}), \tag{3.29}$$

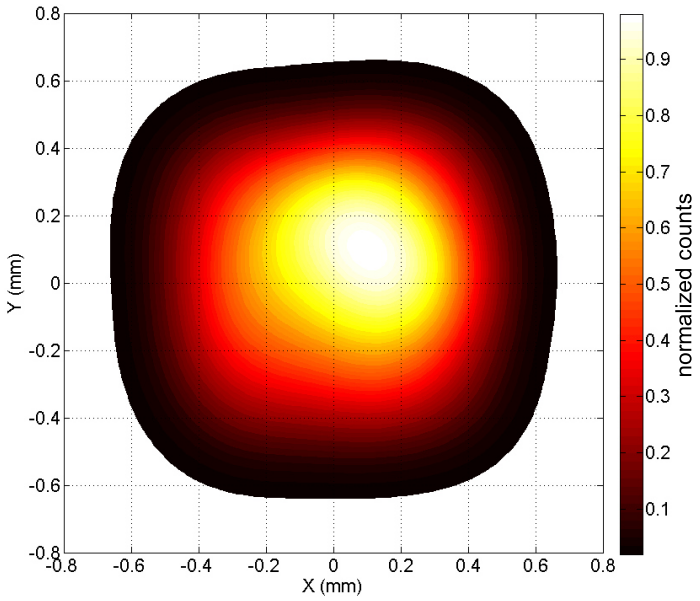

Figure 3.17: Simulated image of the activity distribution inside the region under analysis on a real detector.

where T_0 is the crystal thickness, and μ_c is the linear attenuation coefficient due to Compton effect. The number of photons scattered by all the rings of the lenses composing the imaging system can be obtained summing all the contributions calculated through equation (3.29). Only a small fraction of all the scattered photons reaches the detectors. Because the sensitive area of the detectors is small, we estimate that this fraction is about 1%. These photons are randomly distributed between the pixels of each detector.

Further data required to perform realistic simulations concern the depth at which the region under analysis lies and the nature of the tissue. In this way the the photon absorption can be taken into account. We assume that the region is at a depth of 2.5 cm within an ICRU Four-Component soft tissue, namely a tissue composed of H (0.1%), C (0.11%), N (0.03%), and O (0.76%) [91].

Fig. 3.17 shows the image on a detector with 50% detection efficiency and 200 μm resolution obtained using 14 lenses and a time of acquisition of 20 min as it results form the simulation. As can be seen by comparing Fig. 3.15 and Fig. 3.17, the proposed Laue lens is capable of providing a very good image of the activity within a portion of space entirely contained within the lens FOV, even in the case of a complex distribution such that considered here. This outstanding imaging performance is obtained at cost of an increased complexity of the system. However, it is not achievable through conventional nuclear medicine methods.

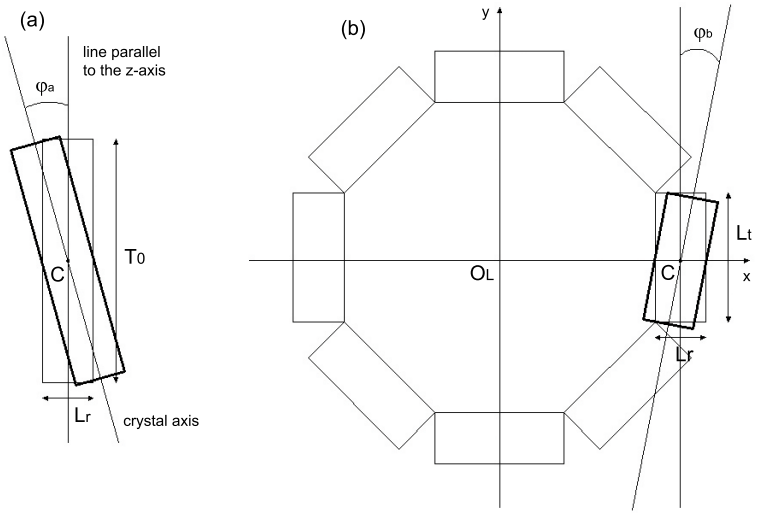

Figure 3.18: Misalignment angles of a crystal lying in a generic ring of a Laue lens. (a) φ_a, (b) φ_b.

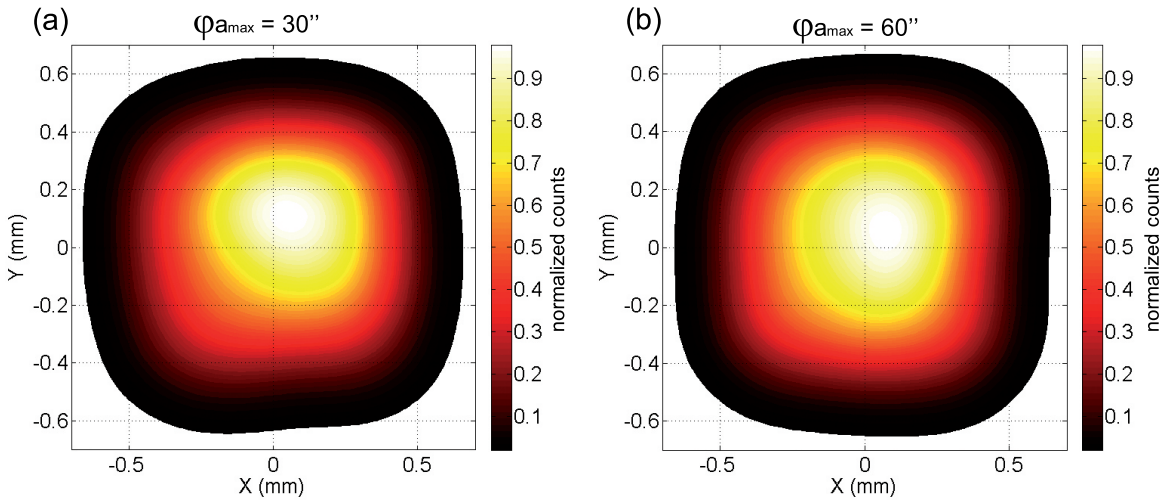

Figure 3.19: Simulated image of the activity distribution inside the region under analysis on a real detector taking into account axial misalignment φ_a.

3.6.2 Effect of crystal misalignments

An essential requirement for a Laue lens to work properly is the alignment of the crystals. The misalignment of a crystal can be described using three angles, two of them affect the photon distribution on the detector [92]. They are depicted in Fig. 3.18.

The misalignment angle of a crystal with respect to the lens axis φ_a has a much stronger effect since it causes a first-order variation on the nominal Bragg angle of each ring, whereas φ_b has a second-order effect. A series of LAUENM simulation were performed to quantify these effects. For each crystal, φ_a and φ_b were two random variables with a uniform probability density function over a symmetric interval around zero. It resulted that φ_a affects

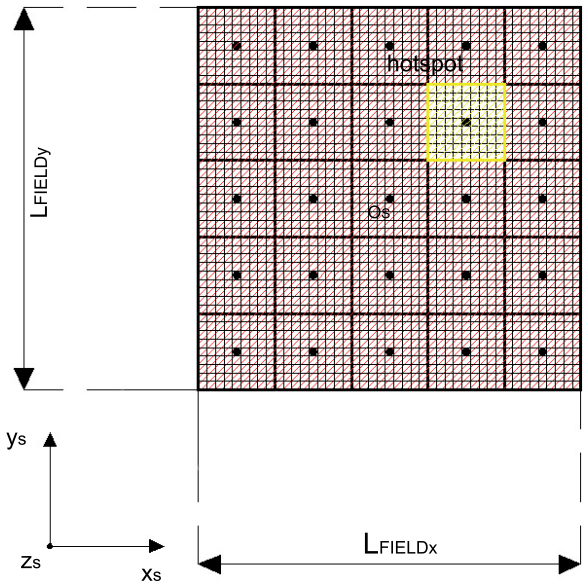

Figure 3.20: Schematic representation of a field of radiation requiring a scan to be imaged. $L_{FIELD_x} = L_{FIELD_y} = 5$ mm.

mainly the size of the spot on the detector, causing a doubling of the FWHM of lens PSF if its maximum value $\varphi_{a_{max}}$ is 30 arcsec. φ_b causes a wider spread of the tails of the photon distribution on the detector and a decrease in the lens efficiency of 7% per degree.

Fig. 3.19 shows the effects of φ_a on the image of the activity distribution inside the region under analysis considered in the previous paragraph. It is evident that, for $\varphi_{a_{max}} =$ 60 arcsec, the image does not correspond any more to the real radioactivity distribution, whereas a value of 30 arcsec does not spoil the imaging properties of the proposed lens. Furthermore, it is worth noting that an accuracy in crystal position within 10-20 arcsec has been reached by the groups involved in the realization of Laue lenses [92, 93], thus an alignment within 30 arcsec is achievable in practice.

3.6.3 Scan of an extended source

As aforementioned, the transversal FOV of the lens is limited by the crystal radial length L_r, while the axial FOV is typically one order of magnitude greater. Since the size of the region to image could be wider than the lens FOV, particularly in the transversal direction, it could be necessary to perform a scan.

Let us consider the 140.5 keV photon source shown in Fig. 3.20. It is a uniform field of radiation with transversal dimensions L_{FIELD_x} and L_{FIELD_y} both equal to 5 mm and axial dimension equal 10 mm. Thus, the source has a cross section wider that the transversal FOV of lens proposed in section 2.3. Inside this volume, there is a $1 \times 1 \times 10$ mm hotspot with an activity concentration 5 times higher than the remainder of the volume. As done

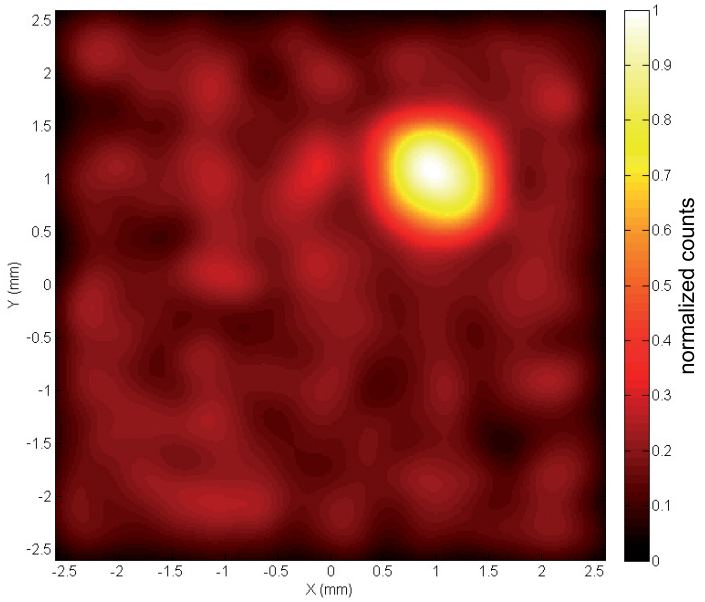

Figure 3.21: Simulated image of the activity distribution inside the a region wider than the lens FOV.

before, we want to simulate the image of this source. Considering the source size and the lens FOV, a 2D scan with 5 steps of 1 mm in each transversal direction (x_S and y_S) is necessary. The scan is envisaged to be performed by moving the bed where the patient lies.

The activity of ^{99m}Tc is 370 MBq, while the uptake is 0.05 and 0.01 for the hotspot and the background region respectively. The depth at which the source lies, the tissue and the detector feature are the same as before. At each step, we consider 14 lens acquiring in parallel the signal from the source for 2.5 min. Thus, the scan would take about 1 hour. The result of the simulation is shown in Fig. 3.21.

In order to quantify the quality of the image, a series of parameters are here introduced. Let N_{hs} and N_b be the mean counts related respectively to the hotspot and to neighbouring background regions with the same area of the hotspot. The ratio

$$\frac{\Delta N}{N_b} = \frac{N_{hs} - N_b}{N_b} \tag{3.30}$$

is called *contrast*. It is one of the most important parameter defining the quality of a diagnostic image [94], it is related to the ability of the human eye to distinguish sharp variations of intensity in a grey scale image (Fig. 3.21 is a false colour image). A more meaningful and frequently used measure in assessing digital images, related to contrast, is

the *contrast-to-noise ratio* (CNR) defined as

$$CNR = \frac{\Delta N}{\sigma_n}, \tag{3.31}$$

where σ_n is the noise in the image [75]. If we assume, as usual, that the counts follow a Poisson Statistics, $\sigma_n = \sqrt{N_b}$.

The *Rose criterion* states that a CNR of at least 5 is needed to be able to distinguish image features at 100% certainty [95]. In the case of concern, CNR is about to 60 and therefore the Rose criterion is fully satisfied. Indeed, the hotspot is perfectly recognisable over the background radiation. Therefore, the proposed Laue lens could be used to effectively image both small and extended source of radiation lying inside the patient's body.

Chapter 4

Laue lenses for radiation therapy

4.1 Motivations

External beam radiotherapy is a technique commonly used for the treatment of tumours. The most widely used particles for radiotherapy are protons, electrons, and X-rays [96]. An important physical quantity used to describe the effects induced by a radiation beam is the absorbed dose, which represents the mean energy imparted to matter per unit mass. The dose distribution inside the patient has a fundamental importance to assess the effectiveness of the treatment. Indeed, the aim of any radiotherapy treatment is to cause as much damage as possible to cancer cells while harming only a few of the healthy ones [97].

Hadron therapy is a technique that can provide precise dose delivery because of the Bragg peak, i.e., the highest ionization density of the hadron beam is near the end of the range [55]. Thus, most of the beam energy is delivered near the stopping point, where the target volume is located. There 63 hadron therapy centres around the world, half of which are in the USA and Japan [98]. These facilities are based on cyclotrons or synchrotrons, the diameter of which spans from a few meters for the smallest cyclotrons to a few tens of meters for the largest synchrotrons [8].

Electron and X-ray beams are more accessible, because they are produced using compact electron linear accelerators (LINACs). They have widespread use in the world, typically with electron energies within the range 4-25 MeV. In particular, electron beams are useful for treating superficial lesions because the maximum of the dose deposition occurs near the surface. The dose then decreases rapidly with depth, sparing underlying tissue [99].

A method to reach deeper tissues consists of using X-ray beams [96]. The depth-dose released by an X-ray beam is described by an initial build-up, where the maximum dose is reached, followed by a long decreasing exponential curve, given by the tissue absorption.

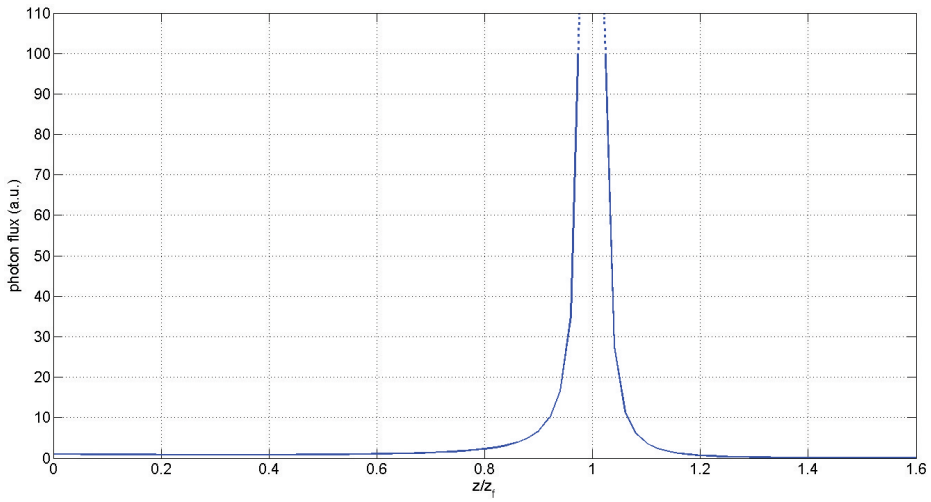

Figure 4.1: Photon flux $\dot{\Phi}$, namely the number of photons per second per unit area, versus penetration depth in a tissue. A monochromatic beam with energy E is ideally focused at a depth z_f. $\dot{\Phi} = \dot{\Phi}_0 \cdot z_f^2/(z_f - z)^2 \exp(-\mu z)$, where $\dot{\Phi}_0$ is the value of the photon flux at $z = 0$ and μ is the total attenuation coefficient at energy E. The term $z_f^2/(z_f - z)^2$ takes into account the variation of the beam cross-section with the penetration depth. The term $\exp(-\mu z)$ takes into account the photon attenuation by the tissue. Under charged-particle equilibrium conditions, the absorbed dose-rate is $\dot{D} = \dot{\Phi} E \mu_{en}/\rho$, where μ_{en} is the absorption coefficient at energy E and ρ is the tissue density [100]. Being $\dot{D}$ proportional to $\dot{\Phi}$, the absorbed dose-rate follows the same behaviour as the flux. The singularity of the flux at the focal depth is due to the perfect focusing and disappears if a real optics is considered.

The X-ray energy is typically in the MeV range to reduce the dose to the skin, because in this case the maximum dose is delivered at a depth of 2-4 cm. Such high-energy photon beams are usually produced through bremsstrahlung, which accelerated electrons undergo passing through a target of a high-Z material, such as tungsten and copper-tungsten alloys. With the aim of reducing the damage to healthy tissues, increasingly sophisticated beam techniques have been developed, e.g. Three-Dimensional Conformal Radiation Therapy (3DCRT), Intensity-Modulated Radiation Therapy (IMRT), Stereotactic Radiation Therapy (SRT), and Tomotherapy [97].

A device capable of focusing a photon beam towards a target volume would pave the way to an innovative radiotherapy methodology. Indeed, for a focused photon beam, the flux along the beam axis increases with the penetration depth, reaching its peak at the focal point and showing a rapid fall-off beyond this point. This effect can be understood by considering the simple case shown in Fig. 4.1, which illustrates the depth-flux curve for a monochromatic photon beam ideally focused at a depth z_f inside a tissue. Under charged-particle equilibrium conditions, the absorbed dose-rate is proportional to the photon flux and therefore, the depth-dose profile shows the same peak of the flux.

Recently, various approaches were proposed to produce a convergent X-ray beam for

radiotherapy application. A first method relies on an equipment applying magnetic and/or electric fields to properly adjust the trajectory of an electron beam from a LINAC [101, 102]. The electrons impinge perpendicularly on the surface of a thin spherical anodic target and generate X-rays with non-isotropic angular-spatial distribution through Bremsstrahlung. The concentration of the photons is greater in the focal direction, which is defined by the geometry of the anode. A properly curved collimator is attached to the back of the anode. X-rays reach the focus passing through the small holes of the collimator. This method requires a LINAC and could be used to focus photons within the energy range 0.4-4 MeV [103]. A further approach to obtain a convergent X-ray beam for radiotherapy application consists of using an X-ray tube and a polycapillary lens as a focusing device [104, 105]. A polycapillary lens exploits multiple total reflections of X-rays inside many hollow glass channels to focus the photon beam towards a target. Since the critical angle for total reflection is inversely proportional to the photon energy, the effectiveness of such approach is limited to photons with energy up to 80 keV [106]. Moreover, the irradiation depth is typically limited to 5 cm. The focal spot size is 100-200 μm wide because of the small radius of the channels. Such a small focal spot implies that even a tumour of 1 cm^3 would require a very time consuming scan of the beam to be uniformly irradiated.

A Laue lens is an optics that would be capable of overcoming these limitations. Fig. 4.2 shows the configuration of a radiotherapy system equipped with a Laue lens. Here an X-ray tube instead of a LINAC is considered as a source of X-rays. The X-ray tube is located at a distance L_S from the lens, which is positioned at the same distance from the focus. The tumour is positioned at the focus, which is at a depth z_f inside the patient's body. A conical metallic applicator joined with the X-ray tube enclosure, similar to that shown in [107], holds both the lens and a collimator. The collimator is positioned just before the patient and stops the photons that transmit through the lens and those that undergo Compton scattering. Furthermore, the lens is equipped with a beam stopper, which stops the direct beam near the optical axis. Hence, ideally only the diffracted beam reaches the patient. A similar approach, based on Bragg-type lens elements, has been proposed in [108]. In this case the energy of the convergent beam is limited to 160 keV, while a Laue lens remains effective to an energy of some hundreds of keV.

The aim of this chapter is to demonstrate the efficiency and versatility of a system for radiation therapy based on a Laue lens. Such a system, based on well-known techniques currently exploited in the field of crystal micromachining, would provide favourable depth-dose curves, comparable with those obtained by high-definition irradiation technologies (IMRT, Tomotherapy or Hadrotherapy) but with significantly less demanding investment in facili-

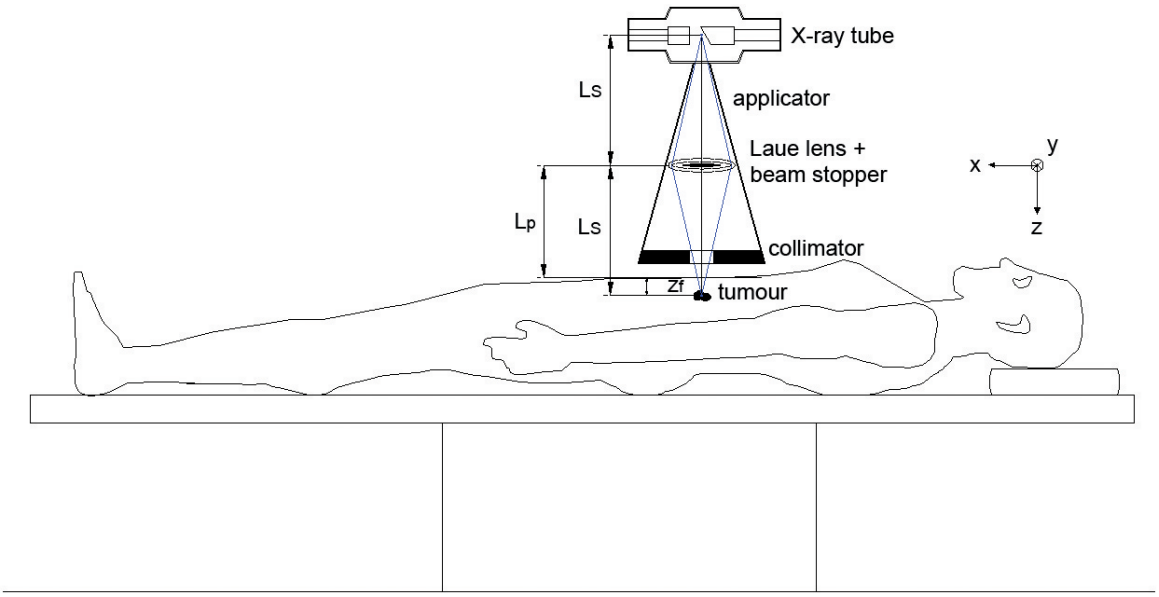

Figure 4.2: Schematic representation of a radiotherapy system exploiting a Laue lens. A fraction of the X-rays emitted by the X-ray tube are focused by the lens towards a target volume that contains the tumour inside the patient's body. The collimator positioned just before the patient together with the beam stopper positioned in the central part of the lens, stop the direct beam and the Compton-scattered photons. Hence, ideally only the diffracted beam reaches the patient.

ties. To show the effectiveness of the proposed system, two series of simulations have been carried out. The first series was performed employing a custom made Monte Carlo software, called LAUETHER and developed in MATLAB language [86]. In the code, the beam emitted by an X-ray tube and the interaction of the photons with the crystals of the lens were taken into account to calculate the phase space of the diffracted photons in a plane at an arbitrary distance from the lens. Starting from the results obtained using LAUETHER, a second series of simulations was carried out considering a voxelized water phantom positioned at a distance L_p from the lens. These latter simulations were carried out using GAMOS [109], a framework based on GEANT4 [110]. The aim of these simulations was to calculate the dose distribution inside the phantom and to determine the dose delivered to a target volume lying inside the phantom itself.

4.2 Lens design principles

The aim of using a Laue lens is to obtain a nearly monochromatic X-ray beam, focused towards a small focal spot. The features and the design method for a Laue lens employed to diffract a monochromatic and divergent beam for diagnostic applications was widely treated in the previous chapter. In the context of this chapter, the source is an X-ray tube, which

emits a polychromatic and divergent beam. Such kind of X-ray source was taken into account for two reasons: first, X-ray tubes are widely available and they emit high fluxes; second, a Laue lens can be designed to focus a narrow portion of the source spectrum. Therefore, the design here proposed is an evolution of that described before.

In the case of a focused X-ray beam, the dose distribution inside the patient's body depends on the properties of the employed optics. For a Laue lens, the nominal energy of the diffracted beam E_0 and the focal distance L_S can be chosen independently. Once they are set, the geometry of the lens can be determined. The crystals that compose the lens are envisaged to be disposed as N concentric rings. Each ring is formed by identical crystals that are initially assumed to be perfectly positioned and aligned. The material, structure, size, and lattice orientation of the crystals have to be set to satisfy some requirements that will be specified in the following.

The materials commonly considered for the fabrication of the optical elements of a Laue lens are monocrystals of Cu, GaAs, Si, and Ge. They are widely available and their growth technology is well-known [53]. The crystal structure of these materials is cubic and they have a high electronic density that ensures a high diffraction efficiency [111].

For each ring, a geometric condition has to be satisfied to permit the focusing of the X-ray beam. Let us consider the line passing through the source and the centre of a crystal. The angle between such line and the lens axis has to be equal to the Bragg angle for the crystal at nominal energy E_0. For a crystal with a cubic lattice and under small-angle approximation, this condition can be expressed as

$$\frac{r}{L_S} = \theta_{B_0} = \frac{h_p c}{2aE_0}\sqrt{h^2 + k^2 + l^2}, \tag{4.1}$$

where r is the radius of the ring to which the crystal belongs, θ_{B_0} the nominal Bragg angle, h_p the Planck's constant, c the speed of light in vacuum, a the lattice constant of the crystal, and h, k, l the Miller indices of the diffracting planes. Equation (4.1) represents Bragg's (see equation 1.4) law and permits to determine the ring radius once the material and the lattice orientation of the crystals have been set. Crystals that exploit lattice orientations with large Miller indices and/or crystals with small lattice constant fill the outermost rings. Fig. 4.3 schematically shows the diffraction occurring in a generic crystal of the lens. A symmetric Laue (transmission) geometry is considered. The photons traverse the crystal thickness T_0 and are diffracted at the portion of the crystal where Bragg's law is satisfied. The ring radius is $\overline{O_L C}$. The radial size of the crystal L_r is highlighted in the figure. The tangential size L_t is the size of the crystal in the direction perpendicular to the plane of the

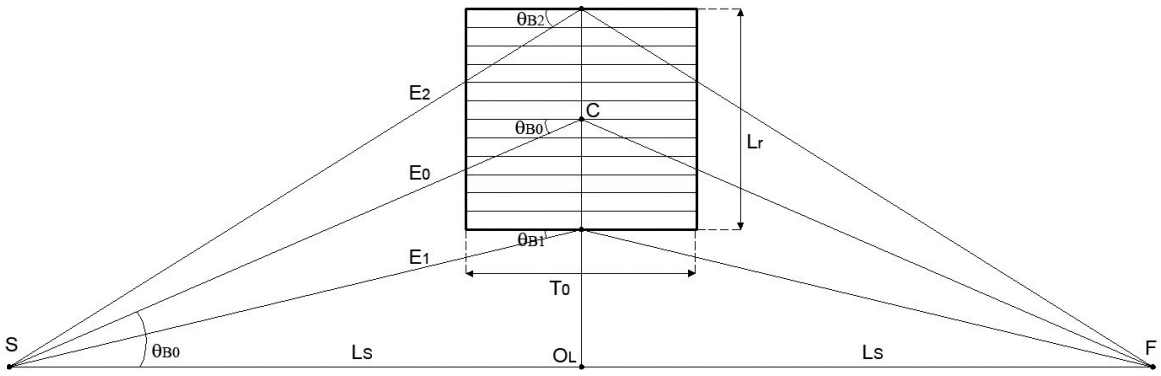

Figure 4.3: Sketch (not to scale) of a generic crystal in the lens. T_0 is the crystal thickness traversed by the beam and L_r is the radial size of the crystal. $\overline{O_L C}$ is the ring radius. The X-ray source S is at a distance L_S from the center of the lens O_L, the lens focus F is at the same distance but in the in the opposite direction. For a given crystallographic orientation, photons with different energy E_j are diffracted at a different Bragg angle θ_{B_j}.

figure. Since the X-ray tube emits photons with different energy, they are diffracted at a different Bragg angle and diffraction occurs in a different position in the crystal.

The crystals may be arranged in each ring according to a polygonal arrangement that best approximates the ring. In this way, the outermost rings contain a higher number of crystals. In general, different rings can be composed of optical elements made of diverse materials and exploiting different crystallographic orientations to satisfy equation (4.1). This is the same approach adopted in the previous chapter. The lens has to concentrate as much incident photons as possible toward the focus. Namely, the crystals should have a high integrated reflectivity. For this reason, crystals with mosaic structure or with self-standing curved diffracting planes (CDP) are the best choice for the fabrication of a Laue lens [81].

For the selection of size and type (mosaic or CDP) of the crystals that compose the lens, some figures of merit that strongly depend on these quantities have to be introduced. The efficiency of the lens ε is defined as the ratio of the diffracted photons to the photons emitted by the X-ray tube within the solid angle subtended by the Laue lens. The diffraction efficiency of the lens ε_D is defined as the ratio of the diffracted photons to the photons impinging on the surface of the crystals. These parameters quantify the diffraction process occurring in the whole lens once the energy band of the impinging beam has been specified. They are linked to one another through the equation

$$\varepsilon = \frac{A_L}{A_{oi}} \varepsilon_D, \tag{4.2}$$

where A_L is the total geometric area of the crystals and A_{oi} is the area of the intersection of the solid angle subtended at the source by the lens with the midplane of the lens itself.

A_L is

$$A_L = \sum_{j=1}^{N} n_j L_{r_j} L_{t_j}, \tag{4.3}$$

n_j being the number of crystals in the jth ring. A_{oi} is just

$$A_{oi} = \pi r_{ext}^2, \tag{4.4}$$

r_{ext} being the external radius of the lens.

Three important physical quantities for the therapeutic use of convergent X-ray beams are the size of the focal spot, the energy passband of the diffracted beam, and the number of diffracted photons per mAs of the X-ray tube N_D. The mAs of the tube, namely the product of the anodic current (mA) and the time of irradiation (s), represents the electron charge (mC) impinging on the anodic surface. mAs is used because, together with the peak voltage, it is a parameter that is commonly used to describe the setting of an X-ray tube.

The bandwidth B of the diffracted beam around the nominal energy E_0 can be derived as follows. Bragg's law, under small-angle approximation, gives an inverse proportionality between diffraction angle and photon energy. Differentiating this relationship, it follows that a relative increase in diffraction angle is equal to a relative decrease in the photon energy, namely

$$\frac{\Delta E}{E_0} = -\frac{\Delta\theta_B}{\theta_{B_0}}. \tag{4.5}$$

From Fig. 4.3, it can be seen that, for a crystal in a given ring, the maximum variation of the diffraction angle $\Delta\theta_B$ from the nominal Bragg angle θ_{B_0} is

$$\Delta\theta_B = \pm\frac{1}{2}\left(\frac{L_r}{L_S} + \Omega\right), \tag{4.6}$$

where L_r is the radial size of the crystals and Ω the angular acceptance of the crystals due to mosaicity or to the curvature of the diffracting planes. A negative value of $\Delta\theta_B$ corresponds to an increase in the diffracted photon energy $\Delta E_+ = E_+ - E_0 = E_0/\theta_{B_0}(L_r/L_S + \Omega)/2$, while a positive value of $\Delta\theta_B$ corresponds to a decrease in the diffracted photon energy $\Delta E_- = E_- - E_0 = -E_0/\theta_{B_0}(L_r/L_S + \Omega)/2$. Therefore, the bandwidth ΔE for the considered ring is

$$\Delta E = \Delta E_+ - \Delta E_- = \frac{E_0}{\theta_{B_0}}\left(\frac{L_r}{L_S} + \Omega\right). \tag{4.7}$$

The lens bandwidth B is the maximum value among the ΔE of the rings. A lens composed of crystals having a large radial size would have a wide bandwidth. However, for a fixed size of the lens, large values of L_r could imply a decrease in the number of rings. As a

consequence, the usage of all the desired lattice orientations could be prevented. Thus, a trade-off has to be chosen. It is worth noting that the aforementioned band is centred around E_0, but also the bands centred around the low- and high-order harmonics from E_0 may be present in the diffracted beam spectrum depending on the source spectrum and the considered lattice orientations. However, in the practical cases, their intensity is negligible compared to that of the nominal band.

The distribution of the diffracted photons around the focal point F results from the combination of focusing and defocusing effects. The main focusing effect is due to lattice orientations chosen so as to satisfy equation (4.1). The main defocusing effect arises because the crystals cannot be sagittally bent to a radius of curvature equal to the radius of their ring [83]. If the crystals composing the lens are flat, these are the only effects that have to be taken into account. On the contrary, CDP crystals provide a further focusing/defocusing effect that depends on the radius of curvature of the diffracting planes (see Appendix B). For a CDP crystal, the width of the diffraction profile at the focal distance is equal to $2|T_0\theta_{B_0} - \Omega L_S|$, provided that a point source is considered. For a flat crystal, the width of the diffraction profile is $2T_0\theta_{B_0}$. Therefore, if the radius of curvature of the diffracting planes $R_C = T_0/\Omega$ is larger than $L_S/(2\theta_{B_0})$, the width of the diffraction profile is smaller than for a flat crystal, giving rise to a focusing effect. On the contrary, if $R_C < L_S/(2\theta_{B_0})$, a defocusing effect arises. For very small radius of curvatures, this defocusing can be even larger than the defocusing due to the lack of sagittal curvature. If the lens is composed of mosaic crystals instead of CDP crystals, a further defocusing effect arises due to the spread of the diffracting planes [15]. In practical cases, with both types of crystal, the dominant effect is the defocusing due to the lack of sagittal curvature. Under this condition, the full size of the spot, namely the diameter s of a circle enclosing all the photons, is simply

$$s = 2L_{t_{max}}. \tag{4.8}$$

Crystals with a large tangential size would lead to a large focal spot, lowering the precision in dose delivery. On the other hand, a sub-mm spot would imply the necessity to use several scanning steps to irradiate uniformly even a small tumour mass, causing an increase in the total irradiation time. Hence, we considered L_t equal to 3 mm at most, which is a good trade-off between precision in dose deposition and irradiation time.

The lens efficiency ε can be accurately evaluated only through a simulation of the system because the distribution of the diffracted photons cannot be analytically described in closed

form. However, ε_D and therefore ε, can be roughly estimated within ±30% as follows.

$$\varepsilon_D = \frac{\sum_{j=1}^{N} n_j \overline{R_{peak_j}} \Omega_j}{\sum_{j=1}^{N} n_j L_{r_j}} L_S \frac{B}{B_S} f_c, \tag{4.9}$$

where $\overline{R_{peak_j}}$ is the mean peak reflectivity of the crystals composing the j-th ring over the lens bandwidth, N the number of the rings, B_S the bandwidth of the source spectrum, and f_c a correction factor that takes into account the variation of the crystal reflectivity over the lens bandwidth and that can be assumed to be 0.5 in practical cases.

Once ε is known, the number of diffracted photons per mAs of the X-ray tube N_D can be calculated through the following equation

$$N_D = \varepsilon \left(\frac{L_{ref}}{L_S} \right)^2 A_{oi} \int_{E_L}^{E_H} \frac{d\Phi(E)}{dE} dE, \tag{4.10}$$

where E_L and E_H are the lowest and the highest energies of the photons emitted by the source, and $d\Phi(E)/dE$ is the differential photon fluence per mAs, at the reference distance L_{ref}.

The photons emitted by the source that are not focused by lens, namely those that do not impinge on the lens and those that impinge but do not undergo diffraction, have to be stopped by a proper collimation system to avoid harming the patient. We envisage a collimation system composed of a beam stopper positioned just before the central part of the lens and a collimator positioned just before the patient. Given the source spectrum, 5-mm-thick lead absorbers would suppress the non-focused beam reaching the patient by a factor of about 0.001 with respect to the focused beam. As shown in Fig. 4.2, a conical metallic applicator joined with the X-ray tube enclosure holds both the beam stopper and the collimator.

4.3 LAUETHER simulations

The LAUETHER software was used to determine the features of the crystals that provide the desired lens performance. In the next subsections, some details about this custom made Monte Carlo code and the design of a specific Laue lens are presented.

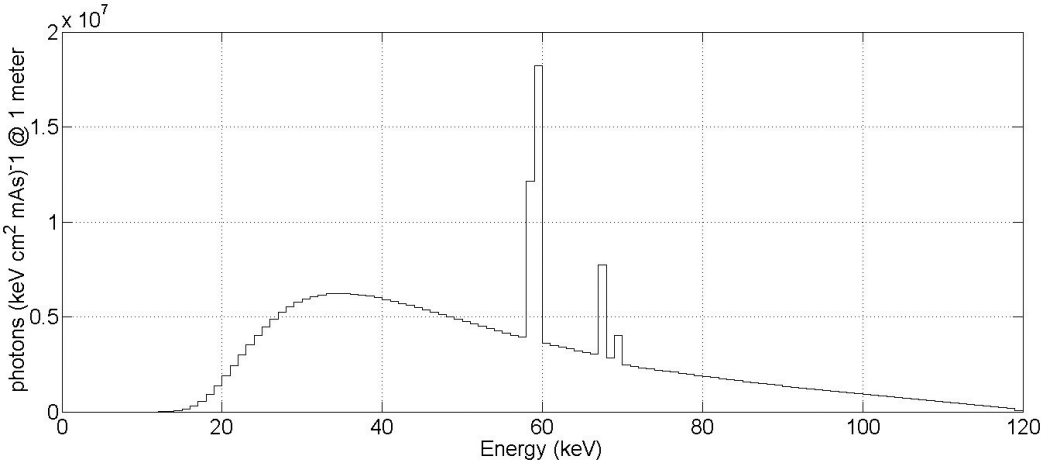

Figure 4.4: Spectrum of the X-ray tube considered in the simulations. The tube had a tungsten anode with an inherent filtration of 0.8 mm of Be. A filtration of 2 mm of Al was added and the peak voltage was set to 120 kV. The spectrum was calculated using the SpekCalc program. The bin width is 1 keV.

4.3.1 The LAUETHER code

The LAUETHER computer program was developed in MATLAB language and is composed of an ensemble of scripts functionally grouped in three main modules. The pre-processing module manages the lens geometry and the photon generation. The processing module handles the interaction of the photons with the crystals and calculates the phase space of the diffracted beam. Finally, the post-processing module computes the lens figures of merit and generates several plots of interest. LAUETHER can be considered a generalized version of the LAUENM code described in chapter 3 and Appendix B. It can manage sources with arbitrary spectral and spatial distributions. However, since a small-focus ($\sim$ 500 μm) X-ray tube is envisaged to be used to preserve the focusing capability of the lens, a point-like source is initially assumed in the simulations for the sake of simplicity. Furthermore, photons are randomly generated inside the solid angle subtended at the source by the lens neglecting the *Heel effect*, namely the variation of the intensity of X-rays depending on the direction of emission. Indeed, the aperture of the solid angle cone is typically $< 5°$. The photon energy is a random variable with a probability density function defined according to the source spectrum. In particular, the X-ray tube considered in our simulations had a tungsten anode with an inherent filtration of 0.8 mm of Be. A filtration of 2 mm of Al was added and the peak voltage was set to 120 kV. The spectrum of such a tube was calculated through the SpekCalc software [112] and it is shown in Fig. 4.4.

The processing module considers X-ray diffraction in absorbing crystals. The algorithm is similar to that of the corresponding module of the LAUENM code (see Appendix B). The

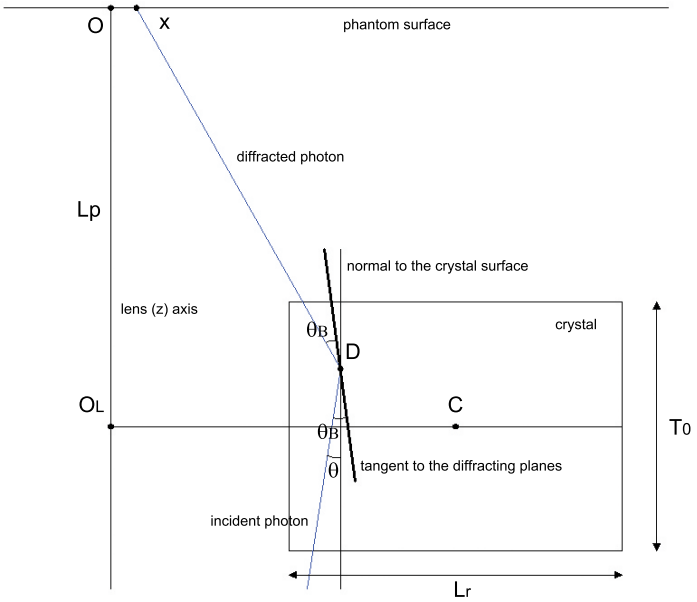

Figure 4.5: Sketch of the diffraction process. A photon with energy E impinges on the crystal surface with an angle θ with respect to a line parallel to the lens axis. Diffraction occurs in the region of the crystal where the Bragg condition is met (point D).

main difference is that here the variation of the nominal Bragg angle θ_{B_0} of the crystals for photons of energy $E \neq E_0$ is taken into account through equation (4.5). The Compton-scattered photons are not tracked by the program because their contribution to the delivered dose is negligible with respect to that due to the diffracted photons. Fig. 4.5 depicts the diffraction process occurring in a generic crystal in the lens. The orientation of the diffracting planes varies throughout the traversed thickness due to the mosaicity/curvature of the crystal. A photon with energy E impinging on the crystal surface with an angle θ with respect to a line parallel to the lens axis is diffracted at the region of the crystal where the Bragg condition is met. The probability that this process occurs is given by the crystal reflectivity at energy E. The arrival point of the diffracted photons on the phantom surface and the related direction cosines are calculated.

4.3.2 Proposal of a Laue lens for radiotherapy

As a practical case, we worked out the design of a lens to be used in combination with the X-ray tube described in the previous subsection. In particular, the lens provides a convergent beam with a nominal energy $E_0 = 80$ keV if the source-to-lens distance L_S is set to 50 cm. The lens is composed of CDP Si crystals because they provide the highest diffraction efficiency at this photon energy [69]. Moreover, Si is a widely available material and its growth technology is well-known since it is usually used in microelectronics. The crystals are considered to be square tiles 2×2 mm in size. Table 4.1 summarizes the

Table 4.1: Rings of the lens.

ring	crystals	ring radius	Bragg angle	reflection	harmonics
1	31 CDP Si	12.4 mm	1.42°	80 keV (111)	-
2	53 CDP Si	20.2 mm	2.31°	80 keV (220)	-
3	63 CDP Si	23.7 mm	2.71°	80 keV (311)	-
4	77 CDP Si	28.6 mm	3.27°	80 keV (400)	-

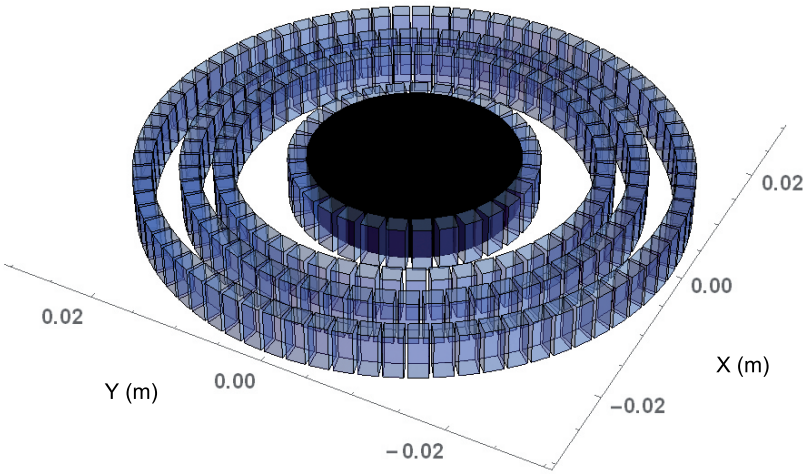

Figure 4.6: Perspective view of the Laue lens designed to focus an 80 keV beam at a distance of 50 cm. The rings of the lens are composed of CDP Si crystals exploiting different lattice orientations. The black disk represents the beam stopper that stops the photons of the direct beam near the lens axis. The photons of the direct beam passing through the voids between the rings are stopped by the collimator positioned before the patient.

physical quantities featuring the rings of the lens, such as number of crystals, radius, lattice orientation, etc.

For each crystal, the traversed thickness T_0 is set to 5 mm and the radius of curvature of the diffracting planes R_C is set to 34.4 m. Therefore, the angular acceptance of the crystals is $\Omega = 30$ arcsec. The designed lens is depicted in Fig. 4.6. The black disk represents the beam stopper, which is positioned just before the central part of the lens. It stops the direct beam, which otherwise would reach the phantom surface near the lens axis. The photons of the direct beam passing through the voids between the rings of the lens are stopped by the collimator positioned before the patient's skin.

A simulation of the proposed system was carried out to calculate the lens performance. Fig. 4.7 shows the spectrum of the diffracted beam as it comes out from the simulation. The spectrum is approximately symmetric around the nominal energy with a bandwidth of 13 keV, in agreement with the value calculated through equation (4.7). The slightly lower intensity for energies higher than 80 keV with respect to the symmetric counterpart is due to the decrease of intensity in the spectrum of the source. Since the maximum energy emitted

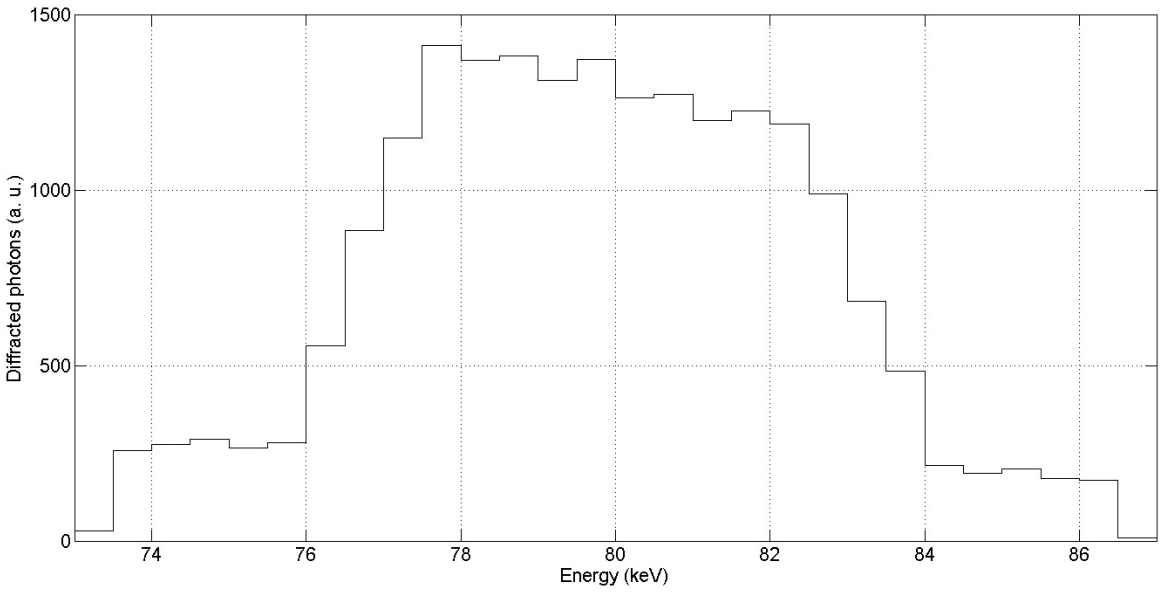

Figure 4.7: Spectrum of the diffracted beam. The bin width is 0.5 keV.

by the source is 120 keV, there are no high-order harmonics.

The lens has an efficiency ε equal to 3.2×10^{-3} considering its passband (73.5-86.5 keV) and equal to 6×10^{-5} considering the whole energy band of the source (12-120 keV). N_D is about 1×10^7 photons/mC. These values include the contribution of the photon absorption due to air and to the lens support. In particular, we considered a Si support with a thickness of 2 mm.

Fig. 4.8 shows the distribution of the diffracted photons at a distance z from the lens equal to L_p and L_S respectively. As can be seen from Fig. 4.8.a, the diffracted beam has an hollow cross section before the focus. This is due to the lens geometry, which does not present crystals in the innermost part. Fig. 4.8.b shows the focal spot. In this case, the curvature of the diffracting planes leads to a focusing effect. The number of photons in the focal plane enclosed by a circle increases linearly with the diameter of the circle. In particular, the spot core including 50% of the photons is about 2 mm wide. The full spot size is 4 mm, in agreement with the value calculated through equation (4.9), $L_{t_{max}}$ being 2 mm.

So far a perfect crystal alignment was supposed, hence the diffracted beam has a perfect rotational symmetry. Actually, such condition is not practically achievable. Therefore, as done for the diagnostic case, we investigated the effect of crystal misalignment on the lens performance. There are three possible misalignment angles; two of them exert a non-negligible influence on the diffracted beam [92]. These angles are represented in Fig. 4.9. The angle φ_a has a much stronger effect since it causes a first-order variation on the nominal

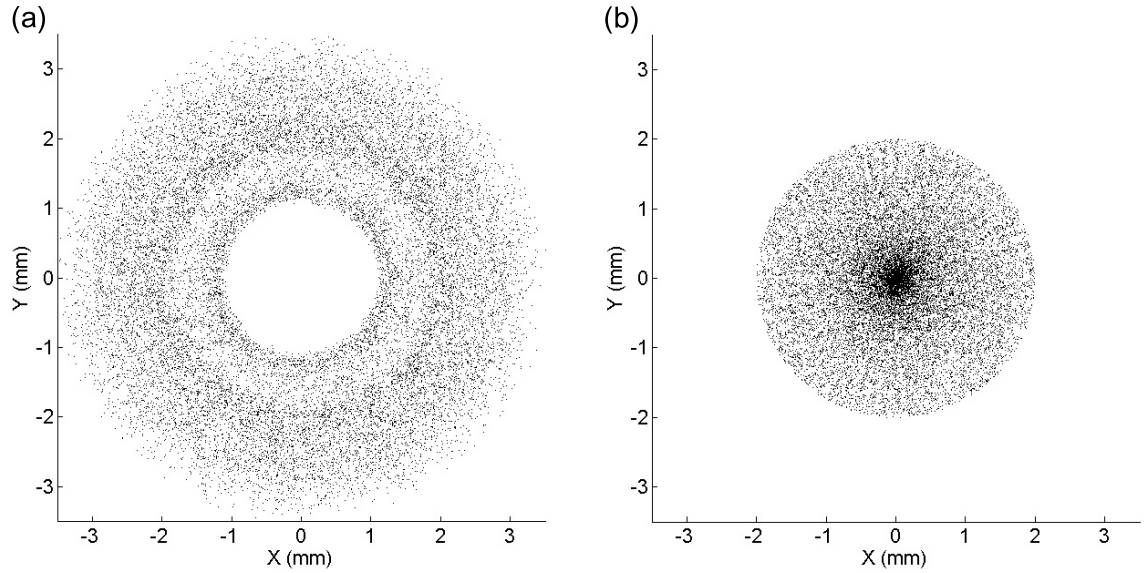

Figure 4.8: Scatter plots showing the transversal coordinates (x, y) of the diffracted photons at different axial distances (z) from the lens. (a) $z = L_p = 45.25$ cm, (b) $z = L_S = 50$ cm.

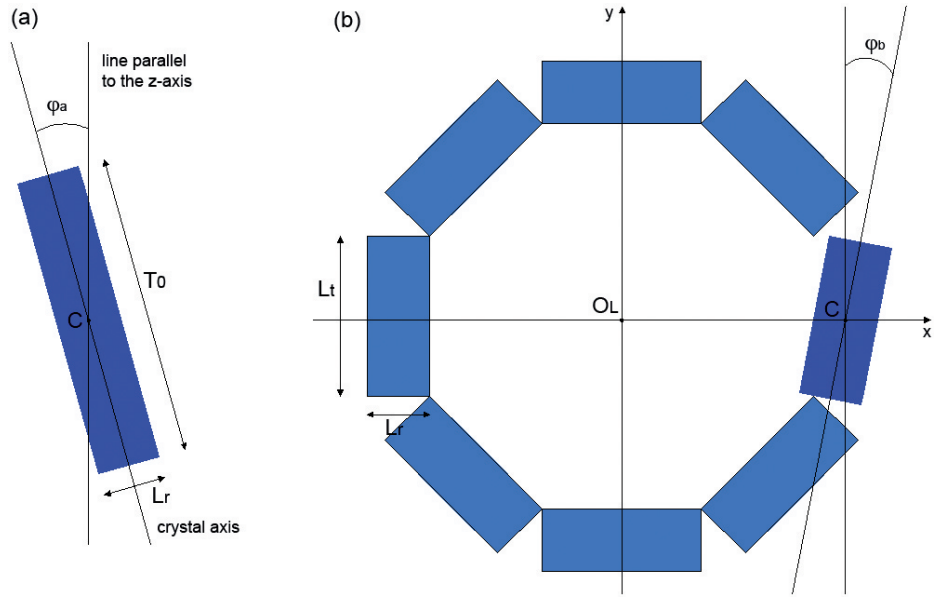

Figure 4.9: Misalignment angles of a crystal in a given ring. (a) φ_a, (b) φ_b.

Table 4.2: Lens performance as a fucntion of misalignment angle φ_a.

φ_a range (arcmin)	Bandwidth (keV)	N_D $(photons/mAs)$	spot size (mm)
0	13.0	9.78×10^6	4.00
± 1	17.0	9.72×10^6	4.10
± 2	20.5	9.70×10^6	4.20
± 3	23.0	9.77×10^6	4.30
± 4	26.0	9.54×10^6	4.40
± 5	30.0	9.65×10^6	4.60

Table 4.3: Lens performance as a fucntion of misalignment angle φ_b.

φ_b range (°)	Bandwidth (keV)	N_D $(photons/mAs)$	spot size (mm)
0	13.0	9.78×10^6	4.00
± 1	13.0	8.94×10^6	4.80
± 2	13.0	8.12×10^6	5.60
± 3	13.0	7.28×10^6	6.40
± 4	13.0	6.35×10^6	7.20
± 5	13.0	5.89×10^6	7.20

Bragg angle of each ring, whereas φ_b has a second-order effect [73]. We performed a series of LAUETHER simulations to quantify the effect of the misalignment angles. For each crystal, φ_a and φ_b were two random variables with a uniform probability distribution over a symmetric range around zero. It resulted that both φ_a and φ_b affect the shape of the focal spot and cause an increase in its size. Furthermore, the lens bandwidth increases almost linearly with φ_a and the lens efficiency inversely depends on φ_b. Tables 4.2 and 4.3 summarize the simulation results. As we show in the next paragraph, φ_a and φ_b have a small effect on the dose distribution inside a phantom provided that their maximum value is smaller than 1 arcmin and 1° respectively. These values are well above the state of the art of alignment techniques currently adopted for the fabrication of a Laue lens. Indeed, a positioning accuracy within 10-20 arcsec has been reached by the groups involved in the assembly of Laue lenses devoted to astrophysics [92, 93].

Other issues that may degrade the lens performance are the non-uniform bending of the crystals and the sub-surface damage and strain due to the fabrication process. Indeed, they cause a decrease in the diffraction efficiency of the crystals [69].

4.4 GAMOS simulations

To assess the effectiveness of the convergent beam diffracted by the proposed lens in the treatment of tumours, the dose distribution inside a voxelized water phantom was calculated.

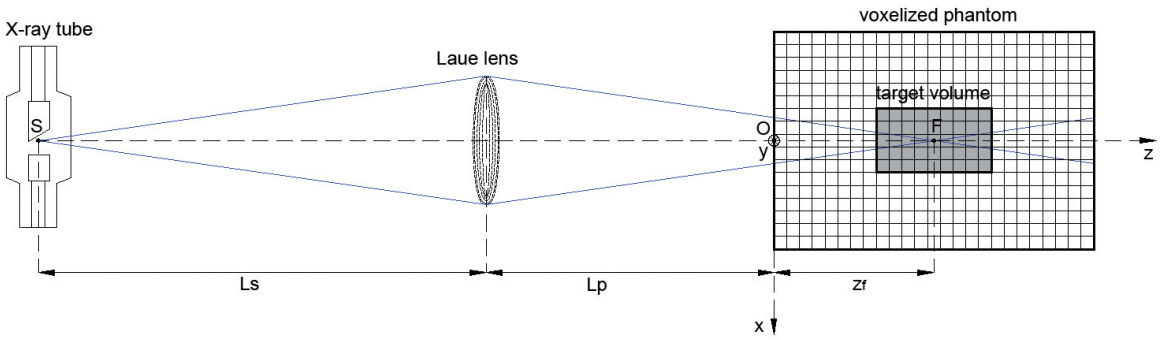

Figure 4.10: Geometry of the system considered in the simulations. A voxelized water phantom is at a distance L_p from the lens. The target volume is a portion of the phantom lying at a depth z_f, where $L_p + z_f = L_S$. The adopted system of coordinate $Oxyz$ is highlighted.

GAMOS, a GEANT4 wrapper, was used to accomplish this task. GEANT4 is a general purpose Monte Carlo code for particle tracking inside matter [110, 113]. GAMOS was chosen because it allows the user to define the geometry of the system, the particle generator, the physics list, and the required output information in a single input script. Then, the core of the program instantiates the GEANT4 classes required to perform the simulation. The coordinate system adopted in the simulation is shown in Fig. 4.10. The origin was set at the intersection of the phantom surface with the lens axis (z-axis). The focus of the lens was at a depth of 4.75 cm along the z-axis. The phantom was described by exploiting the *GmSimplePhantomGeometry* command. Its size was 1.95×1.95×9.50 cm, which was divided into 288990 cubic voxels having a volume of 0.125 mm^3 each. An input text file, containing the phase space of the diffracted beam at the phantom surface, was produced according to the format required by the *GmGeneratorFromTextFile* command. this file was used in the input script as a particle generator. About 1×10^7 primary photons were considered to obtain good statistical significance of the calculated dose per voxel. The PENELOPE [114, 115] physics lists for photons, electrons, and positrons were used in our simulation. The output of the simulation was a *3ddose* file, containing the dose to each voxel of the phantom.

Fig. 4.11 shows the percent depth-dose (PDD) profile calculated along the central axis. This curve shows a pronounced peak at the depth of the focus. The Full Width at Half Maximum (FWHM) of the curve is about 1.2 cm and in the following it will be referred to as *depth of field*. To avoid harming radiosensitive tissues beyond the tumour, it is important that the dose drops to zero as rapidly as possible. Fig. 4.11 shows a rather rapid fall-off of the dose beyond the focus. It is worth noting that for a hadron therapy beam the dose drops at a faster rate. The dose along the lens axis is close to zero in the superficial voxels

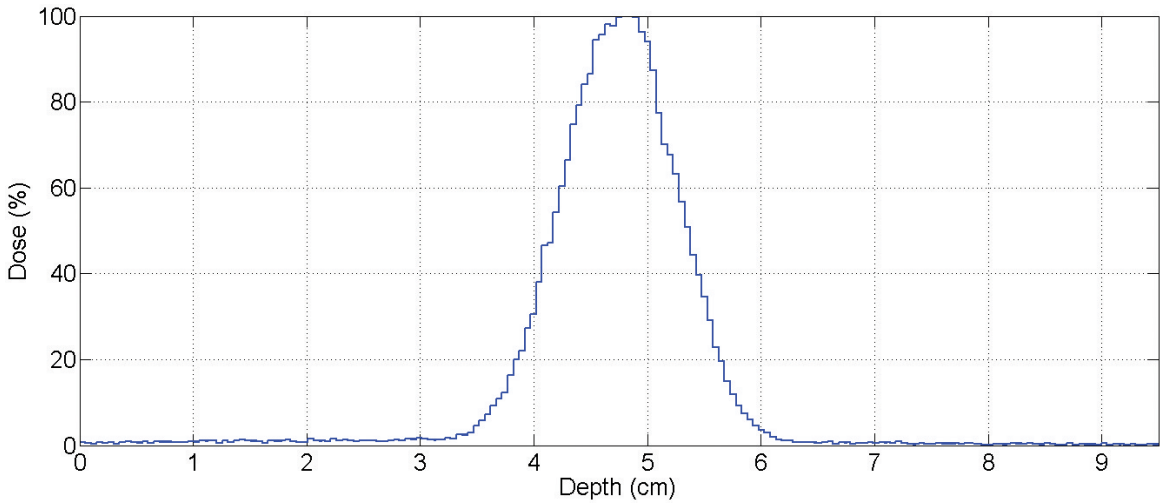

Figure 4.11: Percent Depth-Dose curve along the lens axis (z-axis).

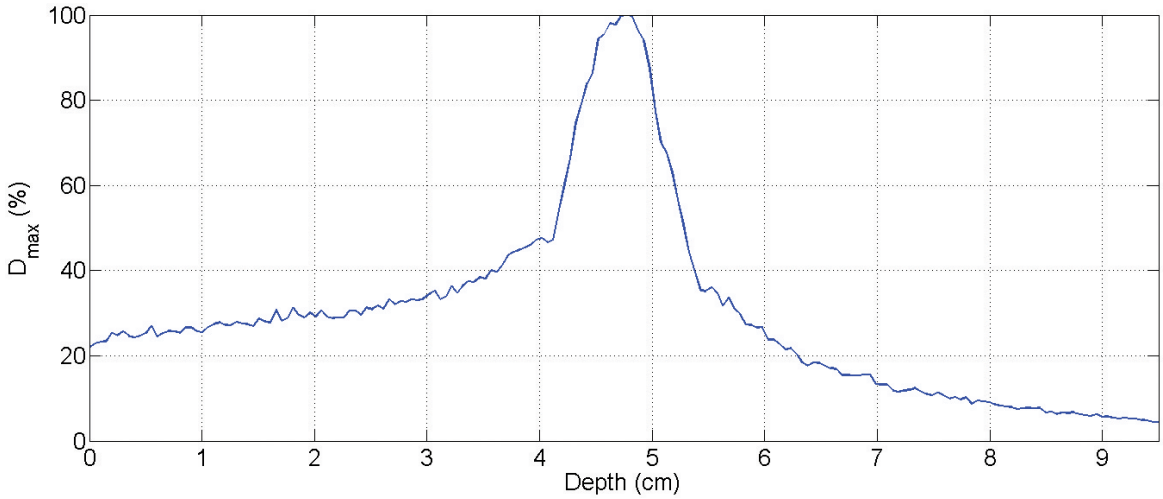

Figure 4.12: Ratio of the maximum dose in each slice to the absolute maximum dose given to the voxels of the phantom.

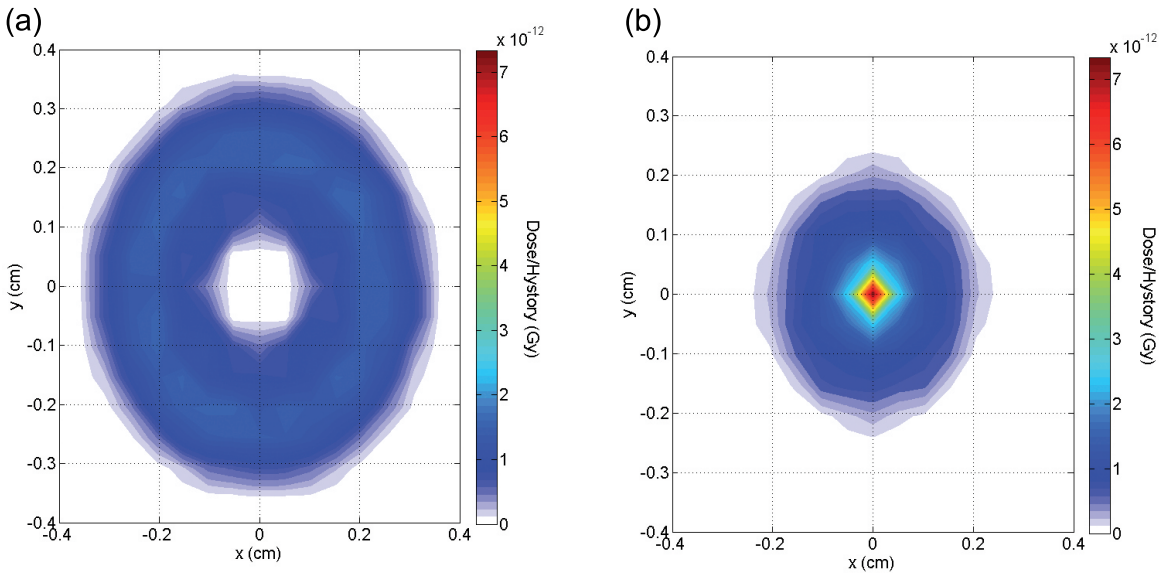

Figure 4.13: Dose distribution in two phantom slices lying at a different depth. (a) Dose distribution in the first (superficial) slice. (b) Dose distribution in the focal slice.

because of the hollow transverse section of the diffracted beam. Fig. 4.12 shows ratio of the maximum dose in each slice to the absolute maximum dose given to the voxels of the phantom. As can be seen, the maximum dose in the superficial voxels is about 22% of the absolute maximum dose.

Fig. 4.13 shows the dose distribution in the superficial slice and in the focal slice, whereas Fig. 4.14 and Fig. 4.15 show the dose distribution in the plane $y = 0$. It is evident how the dose peak is well-localized at the focal depth, while the surrounding regions receive a lower dose. This behaviour makes the proposed system actually suitable for radiotherapy applications.

To show the effectiveness of the proposed system, the time required to give a dose of 2 Gy [1] to a target, localized at a depth of 4.75 cm and whose $x \times y \times z$ size is 0.2×0.2×1.2 cm, is calculated. From the simulation, it turns out that a dose of 9.78×10^{-10} Gy per event is given to the target. Since the lens provides about 1×10^7 photons per mAs, the irradiation time would be about 10 s with an anodic current of 20 mA.

The effect of the crystal misalignment has been evaluated assuming a range for φ_a and φ_b of ±1 arcmin and ±1° respectively. The results of these simulations are summarized in Table 4.4. The performance decrease does not spoil significantly the effectiveness of the method.

[1] A dose of 2 Gy is commonly considered as a reference dose in radiotherapy. Indeed, the surviving fraction of the cells irradiated with an X-ray dose of 2 Gy is an indicator of the radiosensitivity of that tissue. Moreover, the total dose prescribed to treat a given tumour is generally fractionated, each irradiation delivering a dose of 2 Gy [97].

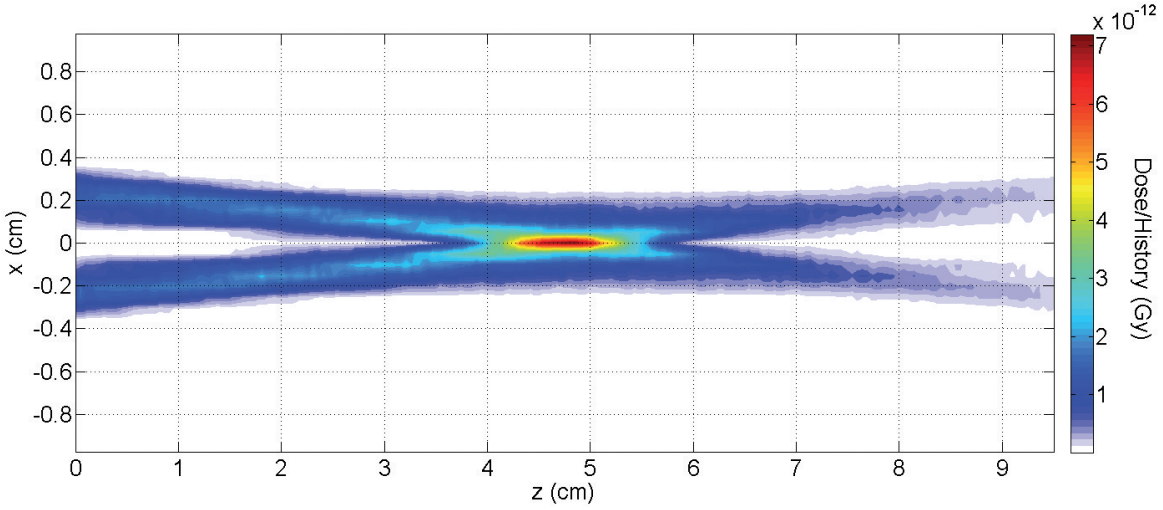

Figure 4.14: Dose distribution in the plane $y = 0$.

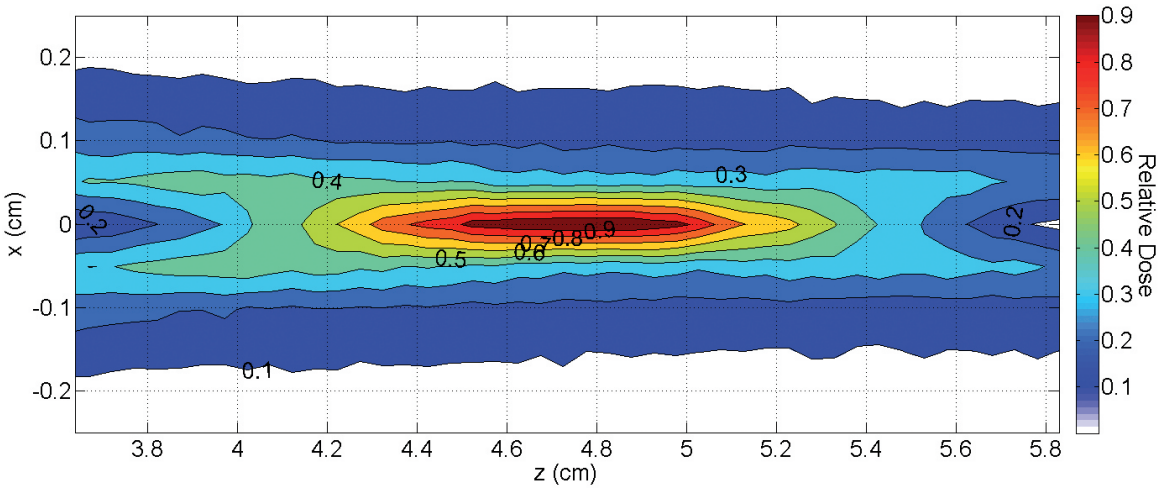

Figure 4.15: Dose distribution in the plane $y = 0$ around the lens focus. Isodose curves are shown.

Table 4.4: Effect of the misaligment angles on the dose distribution inside the phantom.

misalignment range	depth of field	superficial D_{max}	target dose (Gy/event)
$\varphi_a = \varphi_b = 0$	1.19 cm	22.0%	9.78×10^{-10}
φ_a: ± 1 arcmin	1.56 cm	30.6%	9.70×10^{-10}
φ_b: $\pm 1°$	1.23 cm	23.0%	9.60×10^{-10}

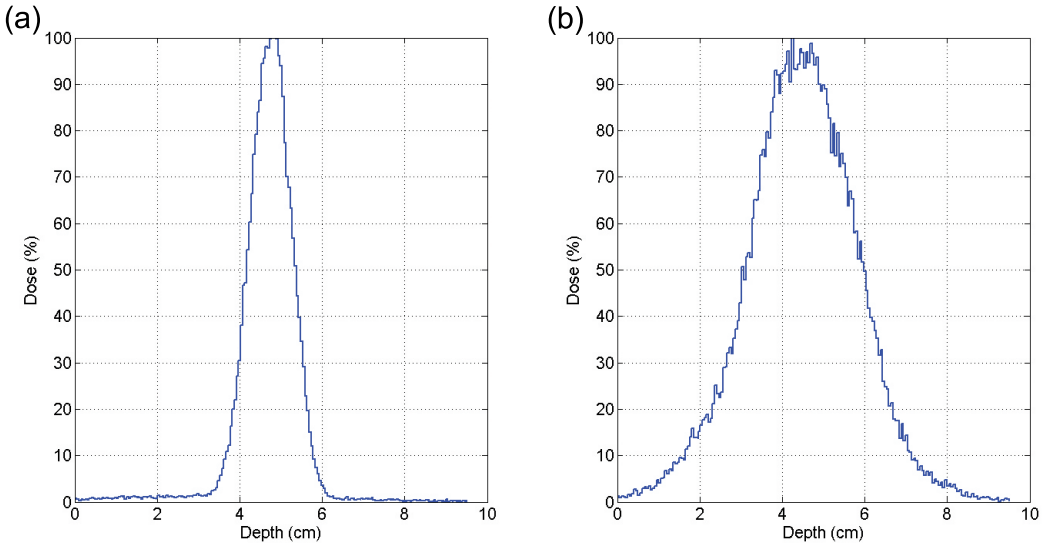

Figure 4.16: Percent depth-dose curve along the lens axis considering two different source shapes. (a) point-like source, (b) circular source with a diameter of 1.2 mm.

A further issue that could degrade the lens performance is due to the finite size of the X-ray tube focus. A simulation was performed with a 1.2 mm source to assess its effect on the dose distribution inside the phantom. Fig. 4.16, compares the PDD curve obtained in this case with the PDD obtained considering a point-like source. The depth of field increases from 1.2 cm to 2.9 cm. The spread of focal spot increases also in traversal direction, doubling its size. Furthermore, the maximum dose in the superficial voxels becomes about 45% of the absolute maximum dose. Thus, the overall lens performance worsens if the X-ray tube focus is larger than 1 mm. Through a series of simulations with sources of different size, we found that the lens performance are virtually unchanged if the focus of the X-ray tube is of the order of 500 μm.

So far, we have considered a target localized at a depth z_f of 4.75 cm within the phantom. However, using a given lens, it is possible to irradiate a target volume positioned at a depth $z_f + \Delta z_f$ in two different ways. In the first way, the source and the lens have to be moved towards the phantom both by Δz_f so that the source-to-lens distance remains equal to the focal length L_S. In this case, the spectrum of the diffracted beam does not vary significantly. In the second way, the source has to be moved backward by Δz_f, so the focal length varies by the same quantity $\Delta L_S = \Delta z_f$. In this case, by differentiating equation (4.1), it follows that

$$\frac{\Delta E_0}{E_0} = \frac{\Delta L_S}{L_S}. \tag{4.11}$$

In other words, the nominal energy of the diffracted beam increases proportionally to the source-to-lens distance. As a consequence, the lens efficiency suffers a slight decrease.

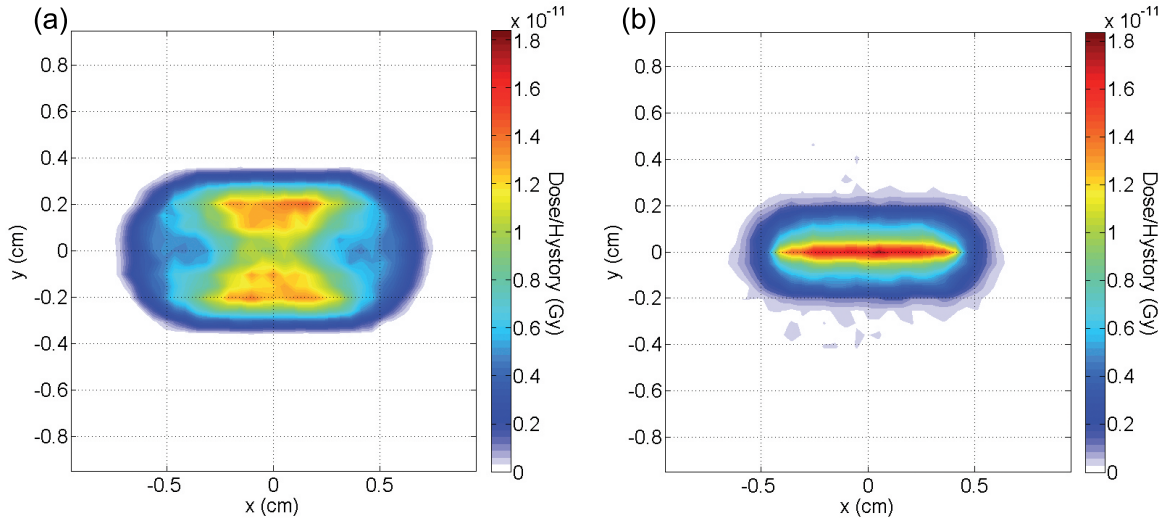

Figure 4.17: Dose distribution in two phantom slices lying at two different depths, obtained with 17 scanning steps along x-axis ($\Delta x = 0.5$ mm). (a) Dose distribution in the first (superficial) slice. (b) Dose distribution in the focal slice.

4.5 Scan of an extended tumour mass

Since the tumour to irradiate could have an extension larger than the focal spot, a scan of the beam could be necessary. To scan the beam, the bed where the patient lies can be moved through remotely controlled motors while X-ray unit is kept fixed. Alternatively, due to the compactness of the system that we propose, it could be favourable to keep the bed fixed and move the source. A series of GAMOS simulations were carried out to demonstrate the capability of irradiating with good uniformity a target located at a depth of 4.75 cm and whose $x \times y \times z$ size is 0.8×0.2×1.2 cm. Given the target size, the focal spot size, and the depth of field, the beam has to be scanned along the x direction only. The step width depends on the required grade of uniformity of the dose delivered to the target volume. In particular, 9 steps with $\Delta x = 1.0$ mm were necessary to obtain an uniformity of 40%, while 17 steps with $\Delta x = 0.5$ mm leaded to an uniformity of about 7%. The total dose distribution inside the phantom is reported in Fig. 4.17 and Fig. 4.18 for the scan of 17 steps.

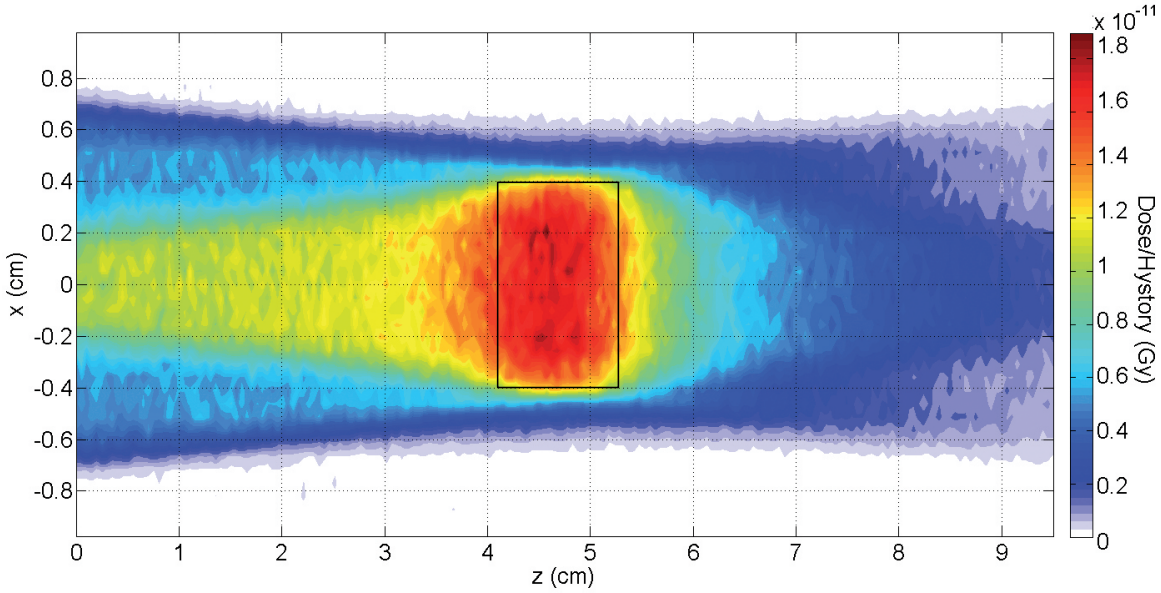

Figure 4.18: Dose distribution in the plane $y = 0$ obtained with 17 scanning steps along x-axis ($\Delta x = 0.5$ mm). The Black rectangle represents the target contour.

As can be seen, the purpose was reached while maintaining at the same time a relatively low dose in the neighbouring regions. However, in the case of a tumour extended in both traversal directions (x and y), a pure linear scan of the beam would cause a shift of the peak dose towards the phantom surface. This effect is due to the superposition of the beams and can be avoided by associating a rotation with each translation of the beam, as in Abbas et al. [105]. In particular, we envisage to translate and tilt the source in such a way that the X-rays hit different portions of the target from diverse angles. As shown in Fig. 4.19, a step Δx along the x-axis involves a rotation of the source by an angle $\Delta\alpha$ around the y-axis. Similarly, a step Δy along the y-axis is accompanied by a rotation by the same angle around the x-axis.

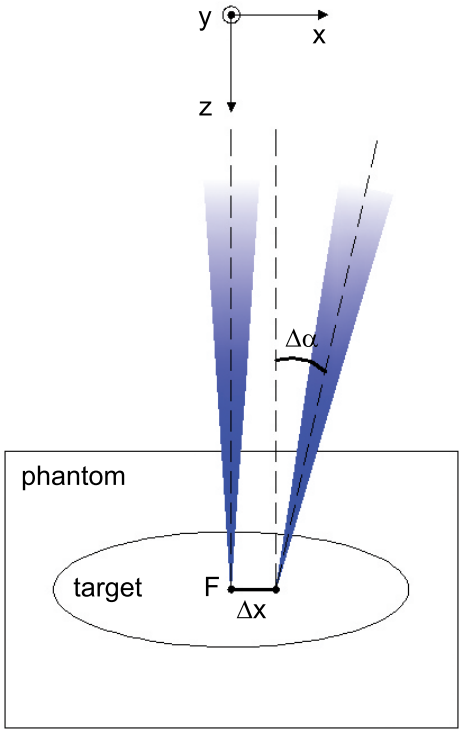

Figure 4.19: Schematic representation of an irradiation involving translation and tilt of the source.

In Fig. 4.20 and Fig. 4.21, the total dose distribution inside the phantom is reported for the case of a scan along x and y performed with 5 steps of 1 mm in each direction accompanied by a rotation of 2° at each step. As can be seen from the figures, the goal of broadening the focal spot, avoiding at the same time an excessive overlap of the beam before and after the focus itself, was achieved. A side effect consists in a shift in the depth of the focus of about 1 cm. However, one can easily take into account this contribution.

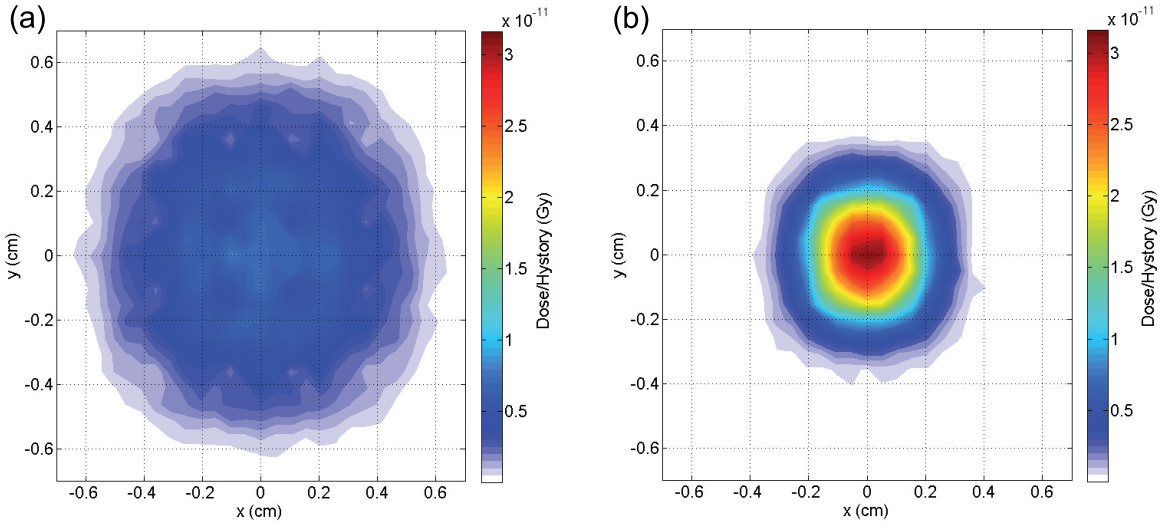

Figure 4.20: Dose distribution in two phantom slices lying at two different depths, obtained with 5 × 5 scanning steps along x-axis and y-axis ($\Delta x = \Delta y = 0.5$ mm, $\Delta\alpha = 2°$). (a) Dose distribution in the first (superficial) slice. (b) Dose distribution in the focal slice.

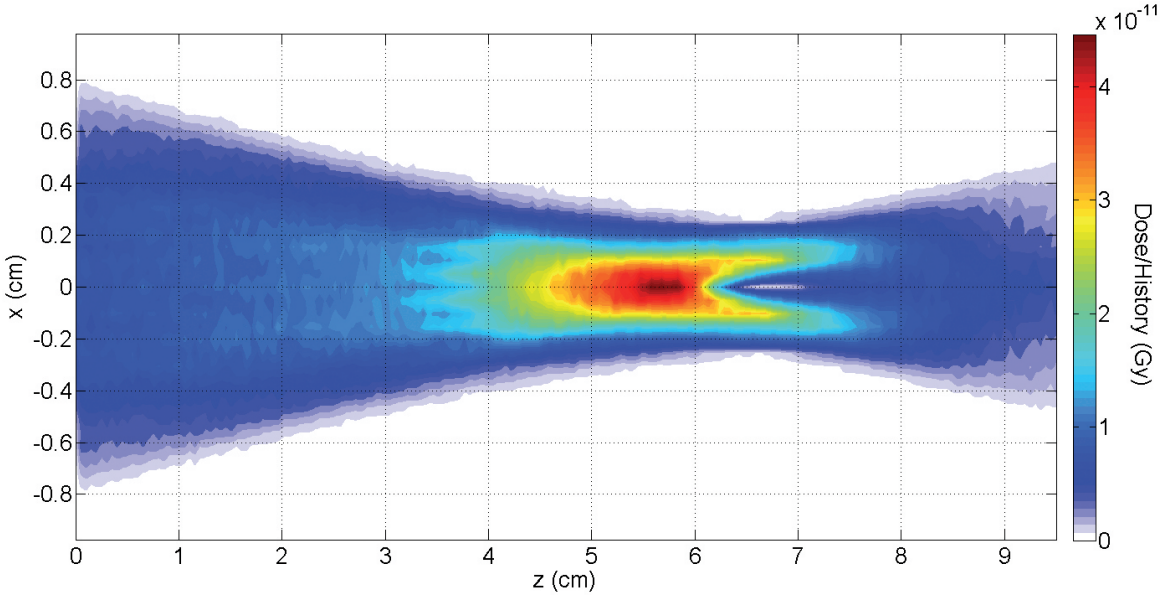

Figure 4.21: Dose distribution in the plane $y = 0$ obtained with 5 × 5 scanning steps along x-axis and y-axis ($\Delta x = \Delta y = 0.5$ mm, $\Delta\alpha = 2°$).

Chapter 5

Prototype of a Laue lens for radiation therapy

The fabrication of a Laue lens is an engineering problem that encompasses the physics of diffraction of high-energy radiation in crystals. Crystalline samples suitable to be used as optical elements for a Laue lens can be profitably produced exploiting one of the techniques described in chapter 2. The major issue in assembling a Laue lens concerns the stringent requirement on the alignment of the samples. In particular, for astrophysical applications involving focal lengths of the order of tens of meters, the maximum value for the misalignment angle with respect to the lens optical axis, φ_a, has to be as small as 10 arcsec in order to not spoil the sensitivity of the lens [92]. A Laue lens for nuclear medicine requires an alignment slightly less strict, tolerating a maximum value for φ_a of the order of 30 arcsec without a degradation of its imaging capability (see chapter 3). To achieve this level of accuracy, the research groups involved in the fabrication of Laue lenses have adopted an approach consisting in positioning each crystal tile on the lens support under the control of an X-ray beam. This implies the necessity of using a robotic system to position the samples and a very time-consuming procedure [93].

A Laue lens for radiotherapy tolerates a larger misalignment with respect to the previous cases. For example, the lens proposed in chapter 4 can be built with a maximum misalignment φ_a of the order of 60 arcsec without a significant degradation of its performance. Depending on the specific case, values of φ_a up to 120 arcsec could be still acceptable. Indeed, in this case, there is not the need of an extremely narrow focal spot since the lens is not used for imaging purposes. Due to the more relaxed requirements on the crystal alignment, a prototype of Laue lens for radiotherapy was developed at the Sensor and Semiconductor Laboratory (SSL) of Ferrara in the last months of 2015. This prototype represents the first

Table 5.1: Features of the lens prototype.

Photon energy band of interest	24 - 39 keV
Source-to-lens distance L_S	35 cm
Lens-to-detector distance L_D	35 cm
Number of rings of the lens	1 (radius $r = 22$ mm)
Crystals of the lens	4 QM silicon samples
Diffraction geometry	2
Diffracting planes	(111)
Traversal size of the crystals	$L_t \times L_r = 10 \times 10$ mm
Thickness of the crystals	$T_0 = 2$ mm
Radius of curvature of the crystals	Primary 80 m, QM 210 m

sample of Laue lens for medical applications produced so far by the SSL. It was conceived as a concept demonstrator using low energy photons and was assembled and tested exploiting the expertise and the equipment available at Ferrara.

5.1 Design and assembling of the prototype

A key point of the prototype design was to test the ability to align crystals through a mechanical method, avoiding the positioning under the control of an X-ray beam. Since the main goal was the alignment, a small numbers of diffracting crystals was chosen. The prototype was designed to diffract a photon beam with energy band 24 - 39 keV at a focal distance of 35 cm. The features of the lens prototype are listed in Table 5.1. The transversal size of the crystals was 10×10 mm, while the thickness traversed by the X-ray beam was 2 mm. The crystalline samples exploited (111) curved diffracting planes obtained through the quasi-mosaic (QM) effect, to increase the flux of the diffracted beam. The geometry 2 was used because the number of sample and their thickness traversed by beam were small.

The 4 silicon crystals composing the prototype were shaped through a high precision dicing saw (DISCO^{TM} DAD3220) from a commercial wafer with a diameter of 100 mm and a thickness of 2 mm. Furthermore, the *miscut angle*, namely the angle between the nominal direction of the wafer major face ($[11\overline{2}]$ in this case) and the actual direction was low, being less than 0.05°. Crystals were bent by sandblasting their $[11\overline{2}]$ face under the same conditions described in chapter 2. Sandblasting damaged a thin layer of the surface of the samples, which acted as a compressive film. As a consequence, the substrate of the samples was permanently deformed according to its elastic properties. Being the samples 2 mm thick, their expected primary radius of curvature was about 80 m, according to the model described in chapter 2. The primary curvature of the samples was measured through an optical profilometer (VEECO^{TM} NT1100) with 1 μm lateral and 1 nm vertical

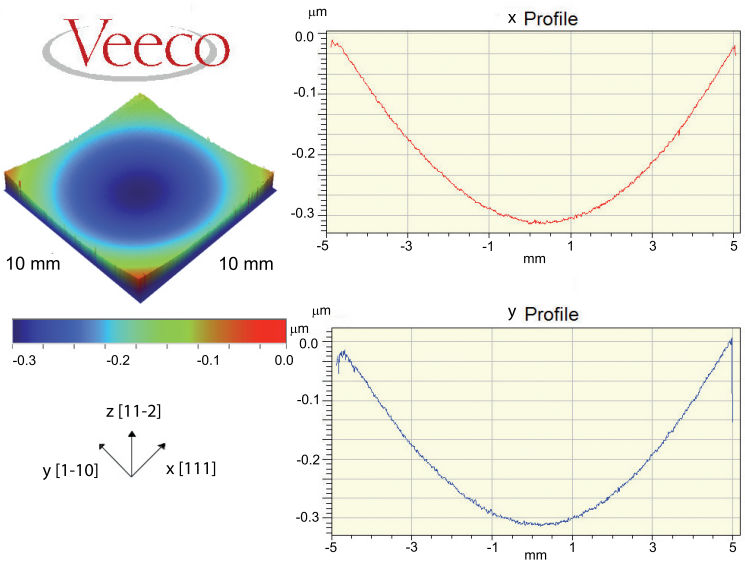

Figure 5.1: Interferometric measurement of the backside of a crystalline sample composing the lens prototype. Left side: 3D view analysis. Right side: Cross sections of the deformation pattern along x and y directions, as taken on the centre of the sample. The average radius of curvature along x is $R_x = 78.6$ m, while that along y is $R_y = 73.3$ m.

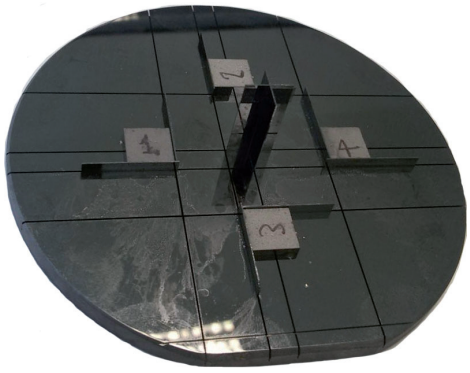

Figure 5.2: Photo of the assembled lens prototype.

resolution. Since the machined surface was damaged, the profilometric characterization was carried out on the back face of the samples. Fig. 5.1 shows the characterization of one of the samples. The measured radii of curvature along the main directions are in agreement with expectations. The radius of curvature of QM (111) diffracting planes, R_{111}, was calculated from the theory of linear elasticity (see Appendix A). It turned out to be about 206 m for this sample. In fact, for the crystallographic orientation of the crystals, it holds $R_{111}/R_x = 2.62$.

The fabricated crystalline samples were arranged in a cross configuration on a proper machined support. The centres of the crystals lied on a circle with a radius of 22 mm. The prototype support was a commercial 4 inches silicon wafer with a thickness of 5 mm and a miscut angle of 0.05°. On the surface of the wafer, a series of grooves were performed. The grooves hosted a series of thin (200 μm) silicon lamellae acting as a guidance for the

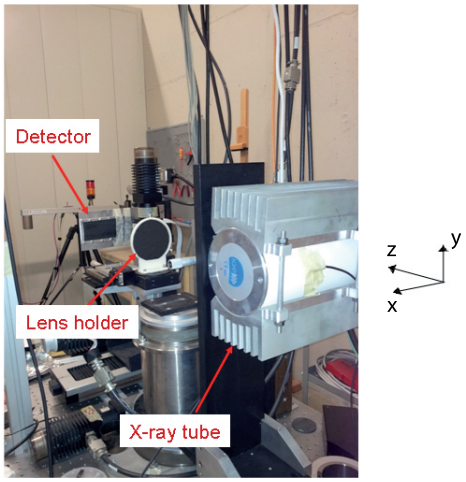

Figure 5.3: Photo of the experimental setup used to test the lens prototype at the LARIX.

positioning of the diffracting samples. Once the samples were in the correct position, they were fixed to the support through a special heat curable glue that minimized the stress imparted to the crystals during hardening. A photo of the prototype is shown in Fig. 5.2.

5.2 Test of the prototype

The assembled Laue lens prototype was tested at the LARge Italian X-ray facility (LARIX) of Ferrara. Within this laboratory, which is mainly aimed at testing X-ray optics for Astrophysics, an experimental line for research on medical imaging is also available. Measurements were carried out in collaboration with the medical physics research group of Ferrara.

The experimental setup used to test the prototype is shown in Fig. 5.3. The lens was positioned approximately halfway between an X-ray source and an imaging detector, the source-to-lens distance L_S being 35 cm. The source was a molybdenum anode X-ray tube, the features of which are listed in Table 5.2. The lens prototype was taken in position through a custom made holder, which was designed to perfectly house the lens support. A manual rotating stage (around y-axis) and a manual shifter (along z-axis) plus two motorized shifters (along x- and y-axis) were used to control the positioning of the prototype with respect to the X-ray beam. The detector was a matrix of CMOS photodiodes coupled with a scintillator. The features of the detector are reported in Table 5.3. A thin layer of small crystalline particles of Gadolinium Oxysulfide (GOS) enclosed in a graphite screen was chosen as a scintillator. Indeed, GOS is one of the most efficient scintillators available in terms of light output per incident X-ray energy. In addition, its high atomic number and density make it an effective absorber of X-rays. The scintillator was of the same size of the active area

Table 5.2: Feature of the X-ray tube used to test the lens prototype.

Anode material	Molybdenum
X-ray exit window	Beryllium
Filtration	absent
Focus size	150 μm
Maximum voltage	40 kV
Maximum current	30 mA
Maximum exposure time	5 s

Table 5.3: Features of the detector used to test the lens prototype.

Detector type	CMOS image sensor coupled with a scintillator
Detector model	RadEye®100 (Rad-icon imaging group)
Active area	49.2×98.3 mm^2
Number of pixels	512×1024
Size of each pixel	96×96 μm^2
Average dark current at 23°C	50000 electrons/s
Quantum efficiency at 550 nm	50%
Conversion gain	0.18 μV/electron
Number of grey level (GL)	2048 (11 bit)
Conversion factor	2.048 GL/mV
Scintillator type	Gadolinium Oxysulfide (GOS)
Scintillator thickness	50 μm
Scintillator light yield	77 photons/keV
Light collection efficiency	$\sim$ 40%
Scintillator enclosure	Graphite layer with a thickness of 0.5 mm

of the CMOS sensor and was mounted directly on the latter. The light collection efficiency was about 40 %.

X-ray tube and detector were aligned through a laser, while the alignment of the prototype with respect to the center of the X-ray beam emitted by the source was obtained by making a radiograph of the prototype and checking if the central cross realized using some silicon lamellae (see Fig. 5.2) was at centre of the image.

Once the prototype was aligned and a lead absorber was positioned on its backside to stop the direct beam near the optical (z) axis, the image on the detector due to the diffraction of the photon beam from the crystals was acquired. The lens-to-detector distance L_D was finely varied until the distance leading to a focused diffracted image was found. In fact, the actual focal distance was a few mm different from the theoretical value $L_D = L_S$ because of the primary curvature and the miscut of the crystals. In particular, the diffraction image was the sum of 10 images, each obtained acquiring the diffracted beam for 1 s with the X-ray tube set at 40 kV and 30 mA, namely at its maximum power. The obtained image was corrected by acquiring the *dark image* and the *white image*. The dark image was obtained with the

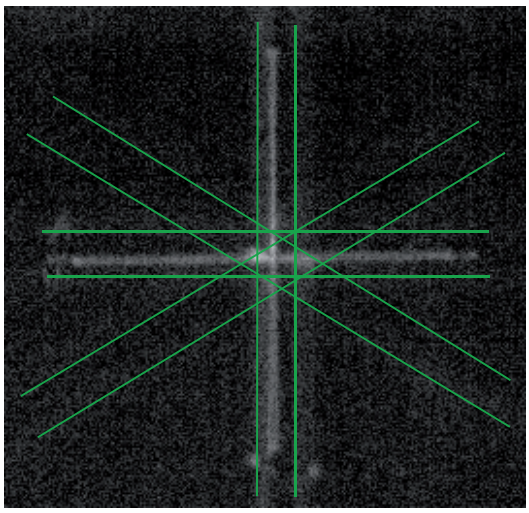

Figure 5.4: Corrected image due to X-ray diffraction from the crystals composing the prototype. The green lines highlight the diffraction pattern due to the crystalline support.

X-ray source off and thus, was due only to the thermally generated carrier within the CMOS sensor and the environmental background radiation. The white image was acquired with the source set at the operating point but without the Laue lens prototype. This image was useful to take into account any spatial inhomogeneity of the CMOS sensor. The grey level of the pixel (x, y) of the corrected image, $GL_{corr}(x, y)$, was calculated from the corresponding measured value $GL_{raw}(x, y)$ through the formula

$$GL_{corr}(x,y) =< GL_{white}(x,y) - GL_{dark}(x,y) > \frac{GL_{raw}(x,y) - GL_{dark}(x,y)}{GL_{white}(x,y) - GL_{dark}(x,y)}, \qquad (5.1)$$

where $GL_{dark}(x, y)$ and $GL_{white}(x, y)$ are the grey levels of the pixel (x, y) of the dark and white image respectively. $< GL_{white}(x, y) - GL_{dark}(x, y) >$ is the mean grey level of the image obtained subtracting the the dark image from the white image. The result of this operation is shown in Fig. 5.4.

Analysing the diffraction image, the goodness of the crystal alignment could be assessed. Each couple of crystals located at diametrically opposed points produced a single line with a length of about 20.3 mm, the expected value in the ideal case being $2L_t = 20$ mm. This enlargement is compatible with a maximum misalignment of the crystals with respect to the lens axis, φ_a, of about 90 arcsec. On the contrary, since the two diffraction lines resulted to be almost perfectly perpendicular, the azimuthal misalignment (described through the angle φ_b) was negligible. Since the support of the prototype was made of crystalline silicon like the 4 samples, a series of diffraction lines due to the support are also present in the image. These lines appear split because the centre of the support and the centre of the samples were 3.5 mm apart. Therefore, the diffraction images due the samples and the support could not

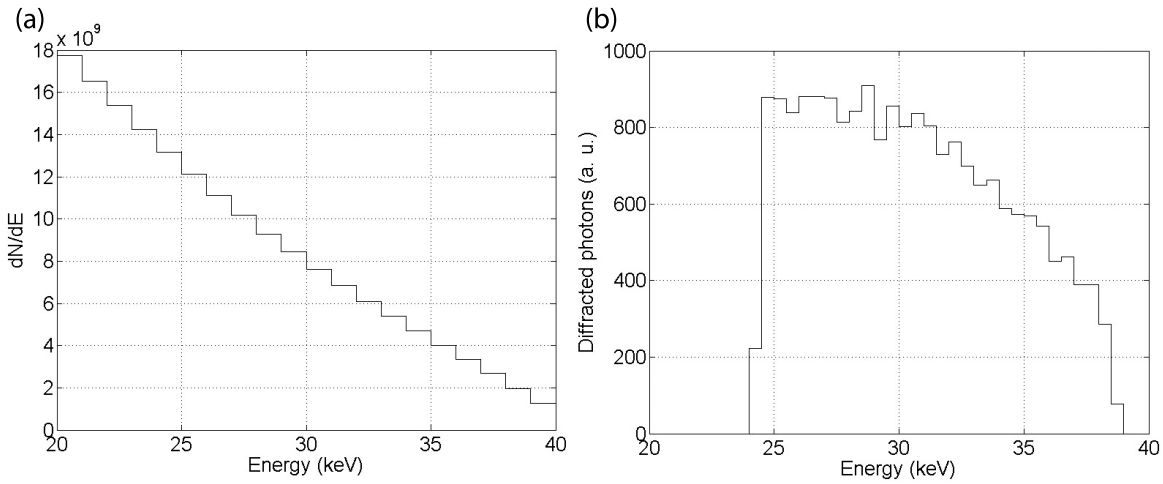

Figure 5.5: (a) Simulated spectrum of the X-ray tube (20 - 40 keV) for 1 s of irradiation. (b) Simulated spectrum of the photon beam diffracted by the lens.

be focused at the same time. This feature of the prototype is unwanted and in the future it can be avoided by using an amorphous support.

In order to get a deeper understanding of the experimental result, the experiment was simulated with the LAUETHER code. The properties of the crystals, the setting of the X-ray tube and the features of the detector were considered. The photon beam attenuation due to air and to the lens support, as well as an estimation of the Compton scattered photons were also taken into account. The diffraction process was modeled as described in chapter 4. Fig. 5.5 shows the spectrum of the source and the spectrum of the diffracted beam respectively. The number of diffracted photons per mAs of the X-ray tube was $N_D = 2.6 \times 10^4$.

The image formation on the detector was modeled as follows. First, the arrival point of the X photons on the focal plane was binned. The bin width was 96 μm, namely the size of a pixel of the CMOS sensor. The resulting distribution was convolved with a Gaussian function centred in zero and having a FWHM of 50 μm and a unit area. In this way, the spreading due to the scintillator was taken into account. This procedure was carried out for each energy of the X photons. In particular, the bandpass of the lens was subdivided in n_{bin} bins, whose central value was E_i. Therefore, the number of photons with energy E_i firing the pixel of coordinates (x, y) was calculated. This value was indicated with $N_i(x, y)$. Then, the energy deposited in each pixel $E_{dep}(x, y)$ was calculated as follows

$$E_{dep}(x,y) = \sum_{i=1}^{n_{bin}} N_i(x,y) \exp(-\mu_G(E_i)t_G) \frac{\mu^{en}_{GOS}(E_i)}{\mu_{GOS}(E_i)} E_i(1 - \exp(-\mu_{GOS}(E_i)t_{GOS})), \quad (5.2)$$

where t_G and t_{GOS} are the thicknesses of the graphite screen and the scintillating GOS layer respectively. $\mu_G(E_i)$ is the linear attenuation coefficient of graphite at energy E_i, $\mu^{en}_{GOS}(E_i)$

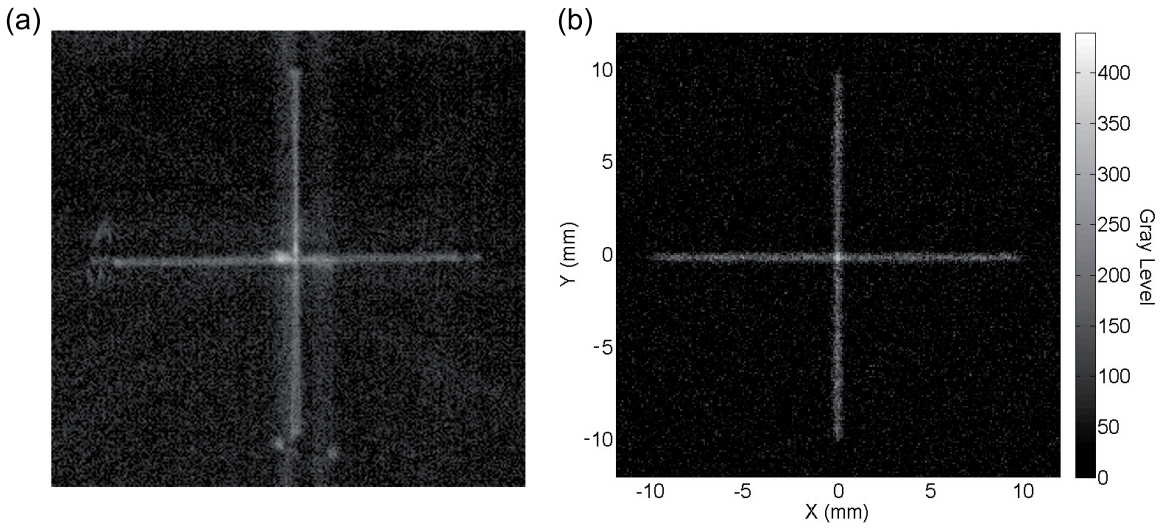

Figure 5.6: Comparison between the experimental (a) and the simulated (b) image produced by the crystals of the lens on the detector. The experimental image was corrected subtracting the dark and the white images.

and $\mu_{GOS}(E_i)$ are the energy-absorption coefficient and the linear attenuation coefficient of GOS at energy E_i respectively [91]. Once the energy deposited in each pixel was known, the corresponding grey level $GL(x, y)$ was calculated as

$$GL(x, y) = \alpha \cdot \beta \cdot \eta \cdot \gamma \cdot \delta \cdot E_{dep}(x, y), \tag{5.3}$$

where are α is the scintillator light yield, β the light collection efficiency, η the quantum efficiency of the CMOS photodiodes, γ the conversion gain, and δ the GL/mV conversion factor. The values of these parameters are listed in Table 5.3.

The comparison between the experimental and the simulated image is shown in Fig. 5.6. The simulation was carried out under the assumption that there was no error in the positioning of the samples ($\Delta pos = 0$), nor azimuthal misalignment ($\varphi_b = 0$). While, a misalignment of the samples with respect to the lens axis was hypothesized. For each sample, the misalignment angle φ_a was set choosing a value uniformly at random from the interval [-90,90] arcsec. Indeed, the maxim misalignment angle inferred from the experimental image was 90 arcsec. Fig. 5.6 shows a very good agreement between experiment and simulation, providing a first validation of the LAUTHER code and of the used models. Moreover, the results of the characterization show that the achieved accuracy in the positioning of the samples is satisfactory. A maximum misalignment of 90 arcsec is a very good performance for a mechanical alignment method, which is much more simple, economic and time-saving with respect to a X-ray assisted positioning method. Thus, the goal of the experiment

has been reached. Moreover, it has been demonstrated that the assembling of a effective prototype of a Laue lens for radiotherapy is within reach. As a development of this work, further prototypes will be fabricated through the proposed method. A key point will be to increase the number of crystals composing the prototype and reduce their transversal size, maintaining the same level of alignment.

Conclusions

The aim of this thesis is to describe study and realization of Laue lenses for medical applications. Since a Laue lens exploits the diffraction of high-energy radiation from crystals, their performance strongly depends on the choice of the crystals themselves. From the short review provided in chapter 1, crystals with curved diffracting planes (CDP) emerged as the best optical elements for a Laue lens devoted to a medical application. Indeed, they guarantee a high integrated reflectivity and can be fabricated in such a way to provide a good focusing power to the lens. CDP crystals can be arranged in a Laue lens according to two geometries. The geometry 1, which foresees that the photon beam enter the crystals from their minor face and that the crystals are bent only along the direction of propagation of the beam, has been recognized as the most suitable geometry for a medical application. Indeed, In this way, a large number of crystals can be arranged even in a very compact lens. There are many way to bend a crystal, each of them has positive and negative aspects. The most used bending techniques have been described in chapter 2, together with three innovative methods developed at SSL. Among these, the sandblasting method emerged as the most suitable to fabricate self-standing CDP crystals with a thickness up to few mm and a radius of curvature of the diffracting planes down to some tens of m. This method is economic, reproducible, and fast. Thus, it is suitable for mass production. All of these features are very important when one has to assemble a compact device composed of many identical parts like a Laue lens for medical applications.

The design principles of Laue lenses optimized for both diagnostic purposes in nuclear medicine and radiotherapy have been described in this thesis.

In chapter 3, it has been demonstrated that a system of Laue lenses capable of providing a high-resolution functional image of a small region of the patient's body can be obtained by properly selecting the features of the crystals. A limitation is due to the fact that the transaxial field of view is limited to the radial size of the crystals and ranges within 0.3-5 mm. By moving the bed where the patient lies, it would be possible to perform a high-resolution scan over a region of interest of a few of cm^2 in a reasonable amount of time. The obtained

image may help the specialists to gain a better understanding of some metabolic processes or to recognize more accurately the extension and the position of a tumour mass in an early stage of evolution. Generally speaking, the lens could be used in those cases where the results of a conventional diagnostic exam are doubtful. Due to its capability, an ensemble of Laue lenses could be also exploited for performing in vivo functional imaging in small animals, allowing the study of complex processes such as mutagenesis and carcinogenesis.

In chapter 4, it has been demonstrated that a specifically designed Laue lens could also be used in radiotherapy, in combination with an X-ray tube, for producing a convergent X-ray beam capable of releasing the maximum dose to a tumour target while sparing the surrounding normal tissues. It has been shown how the features of the crystals composing the lens can be chosen to maximize the photon yield of the lens and, at the same time, optimize the size of the focal spot. In this way, an effective system capable of a high precision in the dose deposition could be designed. The proposed system can be exploited for irradiating both sub-cm and larger tumours. In the former case, a single irradiation of few seconds with a convergent beam could be sufficient. In the latter case, a scan of the beam is required. In this case, a linear scan accompanied by a rotation of the beam might be exploited to avoid of delivering too high a superficial dose with respect to the dose given near the focus. It was not the purpose of this work to identify the oncological pathologies that could be best treated using the proposed methodology. This task, as well as a comparison with hadron therapy and conventional radiotherapy will be accomplished in a future work. Generally speaking, it can be envisaged that the proposed technique may be very effective when it is necessary to treat small tumours located just before radiosensitive organs. This can be done with hadron therapy, but one of the main advantages of using a system based on a Laue lens with respect to a hadron therapy system relies in the cost and the size of the former, which are orders of magnitude lower than that of the latter.

An important feature of a Laue lens suitable for radiotherapy is the relaxed requirement on crystal alignment, which represented so far the main issue in assembling a Laue lens for astrophysics or nuclear medicine. As described in chapter 5, a prototype of Laue lens for radiotherapy was successfully assembled at SSL and tested at the LARIX laboratory in collaboration with the medical physics group of Ferrara. The prototype was composed of a small number of crystals and the size of the latter was not optimal from the point of view of the precision in the dose delivery, however, the mechanical tolerances required for the realization of an effective Laue lens were fulfilled. Thus, the realized prototype represents the first step toward the assembling of an effective Laue lens that could be really used in a radiotherapy treatment. Such a lens requires a rather large number (hundreds)

of mm-sized bent crystals to guarantee a high precision in the dose delivery and a high flux of diffracted photons. Recently, the Italian National Institute for Nuclear Physics (INFN) funded LAUPER, a project aimed at demonstrating the feasibility of such kind of lens. Within the framework of this project, the full potentiality of the assembly methods proposed in this thesis will be assessed.

Appendices

Appendix A

Theory of linear elasticity in crystals

Primary and secondary curvatures within a crystal can be calculated through the theory of linear elasticity. Elasticity expresses the relationship between stress σ (force per unit area) and strain ε (ratio of deformation over initial length) in a medium. A crystal can be considered as a homogeneous continuous medium rather than as a periodic array of atoms for elastic waves of wavelength longer than 10^{-8} m (i.e. with frequencies below 10^{11} - 10^{12} Hz). In the linear approximation, stress and strain are linked by first order equations. In particular, for Si and Ge the relationships between stresses and strains are linear up to the breaking point [116]. In tensor notation, it is:

$$\begin{aligned} \sigma &= C\epsilon, \\ \epsilon &= S\sigma, \end{aligned} \tag{A.1}$$

where C is the tensor of stiffness and S the tensor of compliance, $S = C^{-1}$. Once the crystallographic orientation of the crystals has been set, S and C contain all the useful information about the elastic behaviour of the sample. In general, fourth-rank tensors 3×3×3×3 are needed when dealing with S and C. However, owing to the symmetry of the stress and strain fields, the stress-strain relationship can be represented through second-order tensors by using the Voigt compact notation. Thus, without loss of generality, stiffness and compliance tensors are completely defined by 6×6 matrices. It is

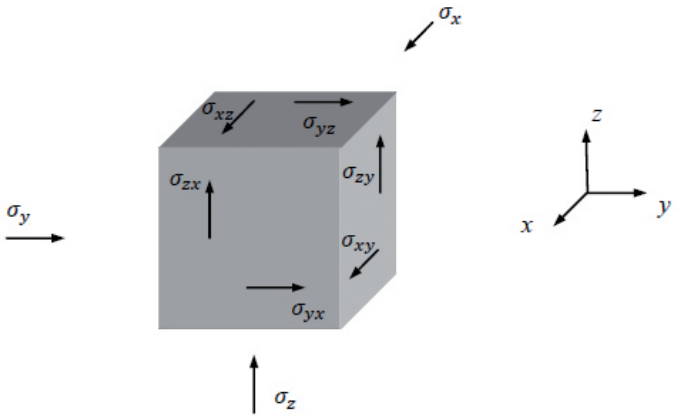

Figure A.1: Stress tensor components.

$$\begin{pmatrix}\sigma_1\\ \sigma_2\\ \sigma_3\\ \sigma_4\\ \sigma_5\\ \sigma_6\end{pmatrix} = \begin{pmatrix} C_{11} & C_{12} & C_{13} & C_{14} & C_{15} & C_{16} \\ & C_{22} & C_{23} & C_{24} & C_{25} & C_{26} \\ & & C_{33} & C_{34} & C_{35} & C_{36} \\ & & & C_{44} & C_{45} & C_{46} \\ & Sym & & & C_{55} & C_{56} \\ & & & & & C_{66} \end{pmatrix} \begin{pmatrix}\varepsilon_1\\ \varepsilon_2\\ \varepsilon_3\\ \varepsilon_4\\ \varepsilon_5\\ \varepsilon_6\end{pmatrix}, \tag{A.2}$$

where, for the Voigt notation, the indices ranging from 1 to 6 correspond to the following directions

$$\begin{aligned} 1 &\longrightarrow x, \\ 2 &\longrightarrow y, \\ 3 &\longrightarrow z, \\ 4 &\longrightarrow yz, \\ 5 &\longrightarrow zx, \\ 6 &\longrightarrow xy. \end{aligned}$$

The stress tensor components acting on a unit volume are shown in Fig. A.1. As aforementioned, the shear stress components are symmetric, thus $\sigma_{yx} = \sigma_{xy}$, $\sigma_{yz} = \sigma_{zy}$, and $\sigma_{xz} = \sigma_{zx}$. It is also worth noting that they are often indicated with the Greek letter τ instead of σ.

The Si and Ge C tensors for ([100], [010], [001]) as (xyz) axes are well known in the

literature:

$$C_{Si} = \begin{pmatrix} 165.64 & 63.94 & 63.94 & 0 & 0 & 0 \\ 63.94 & 165.64 & 63.94 & 0 & 0 & 0 \\ 63.94 & 63.94 & 165.64 & 0 & 0 & 0 \\ 0 & 0 & 0 & 79.51 & 0 & 0 \\ 0 & 0 & 0 & 0 & 79.51 & 0 \\ 0 & 0 & 0 & 0 & 0 & 79.51 \end{pmatrix} GPa,$$

$$C_{Ge} = \begin{pmatrix} 129.2 & 47.9 & 47.9 & 0 & 0 & 0 \\ 47.9 & 129.2 & 47.9 & 0 & 0 & 0 \\ 47.9 & 47.9 & 129.2 & 0 & 0 & 0 \\ 0 & 0 & 0 & 67.0 & 0 & 0 \\ 0 & 0 & 0 & 0 & 67.0 & 0 \\ 0 & 0 & 0 & 0 & 0 & 67.0 \end{pmatrix} GPa.$$

Since crystals are inherently anisotropic media, their elastic properties depend on the crystallographic orientation. To calculate the anisotropic properties along an arbitrary crystallographic orientation, the C and S tensors for ([100], [010], [001]) orientation have to be rotated so that the axes are aligned with the directions of interest:

$$\begin{aligned} C' &= \Omega C \Omega^T, \\ S' &= \Omega S \Omega^T. \end{aligned} \tag{A.3}$$

It is not straightforward to calculate the orthogonal rotation tensor Ω. The complete formulae needed for the transformation can be found in [61].

Three important parameters used to describe the elastic properties of a medium are the Young's modulus, the Poisson's ratio and the shear modulus. They are here described:

- The Young's modulus or elastic modulus E is the ratio of normal stress σ along an axis over the deformation ε along that axis. Thus, it represents a measure of the stiffness of an elastic material.

- The Poisson's ratio (ν) describes the deformation of a body occurring along a direction orthogonal to the direction of applied tension. Usually, it assumes positive value, thus if a body is stretched, it exhibits a transverse contraction.

- The shear modulus or modulus of rigidity (G) describes the material response to shear stress.

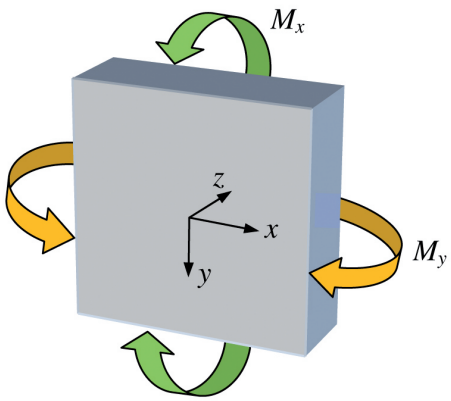

Figure A.2: Couples of moments applied to an anisotropic thin plates.

They can be calculated in terms of the (rotated) compliance tensor as follows:

$$E_j = \frac{1}{S_{jj}}, \tag{A.4}$$

$$v_{ij} = -\frac{S_{ji}}{S_{ii}}, \tag{A.5}$$

$$G_{ij} = \frac{|\epsilon_{ijk}|}{S_{k+3,k+3}}, \tag{A.6}$$

with i,j=1,2,3 and ϵ the Levi-Civita tensor.

The complete description of the deformations in anisotropic bodies can be found in [117]. For our purposes, crystals can be modeled as a thin rectangular plate (e.g. [82]). Moreover, the load acting on a crystal can be equivalently described by a system of bending moments acting only at the edges of the sample [118], according to the scheme depicted in Fig. A.2. The curvature of the crystallographic planes can be calculated through the displacement field described by $u(\mathbf{r})$, $v(\mathbf{r})$, and $w(\mathbf{r})$, which are the displacements along the x-, y-, and z-axis respectively. The displacements can be calculated trough their relationship with the deformations. In turn, the deformations can be obtained once the stress tensor components are known.

$$\begin{gathered} \varepsilon_x = \frac{\partial u}{\partial x}, \quad \varepsilon_y = \frac{\partial v}{\partial y}, \quad \varepsilon_z = \frac{\partial w}{\partial z}, \\ \varepsilon_{xy} = \frac{\partial u}{\partial y} + \frac{\partial v}{\partial x}, \quad \varepsilon_{yz} = \frac{\partial v}{\partial z} + \frac{\partial w}{\partial y}, \quad \varepsilon_{zx} = \frac{\partial w}{\partial x} + \frac{\partial u}{\partial z}. \end{gathered} \tag{A.7}$$

The normal (σ) and tangential (τ) components of the stress tensor are bound up to me-

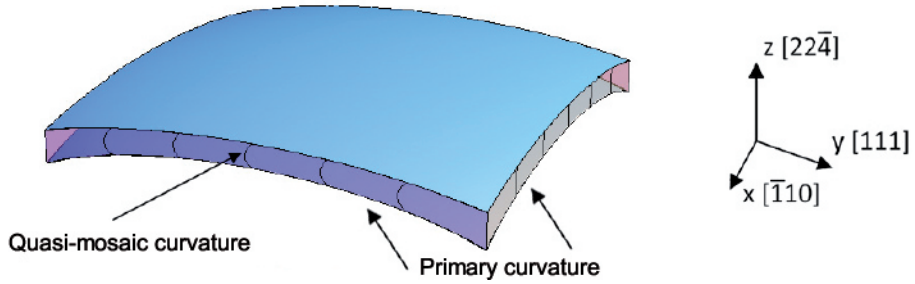

Figure A.3: Schematic representation of a crystal plate with the coordinate system used for the modeling. Two moments are applied to the sample. Crystallographic orientation and quasi-mosaic curvature are highlighted.

chanical moments M_x and M_y applied to the crystal via

$$\begin{aligned} \sigma_x = \frac{M_y}{I_y} z, \quad \sigma_y = \frac{M_x}{I_x} z, \quad \sigma_z = 0, \\ \tau_{yz} = 0, \quad \tau_{xz} = 0, \quad \tau_{xy} = 0, \end{aligned} \tag{A.8}$$

where I_x and I_y are the moments of inertia about x- and y-axis respectively. Under the following boundary conditions

$$\left.\frac{dw}{dx}\right|_0 = \left.\frac{dw}{dy}\right|_0 = 0, \qquad \frac{dv}{dx} - \frac{du}{dy} = 0, \qquad u(0) = v(0) = w(0) = 0, \tag{A.9}$$

which impose that there is no deformation and displacement in the center of the plate nor a rigid rotation, the displacement field arising from the deformation of a crystal plate turns out to be

$$\begin{aligned} u = \frac{1}{2I_y}[M_y(S_{51}z^2 + S_{61}yz + 2S_{11}xz)] + \\ \frac{1}{2I_x}[M_x(S_{52}z^2 + S_{62}yz + 2S_{12}xz)], \\ v = \frac{1}{2I_y}[M_y(S_{41}z^2 + 2S_{21}yz + S_{61}xz) + \\ \frac{1}{2I_x}[M_x(S_{42}z^2 + 2S_{22}yz + S_{62}xz)], \\ w = \frac{1}{2I_y}[M_y(S_{31}z^2 - S_{11}x^2 - S_{12}y^2 - S_{16}xy + \\ \frac{1}{2I_x}[M_x(S_{32}z^2 - S_{12}x^2 - S_{22}y^2 - S_{26}xy)], \end{aligned} \tag{A.10}$$

where S_{ij} are the components of compliance tensor referred to the (x, y, z) Cartesian system. These three values completely define the displacement field of the crystal plate. Once the crystal features and the crystallographic orientation are set, by differentiating twice equations A.10 with respect to x, y, and z, the curvature along a given axis can be calculated. As an example, let us consider the configuration described in Fig. A.3. In this case, the

compliance tensor for silicon is

$$S = \begin{pmatrix} 0.591871 & -0.0960531 & -0.155125 & 0.167081 & 0 & 0 \\ -0.0960531 & 0.532799 & -0.0960531 & 0 & 0 & 0 \\ -0.155125 & -0.0960531 & 0.591871 & -0.167081 & 0 & 0 \\ 0.167081 & 0 & -0.167081 & 1.73028 & 0 & 0 \\ 0 & 0 & 0 & 0 & 1.49399 & 0.334162 \\ 0 & 0 & 0 & 0 & 0.334162 & 1.73028 \end{pmatrix} 10^{-11} Pa^{-1}.$$

If we apply two momenta M_x and M_y to the sample, the curvature of middle plane of the plate along x and y, i.e., the principal curvature on the two perpendicular directions, turns out to be

$$\begin{aligned} \frac{1}{R_{P_x}} &= \frac{\partial^2 w}{\partial^2 x} = -\left(\frac{M_y}{I_y} S_{11} + \frac{M_x}{I_x} S_{12}\right), \\ \frac{1}{R_{P_y}} &= \frac{\partial^2 w}{\partial^2 y} = -\left(\frac{M_y}{I_y} S_{12} + \frac{M_x}{I_x} S_{22}\right). \end{aligned} \tag{A.11}$$

The secondary curvatures, namely those arising within the solid as a consequence of the primary curvature, can also be calculated. They strongly depends on the crystallographic orientation, and in particular on the terms S_{41}, S_{42}, S_{51}, and S_{52} of the compliance tensor. For the case sketched in Fig. A.3 these terms are not null and a QM curvature in yz planes is present

$$\frac{1}{R_{QM}} = \frac{\partial^2 v}{\partial^2 z} = \frac{M_y}{I_y} S_{41} + \frac{M_x}{I_x} S_{42}. \tag{A.12}$$

Considering a spherical curvature with $M_x/I_x = M_y/I_y$, the ratio between the primary and the QM curvatures is

$$\frac{R_{QM}}{R_{P_y}} = -\frac{S_{12} + S_{22}}{S_{42} + S_{42}}. \tag{A.13}$$

Thus, imparting a spherical bending to $(22\overline{4})$ Si plates results in a QM curvature of the (111) planes. Experimental evidence of X-ray diffraction with a silicon sample that exploited (111) planes bent through the quasi-mosaic effect can be found in [82].

Appendix B

Features of diffraction of high-energy radiation in CDP crystals

B.1 Modelization of the diffraction process in the LAUENM code

The LAUENM code allows the user to design and simulate optimized Laue lens for diagnostic nuclear medicine. The code was developed as an ensemble of MATLAB scripts and functions [86]. MATLAB was chosen because of its excellent capabilities of managing vectorial and matricial data as required when dealing with Laue lenses. Moreover it permits to parallelize complex numerical calculations through the Parallel Computing Toolbox. As mentioned in chapter 2, LAUENM is divided in three main functional modules. The pre-processing module manages the source and the geometry of the lens, the processing module simulates the diffraction process and the post-processing module computes the image on a detector and all the figures of merit regarding the lens.

In LAUENM, the diffraction process is modeled as follows.

- A photon is generated in a random direction defined by the polar angle θ and the azimuthal angle φ from a point S of the source (see Fig. B.1).
- The program assesses if the photon impinges on a crystal of the lens (whose nominal Bragg angle is θ_B), otherwise another photon is generated.
- The program checks if the angular deviation $\Delta\theta = \theta - \theta_B$ is smaller than the angular acceptance of the crystal, otherwise another photon is generated.

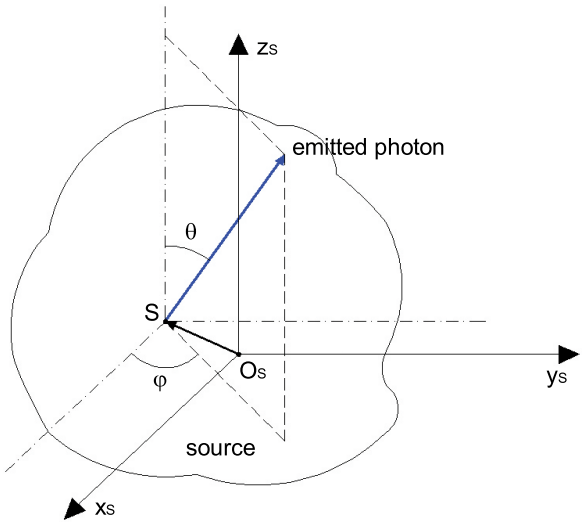

Figure B.1: Sketch of photon emission. The polar angle θ and the azimuthal angle φ of the photon are indicated. The source volume is divided in several identical cubic voxels. Each voxel is considered as an isotropic point source (point S).

- The program calculates the potential diffraction point within the crystal.
- A random number with uniform distribution within [0,1] is generated. If this number is lower than the crystal reflectivity, then diffraction occurs, otherwise another photon is generated.
- The program calculates the arrival point $P_{DET} = (x_{DET}, y_{DET})$ on the detector plane.

Fig. B.2 and Fig. B.3 depict the diffraction process occurring in a crystal of the lens and show the systems of coordinates used by the program.

Three coordinate systems are exploited to describe the diffraction process. The main one is the system $Oxyz$ with origin at the centre of the lens. The second coordinate system is parallel to the previous one but it is centred at point O_S. This frame is used to describe the shape of the source. The third coordinate system $Ox'y'z'$ is obtained by rotating the system $Oxyz$ around the z axis by an angle equal to the azimuth of the crystal where diffraction potentially occurs. Thus, this latter system depends on the photon we are considering.

As aforementioned, a photon emitted by the source with a polar angle within the angular acceptance of a crystal could be diffracted, thus the program calculates the potential point of diffraction. Let θ_B be the nominal Bragg angle and φ_M the azimuthal angle of the crystal, respectively. First, z'_D, namely the coordinate of the diffraction point along the lens axis in the $Ox'y'z'$ frame, is calculated depending on the type of crystal. If the crystal is a mosaic, a random value within the crystal is taken. If the crystal is a CDP, the program takes the

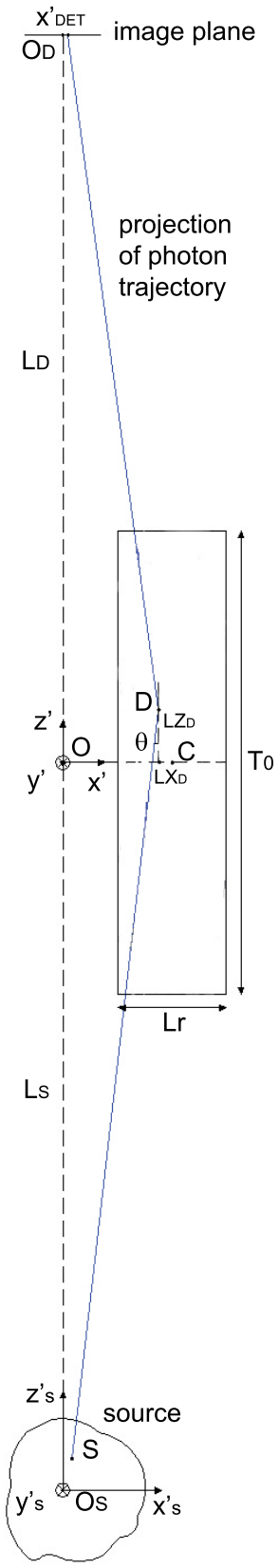

Figure B.2: Sketch of diffraction process of a photon within a crystal (*side view*).

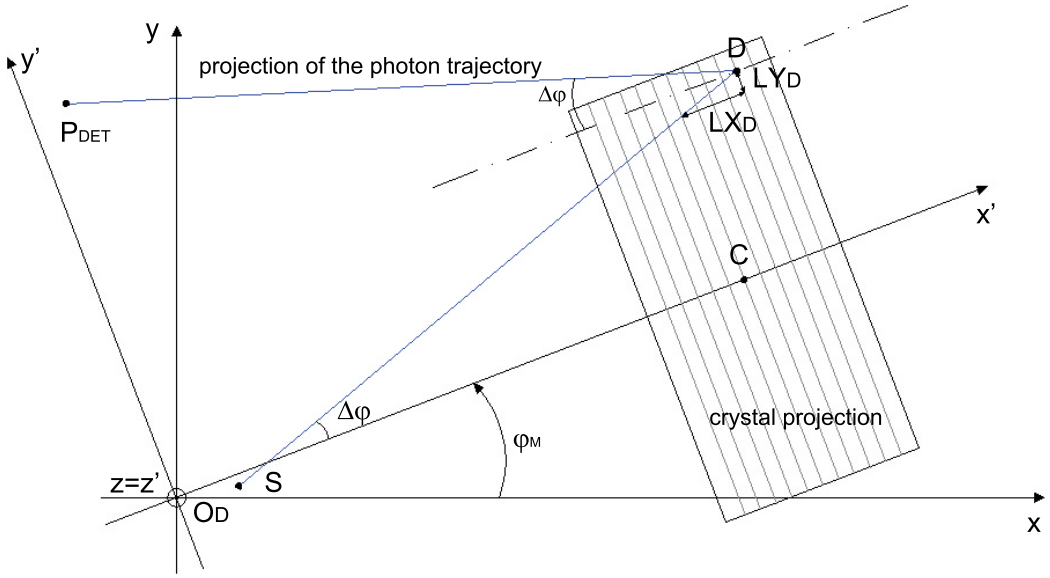

Figure B.3: Sketch of diffraction process of a photon within a crystal (*top view*).

coordinate where the Bragg condition is satisfied

$$z'_D = LZ_D = -\frac{T_0}{\Omega}(\Delta\theta + \varphi_a)\cos\varphi_a + \Delta z, \tag{B.1}$$

where T_0 is the thickness traversed by the photon beam, Ω the angular acceptance (bending angle), φ_a the axial misalignment, and Δz the mispositioning of the crystal in z direction.

For both types of crystals x'_D and y'_D are calculated. A intermediate step consists in calculating the parameters LX_D, LY_D, LZ_D shown in Fig. B.2 and Fig. B.3. From trigonometric considerations, we have

$$\begin{aligned} LX_D &= z'_D\theta + \Delta\theta L_S + x'_s - z'_s\theta - \varphi_a + \Delta x, \\ LY_D &= LX_D \tan\Delta\varphi, \end{aligned} \tag{B.2}$$

Where x'_s, y'_s, z'_s are the coordinates of the point of the source which emitted the photon, L_S the source-to-lens distance, $\Delta\varphi = \varphi - \varphi_M$, and Δx the mispositioning of the crystal in x direction. x'_D and y'_D are

$$\begin{aligned} x'_D &= r + LX_D, \\ y'_D &= (r - x'_s)\tan\Delta\varphi + y'_s + LY_D, \end{aligned} \tag{B.3}$$

r being the radius of ring where the crystal lies.

$\boldsymbol{k_h} = (1, -\tan\Delta\varphi, -1/\theta_e)$, where $\theta_e = \theta_B - \Delta\theta + \varphi_a$, is a vector parallel to the diffracted

photon trajectory. The arrival point on the detector can be calculated as the intersection of the line passing for the point of diffraction (x'_D,y'_D,z'_D) and parallel to vector $\boldsymbol{k_h}$ and the plane of equation $z' = L_D$, where L_D is the lens-to-detector distance. In the frame $Ox'y'z'$, it results

$$\begin{aligned} x'_{DET} &= x'_D - (L_D - z'_D)\theta_e, \\ y'_{DET} &= y'_D + (L_D - z'_D)\theta_e \tan(\Delta\varphi - \varphi_b). \end{aligned} \tag{B.4}$$

The same point is calculated in the frame $Oxyz$ through a rotation of the axes

$$\begin{aligned} x_{DET} &= x'_{DET}\cos\varphi_M - y'_{DET}\sin\varphi_M, \\ y_{DET} &= x'_{DET}\sin\varphi_M + y'_{DET}\cos\varphi_M. \end{aligned} \tag{B.5}$$

It is worth noting that, considering a perfect crystal alignment and positioning ($\varphi_a = \varphi_b = 0$ and $\Delta x = \Delta y = \Delta z = 0$), an azimuthal angle equal to zero ($\varphi = \varphi_M = 0$), a point source centred in O_S ($x'_s = y'_s = z'_s = 0$), the source-to-lens distance equal to the lens-to-detector distance ($L_D = L_S$), we obtain the same equations presented in chapter 3, provided to identify x_D with LX_D, y_D with LY_D and z_D with LZ_D.

B.2 Focusing/defocusing properties of CDP crystals

Under the assumptions mentioned at the end of the previous section, the focusing/defocusing properties of CDP crystals can be demonstrated.

Using the formalism adopted in chapter 3, the coordinates of the arrival point on the detector plane can be rewritten as

$$\begin{aligned} x_{DET} &= r + x_D - (L_S - z_D)(\theta_B - \Delta\theta), \\ y_{DET} &= 0. \end{aligned} \tag{B.6}$$

Substituting $r = \theta_B L_S$ and $z_D = -T_0/\Omega\Delta\theta$ in the previous relations, it turns out

$$\begin{aligned} x_{DET} &= -\frac{2\Delta\theta}{\Omega}(T_0\theta_B - \Omega L_S), \\ y_{DET} &= 0. \end{aligned} \tag{B.7}$$

Calculating these relations for $\Delta\theta = -\Omega/2$ and $\Delta\theta = +\Omega/2$ and taking the absolute value of the difference between the results, we obtain the width W of the profile on the image

plane due to diffraction from a crystal

$$W = |2T_0\theta_B - 2\Omega L_S|, \tag{B.8}$$

as is claimed in this thesis. Furthermore, taking into account the contribution of the photon azimuthal angle φ, it is possible to calculate the length L of the line obtained as an image of each crystal. Indeed, from Fig. B.3, it results that $\Delta\varphi_{max} = \arctan L_t/2r$. Thus, if we consider photons emitted by the source with a polar angle $\theta = \theta_B$, we obtain $y_{DET_{max}} = 2r \tan \Delta\varphi_{max}$. Therefore

$$L = 2y_{DET_{max}} = 2L_t, \tag{B.9}$$

as is claimed in chapters 3 and 4. A curvature of the crystal along the tangential direction (sagittal curvature) would reduce the value of L and improve the focusing capabilities of the sample. However, an appreciable effect is not achievable in practice, because of the stiffness of the small crystals suitable for a Laue lens devoted to medical applications.

So far we considered photons impinging on concave[1] diffracting planes. If photons impinge on convex diffracting planes, equation (B.8) becomes

$$W = |2T_0\theta_B + 2\Omega L_S|. \tag{B.10}$$

For a flat crystal $W = 2T_0\theta_B$, thus photons impinging on convex diffracting planes always cause an enlargement of the diffraction profile, namely a defocusing effect (see Fig. B.4.b). On the contrary, if the photons impinge on concave diffracting planes, a focusing or a defocusing effect arises depending on the value of the radius of curvature of the diffracting planes $R_C = T_0/\Omega$. If $R_C < L_S/(2\theta_B)$, there is a defocusing effect, otherwise a focusing effect (see Fig. B.4.a). If $T_0\theta_B = \Omega L_S$, namely $R_C = L_S/\theta_B$, a perfect focusing occurs in x direction. In fact, all the diffracted photons impact the image plane in $x_{DET} = 0$. Unfortunately, this condition can not be exploited for improving image resolution. Indeed, because of the lack of sagittal curvature there is a defocusing in y direction causing the spread of the photon distribution on the detector. It is worth noting that these results hold also in the case of a polychromatic source, though the case treated here concerns a monochromatic source.

The focusing capability of CDP crystals can also be put in evidence as follows. Let us

[1] The intuitive meaning of the term has to be intended here

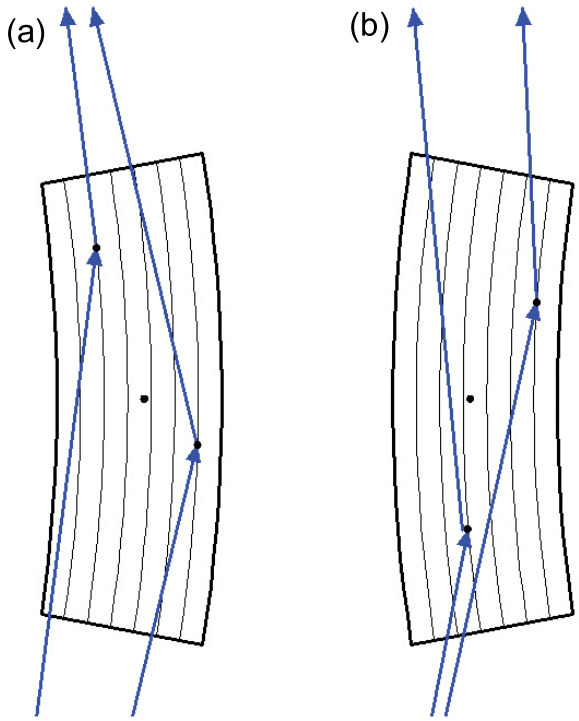

Figure B.4: Sketch of diffraction occurring in CDP crystal with photons imping on concave (a) and convex (b) diffracting planes.

rewrite equation (B.2) as

$$x_D = -\Delta\theta(\frac{T_0}{\Omega}\theta_B - L_S) - \Delta\theta^2\frac{T_0}{\Omega}. \tag{B.11}$$

If $R_C = L_S/\theta_B$, it results

$$x_D = -\Delta\theta^2\frac{T_0}{\Omega}. \tag{B.12}$$

Since $\Delta\theta = -z_D/R_C$, if we set $R_{RW} = R_C/2$, we can write

$$x_D = -\frac{z_D^2}{2R_{RW}}, \tag{B.13}$$

which is the equation of a parabola with vertex in the origin (in this case the centre of the crystal) and x_D as symmetry axis. Near the origin, this parabola approximates the circle with radius of curvature R_{RW} passing for the origin. This circle can be recognized to be the *Rowland circle*, namely the circle on which diffraction points have to lie in order to have perfect meridional focusing [16]. Fig. B.5 depicts the situation considered here. The Rowland circle is highlighted.

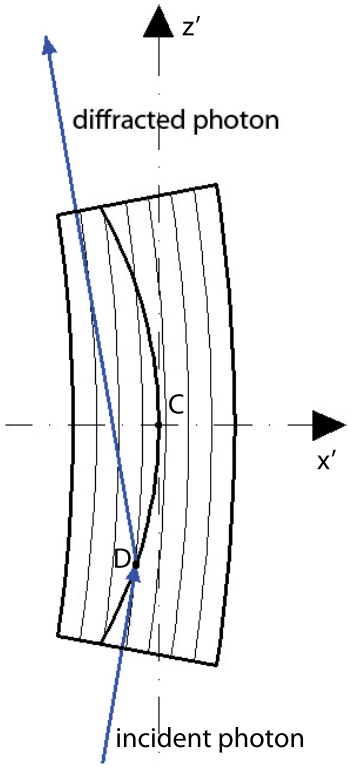

Figure B.5: Diffraction of a photon in a CDP crystal with radius of curvature $R_C = L_S/\theta_B$. The point of diffraction is on a circle with radius of curvature $R_{RW} = R_C/2$ (solid curve).

B.3 Variation of the spacing between the diffracting planes in a CDP crystal

Let us consider the bent crystal depicted in Fig. B.6. The scheme represents a CDP crystal of the type considered in chapters 3 and 4. T_0 is the mean thickness of the crystal traversed by the photon beam and R_C is the radius of curvature of the diffracting planes in Laue geometry. As a consequence of the bending, the crystal is stretched on the convex[2] side and compressed in on the concave side. Through the Poisson's ratio ν, it is possible to calculate the variation of the spacing between the diffracting planes d. It holds

$$\frac{\Delta d}{d} = -\nu \frac{\Delta T_0}{T_0}. \tag{B.14}$$

Being $T_0 = \Omega R_C$ and $\Delta R_C = L_r$, it follows that

$$\frac{\Delta d}{d} = -\nu \frac{L_r}{R_C}. \tag{B.15}$$

[2]The intuitive meaning of the term has to be intended here

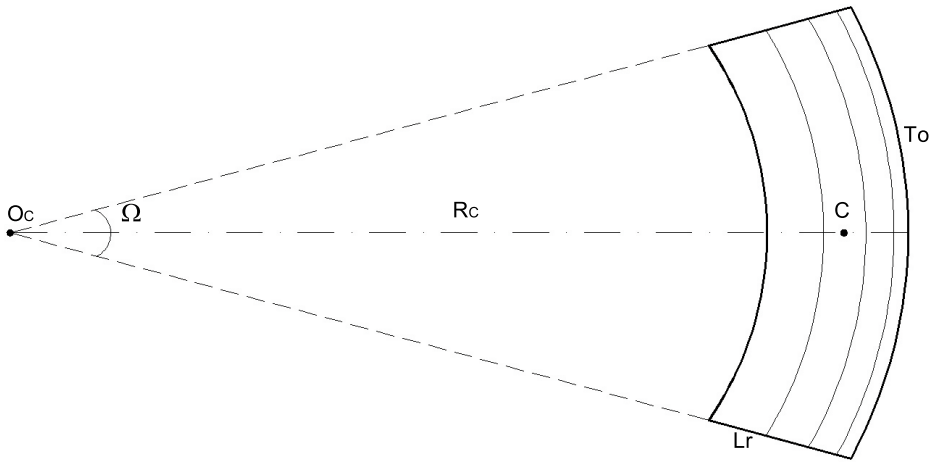

Figure B.6: Variation of the spacing between the diffracting planes in a CDP crystal. L_r is the radial dimension of crystal, Ω the bending angle and $R_C = \overline{O_C C}$ the radius of curvature. In the figure, the variation of the spacing has been exaggerated for better visibility.

Thus, the curvature of the diffracting planes implies a reduction of the crystal spacing on the convex surface and an increment of the crystal spacing on the concave surface.

The variation of the crystal plane spacing potentially increases the angular acceptance for a given photon energy, indeed it causes a variation of the Bragg angle along the thickness of the crystal traversed by the photon beam. Differentiating Bragg's law, we have

$$\frac{\Delta\theta_B}{\theta_B} = -\frac{\Delta d}{d}, \tag{B.16}$$

thus, the total variation of the Bragg angle $\Delta\theta_B$ due the variation of d turns out to be

$$\Delta\theta_B = \nu\theta_B \frac{L_r}{R_C}. \tag{B.17}$$

In the practical cases, this variation is negligible with respect to the spread of the diffracting planes directly due to bending Ω. For example, Let us consider a (111) CDP silicon crystal. Poisson's ratio is about 0.26, while θ_B is about 0.02 rad (1.1°) at 100 keV. If we take typical values for L_r and R_C, $\Delta\theta_B$ turns out to be lower than 0.2 arcsec, thus it is even lower than the Darwin width, which is 0.5 arcsec in this case. For this reason, the variation of the crystal plane spacing has not been taken into account in this thesis.

Bibliography

[1] WHO. http://www.who.int/mediacentre/factsheets/fs297/en, 2015.

[2] J.L. Viney. Transgenic and gene knockout mice in cancer research. *Cancer and Metastasis Reviews*, 14(2):77–90, 1995.

[3] F. P. Jansen and Jean-Luc. Vanderheyden. The future of SPECT in a time of PET. *Nuclear Medicine and Biology*, 34:733–735, 2007.

[4] A. Authier. *Dynamical Theory of X-Ray Diffraction*. Oxford University Press, 2001.

[5] M. J. Pivovaroff, W. B. Barber, F. E. Christensen, W. W. Craig, T. Decker, M. Epstein, T. Funk, C. J. Hailey, B. H. Hasegawa, R. Hill, J. G. Jernigan, C. Taylor, and K. P. Ziock. Small-animal radionuclide imaging with focusing gamma-ray optics. *Proc. SPIE*, 5199:147–161, 2004.

[6] M. J. Pivovaroff, T. Funk, W. C. Barber, B. D. Ramsay, and B. H. Hasegawa. Progress of focusing x-ray and gamma-ray optics for small animal imaging. *Proc. SPIE*, 5923, 2005.

[7] R. K. Smither. New method for focusing x rays and gamma rays. *Rev. Sci. Instrum.*, 53:131, 1982.

[8] H. Owen, D. Holder, J. Alonso, and R. Mackay. Technologies for delivery of proton and ion beams for radiotherapy. *Int. J. Mod. Phys. A*, 29:1441002, 2014.

[9] W. H. Zachariasen. *Theory of X-ray diffraction in crystals*. J. Wiley and sons, inc., 1945.

[10] C. G. Darwin. The theory of x-ray reflection. *Philosophical Magazine Series 6*, 27(158):315–333, 1914.

[11] C. G. Darwin. The theory of x-ray reflection. part II. *Philosophical Magazine Series 6*, 27(160):675–690, 1914.

[12] A. Authier and C. Malgrange. Diffraction physics. *Acta Crystallogr.*, A54:806–819, 1998.

[13] A. Authier. Dynamical theory of x-ray diffraction. *International Tables for Crystallography*, B(5.1):534–551, 2006.

[14] B. W. Batterman and H. Cole. Dynamical diffraction of x rays by perfect crystals. *Rev. Mod. Phys.*, 36(3):681–717, 1964.

[15] H. Halloin and P. Bastie. Laue diffraction lenses for astrophysics: Theoretical concepts. *Exp. Astron.*, 20:151–170, 2005.

[16] R. K. Smither. Development of crystal lenses for energetic photons. *Rev. Sci. Instrum.*, 85:081101, 2014.

[17] R. K. Smither and D. E. Roa. Crystal diffraction lens for medical imaging. *Proc. SPIE*, 3977, 2000.

[18] D. Roa, R. Smither, X. Zhang, K. Nie, Y. Shieh, N. Ramsinghani, N. Milne, J. Kuo, J. Redpath, M. Al-Ghazi, and P. Caligiuri. Development of a new photon diffraction imaging system for diagnostic nuclear medicine. *Exp. Astron.*, 20:229–239, 2005.

[19] V. Carassiti, P. Dalpiaz, V. Guidi, A. Mazzolari, and M. Melchiorri. Note: Rigid holder to host and bend a crystal for multiple volume reflection of a particle beam. *Rev. Sci. Instrum.*, 81:066106, 2010.

[20] C. Schulze, U. Lienert, M. Hanfland, M. Lorenzen, and F. Zontone. Microfocusing of hard x-rays with cylindrically bent crystal monochromators. *J. Synchrotron Rad.*, 5:77–81, 1998.

[21] P. Suortti, U. Lienert, and C. Schulze. Bent crystal optics for high energy synchrotron radiation. *AIP Conf. Proc.*, 389:175–192, 1997.

[22] S. Takagi. A dynamical theory of diffraction for a distorted crystal. *J. Phys. Soc. Jpn.*, 26:1239–1253, 1969.

[23] D. Taupin. Theorie dynamique de la diffraction des rayons x par les cristaux deformes. *Bull. Soc. Fr. Miner. Crist*, 87, 1964.

[24] P. Penning and D. Polder. Anomalous transmission of X-rays in elastically deformed crystals. *Philips Res. Rep.*, 16:419–440, 1961.

[25] N. Kato. Pendellosung fringes in distorted crystals I. fermat's principle for Bloch waves. *J. Phys. Soc. Jpn.*, 18:1785–1791, 1963.

[26] C. Malgrange. X-ray propagation in distorted crystals: From dynamical to kinematical theory. *Cryst. Res. and Tech.*, 37:654–662, 2002.

[27] A. Boeuf, S. Lagomarsino, S. Mazkedian, S. Melone, P. Puliti, and F. Rustichelli. X-ray diffraction characteristics of curved monochromators for synchrotron radiation. *J. Appl. Crystallogr.*, 11(5):442–449, Oct 1978.

[28] V. Bellucci, R. Camattari, I. Neri, and V. Guidi. Calculation of diffraction efficiency for curved crystals with arbitrary curvature radius. *J. Appl. Crystallogr.*, 46:415–420, 2013.

[29] E. Virgilli, F. Frontera, V. Valsan, V. Liccardo, V. Carassiti, S. Squerzanti, M. Statera, M. Parise, S. Chiozzi, F. Evangelisti, E. Caroli, J. B. Stephen, N. Auricchio, S. Silvestri, A. Basili, F. Cassese, L. Recanatesi, V. Guidi, V. Bellucci, R. Camattari, C. Ferrari, A. Zappettini, E. Buffagni, E. Bonnini, M. Pecora, S. Mottini, and B. Negri. The LAUE project and its main results. *Proc. SPIE*, 8861:886107–886107–17, 2013.

[30] P. Mikula, E. Krüger, R. Scherm, and V. Wagner. Elastically bent silicon crystal as a monochromator for thermal neutrons. *J. Appl. Crystallogr.*, 23:105–110, 1990.

[31] E. N. Tsyganov. Some aspects of the mechanism of a charge particle penetration through a monocrystal. Technical report, Fermilab, 1976. Preprint TM-682.

[32] A. M. Taratin and S. A. Vorobiev. Volume reflection of high-energy charged particles in quasi-channeling states in bent crystals. *Phys. Lett. A*, 119(8):425 – 428, 1987.

[33] W. Scandale, G. Arduini, R. Assmann, R. Losito, G. Cavoto, Yu-M. Ivanov, G. Hall, T. Markiewicz, A-M. Taratin, and Yu-A. Chesnokov. LHC collimation with bent crystals - LUA9. Technical Report CERN-LHCC-2011-007. LHCC-I-019, CERN, Geneva, Jun 2011.

[34] A.F. Elishev, N.A. Filatova, V.M. Golovatyuk, I.M. Ivanchenko, R.B. Kadyrov, N.N. Karpenko, V.V. Korenkov, T.S. Nigmanov, V.D. Riabtsov, M.D. Shafranov, B. Sitar, A.E. Senner, B.M. Starchenko, V.A. Sutulin, I.A. Tyapkin, E.N. Tsyganov, D.V. Uralsky, A.S. Vodopianov, A. Forycki, Z. Guzik, J. Wojtkowska, R. Zelazny, I.A. Grishaev, G.D. Kovalenko, B.I. Shramenko, M.D. Bavizhev, N.K. Bulgakov, V.V.

Avdeichikov, R.A. Carrigan Jr., T.E. Toohig, W.M. Gibson, I.J. Kim, J. Phelps, and C.R. Sun. Steering of charged particle trajectories by a bent crystal. *Physics Letters B*, 88(3-4):387 – 391, 1979.

[35] A. G. Afonin, V. T. Baranov, V. M. Biryukov, M. B. H. Breese, V. N. Chepegin, Yu. A. Chesnokov, V. Guidi, Yu. M. Ivanov, V. I. Kotov, G. Martinelli, W. Scandale, M. Stefancich, V. I. Terekhov, D. Trbojevic, E. F. Troyanov, and D. Vincenzi. High-efficiency beam extraction and collimation using channeling in very short bent crystals. *Phys. Rev. Lett.*, 87:094802, 2001.

[36] A. V. Korol, A. V. Solov'yov, and W. Greiner. Channeling of positrons through periodically bent crystals: on feasibility of crystalline undulator and gamma-laser. *Int. J. Mod Phys E*, 13(05):867–916, 2004.

[37] H. Kawata, M. Sato, and Y. Higashi. Improvements on water-cooled and doubly bent crystal monochromator for Compton scattering experiments. *Nucl. Instrum. Meth. A*, 467-468, Part 1:404–408, 2001.

[38] R. K. Smither, K. A. Saleem, D. E. Roa, M. A. Beno, P. V. Ballmoos, and G. K. Skinner. High diffraction efficiency, broadband, diffraction crystals for use in crystal diffraction lenses. *Exp. Astron.*, 20:201–210, 2005.

[39] S. Keitel, C. Malgrange, T. Niemöller, and J. R. Schneider. Diffraction of 100 to 200 keV x-rays from an $Si_{1-x}Ge_x$ gradient crystal: comparison with results from dynamical theory. *Acta Crystallogr. A*, A55:855–863, 1999.

[40] C. Ferrari, E. Buffagni, E. Bonnini, and D. Korytar. High diffraction efficiency in crystals curved by surface damage. *J. Appl. Crystallogr.*, 46:1576–1581, 2013.

[41] V. Bellucci, R. Camattari, V. Guidi, and A. Mazzolari. Bending of silicon plate crystals through superficial grooving: modeling and experimentation. *Thin Solid Films*, 520:1069–1073, 2011.

[42] R. Camattari, V. Guidi, V. Bellucci, and A. Mazzolari. Quasi-mosaic effect in crystals and its applications in modern physics. *J. Appl. Crystallogr.*, 2015.

[43] R. Camattari. Curved crystals as optical elements for focusing X- and γ-rays in a Laue lens, 2013. Ph.D. thesis.

[44] O.I. Sumbaev. Experimental investigation of the elastic qausi-mosaic effect. *Soviet Phys. JETP*, 5:724–728, 1968.

[45] V. Guidi, V. Bellucci, R. Camattari, and I. Neri. Proposal for a Laue lens with quasi-mosaic crystalline tiles. *J. Appl. Crystallogr.*, 44:1255–1258, 2011.

[46] R. Camattari, G. Paternò, Bellucci, and V. Guidi. Quasi-mosaicity of (311) planes in silicon and its usage in a high-focusing Laue lens. *Exp. Astron.*, 38:417–431, 2014.

[47] R. Camattari, E. Dolcini, V. Bellucci, A Mazzolari, and V. Guidi. High diffraction efficiency with hard x-rays through a thick silicon crystal bent by carbon fiber deposition. *J. Appl. Crystallogr.*, 47:1762–1764, 2014.

[48] S. Mader and J. F. Ziegler. *Ion Implantation Science and Technology.* Academic Press, New York, NY 109, 1984.

[49] P. J. Burnett and T. F. Page. An investigation of ion implantation-induced near-surface stresses and their effects in sapphire and glass. *J. Mat. Sci.*, 20:4624–4646, 1985.

[50] M. Itoh and M. Hori. An ultra-low stress tungsten absorber for x-ray masks. *J. Vac. Sci. Technol. B*, 9:165–168, 1991.

[51] B. Chalifoux, E. Sung, R. K. Heilmann, and M. L. Schattenburg. High-precision figure correction of x-ray telescope optics using ion implantation. *Optics for EUV, X-Ray, and Gamma-Ray Astronomy VI*, 8861:88610T, 2013.

[52] T.G. Bifano, H.T. Johnson, P. Bierden, and R.K. Mali. Elimination of stress-induced curvature in thin film structures. *J. Microelectromechanical Sys.*, 11:592–597, 2002.

[53] S. M. Sze. *Semiconductor Devices: Physics and Technology, 2nd edition.* Wiley, 2002.

[54] J. F. Ziegler, M. D. Ziegler, and J. P. Biersack. SRIM - the stopping and range of ions in matter. *Nucl. Instrum. Meth. B*, 268(11-12):1818 – 1823, 2010.

[55] J. Lilley, editor. *Nuclear Physics: Principles and Applications.* Wiley, 2001.

[56] F. L. Vook. Low-temperature length change measurements of electron-irradiated germanium and silicon. *Phys. Rev.*, 125:855–861, 1962.

[57] S. Tamulevicius, I. Pozela, and J. Jankauskas. Integral stress in ion-implanted silicon. *J. Phys. D: Appl. Phys.*, 31:2991, 1998.

[58] R. Lang, A. de Menezes, A. dos Santos, S. Reboh, E. Meneses, L. Amaral, and L. Cardoso. *Ion-Beam-Induced Epitaxial Recrystallization Method and Its Recent Applications*, volume 14. InTech, 2012.

[59] G.C.A.M. Janssen, F. Abdalla, M.M.and van Keulen, B.R. Pujada, and B. van Venrooy. Celebrating the 100th anniversary of the stoney equation for film stress: Developments from polycrystalline steel strips to single crystal silicon wafers. *Thin Solid Films*, 517(6):1858 – 1867, 2009.

[60] Straus7. Release 2.3.3 - 2004. http://www.straus7.com.

[61] R. Camattari, L. Lanzoni, V. Bellucci, and V. Guidi. Computer program for calculation of elastic properties in silicon and germanium crystals. *J. Appl. Crystallogr.*, 48:943–949, 2015.

[62] V. Bellucci, G. Paternò, R. Camattari, V. Guidi, M. Jentschel, and P. Bastie. High-efficiency diffraction and focusing of X-rays through asymmetric bent crystalline planes. *J. Appl. Crystallogr.*, 48:297–300, 2015.

[63] V. Bellucci, R. Camattari, A. Mazzolari, G. Paternò, V. Guidi, C. Scian, G. Mattei, and L. Lanzoni. Ion implantation for manufacturing bent and periodically bent crystals. *Applied Physics Letters*, 107(6), 2015.

[64] S. Bellucci, S. Bini, V. M. Biryukov, Yu. A. Chesnokov, S. Dadagov, G. Giannini, V. Guidi, Yu. M. Ivanov, V. I. Kotov, V. A. Maisheev, C. Malagù, G. Martinelli, A. A. Petrunin, V. V. Skorobogatov, M. Stefancich, and D. Vincenzi. Experimental study for the feasibility of a crystalline undulator. *Phys. Rev. Lett.*, 90:034801, 2003.

[65] R. Camattari, V. Guidi, L. Lanzoni, and I. Neri. Experimental analysis and modeling of self-standing curved crystals for focusing of x-rays. *Meccanica*, 48:1875–1882, 2013.

[66] S. G. Lekhnitskii, S. W. Tsai, and T. Cheron. *Anisotropic Plates*. Gordon and Breach Science Publishers, 1956.

[67] Y. Gogotsi, C. Baek, and F. Kirscht. Raman microspectroscopy study of processing-induced phase transformations and residual stress in silicon. *Semicond. Sci. Technol.*, 14:936, 1999.

[68] N. Barrière, V. Guidi, V. Bellucci, R. Camattari, T. Buslaps, J. Rousselle, G. Roudil, F.X. Arnaud, P. Bastie, and L. Natalucci. High diffraction efficiency at hard X-ray energy in a silicon crystal bent by indentation. *J. Appl. Crystallogr.*, 43:1519–1521, Dec 2010.

[69] V. Bellucci, R. Camattari, V. Guidi, I. Neri, and N. Barrière. Self-standing bent silicon crystals for very high efficiency Laue lens. *Exp. Astron.*, 31:45–58, 2011.

[70] A. Guinier and J. Tennevin. Sur deux variantes de la methode de Laue et leurs applications. *Acta Crystallogr.*, 2:133–138, 1949.

[71] B. Hamelin and P. Bastie. High-energy focusing Laue method: Recent developments. *J. Phys. IV.*, 8:3–8, 1998.

[72] M. Stockmeier and A. Magerl. A focusing Laue diffractometer for the investigation of bulk crystals. *J. Appl. Crystallogr.*, 41:754–760, 2008.

[73] I. Neri, R. Camattari, V. Bellucci, V. Guidi, and P. Bastie. Ordered stacking of crystals with adjustable curvatures for hard x- and gamma-ray broadband focusing. *J. Appl. Crystallogr.*, 46:953–959, 2013.

[74] V. Guidi, V. Bellucci, R. Camattari, and I. Neri. Curved crystals for high-resolution focusing of x and gamma rays through a Laue lens. *Nucl. Instrum. Meth. B*, 309:249–253, 2013.

[75] J. T. Bushberg, J. A. Seibert, E. M. JR. Leidholdt, and J. M. Boone. *The Essential Physics of Medical Imaging.* Lippincott Williams & Wilkins, 2002.

[76] A. Rahmim and H. Zaidi. PET versus SPECT: strengths, limitations and challenges. *Nuclear Medicine Communications*, 29:193–207, 2008.

[77] F. Beekman and F. van der Have. The pinhole: gateway to ultra-high-resolution three-dimensional radionuclide imaging. *Eur. J. Nucl. Med. Mol. Imaging*, 34(2):151–161, 2007.

[78] N.U. Schramm, G. Ebel, U. Engeland, T. Schurrat, M. Behe, and T.M. Behr. High-resolution SPECT using multipinhole collimation. *Nuclear Science, IEEE Transactions on*, 50(3):315–320, June 2003.

[79] F. J. Beekman, F. van der Have, B. Vastenhouw, A. J. van der Linden, P. P. van Rijk, J. P. H. Burbach, and M. P. Smidt. U-SPECT-I: a novel system for submillimeter-resolution tomography with radiolabeled molecules in mice. *The Journal of Nuclear Medicine*, 46(7):1194–1200, July 2005.

[80] N. Lund. A study of focusing telescopes for soft gamma rays. *Exp. Astron.*, 2:259–273, 1992.

[81] F. Frontera and P. Von Ballmoos. Laue gamma-ray lenses for space astrophysics:status and prospects. *X-Ray Optics and Instrumentation*, 2010:215375, 2010.

[82] V. Bellucci, R. Camattari, and V. Guidi. Proposal for a Laue lens relying on hybrid quasi-mosaic curved crystals. *Astron. and Astrophys.*, 560:8, 2013.

[83] R. K. Smither, P. B. Fernandez, T. Graber, P. von Ballmoos, J. Naya, F. Albernhe, G. Vedrenne, and M. Faiz. Review of crystal diffraction and its application to focusing energetic gamma rays. *Exp. Astron.*, 6:47–56, 1995.

[84] S. Webb. *The Physics of Medical Imaging.* Taylor & Francis, 1988.

[85] H. Halloin. Laue diffraction lenses for astrophysics: From theory to experiments. *Exp. Astron.*, 20:171–184, 2005.

[86] MATLAB. *version 8.6 (R2015b).* The MathWorks Inc., Natick, Massachusetts, 2015.

[87] E. Caroli, N. Auricchio, L. Amati, Y. Bezsmolnyy, C. Budtz-jorgensen, R. M. Curado da Silva, F. Frontera, A. Pisa, S. Del sordo, J. B. Stephen, and G. Ventura. A focal plane detector design for a wide-band Laue-lens telescope. *Exp. Astron.*, 20:341–351, 2005.

[88] E. Caroli, N. Auricchio, S. Del Sordo, L. Abbene, C. Budtz-Jorgensen, F. Casini, R. M. Curado da Silva, I. Kuvvetlli, L. Milano, L. Natalucci, E. M. Quadrini, J. B. Stephen, P. Ubertini, M. Zanichelli, and A. Zappettini. Development of a 3D CZT detector prototype for Laue lens telescope. *Proc. SPIE*, 7742:77420V–77420V–9, 2010.

[89] S. Del Sordo, L. Abbene, E. Caroli, J. B. Stephen, e. Quadrini, L. Natalucci, P. Ubertini, and A. Zappettini. Hard X-Ray CZT detector development and testing on stratospheric balloon payloads, 2009.

[90] M. Khalil, F. Frontera, E. Caroli, E. Virgilli, and V. Valsan. A simulation study on the focal plane detector of the LAUE project. *Nuclear Instruments and Methods in Physics Research Section A: Accelerators, Spectrometers, Detectors and Associated Equipment*, 786:59–70, 2015.

[91] NIST. http://www.nist.gov/pml/data/xraycoef/index.cfm, 2015.

[92] N. Barrière, S. E. Tomsick, J. A.and Boggs, A. Lowell, C. Wade, M. Baugh, P. von Ballmoos, N. V. Abrosimov, and L. Hanlon. Developing a method for soft gamma-ray Laue lens assembly and calibration. *Nuclear Instruments and Methods in Physics Research Section A: Accelerators, Spectrometers, Detectors and Associated Equipment*, 741:47 – 56, 2014.

[93] E. Virgilli, F. Frontera, P. Rosati, V. Liccardo, S. Squerzanti, V. Carassiti, E. Caroli, N. Auricchio, and J. B. Stephen. Hard x-ray broad band Laue lenses (80-600 keV): building methods and performances. *Proc. SPIE*, 9603:960308–960308–9, 2015.

[94] G. Dougherty. *Digital Image Processing for Medical Applications*. Cambridge University Press, 2009.

[95] A. Rose. *Vision: Human and Electronic*. Plenum Press, 1973.

[96] F. M. Khan, editor. *The Physics of Radiation Therapy*. Lippincott Williams & Wilki, 1987.

[97] P. Mayles, A. Nahum, and J. C. Rosenwald, editors. *Handbook of Radiotherapy Physics - Theory and Practice*. Taylor & Francis, 2007.

[98] PTCOG. http://www.ptcog.ch/index.php/facilities-in-operation, 2016.

[99] E. B. Podgorsak. *Radiation Oncology Physics: A Handbook for Teachers and Students*. IAEA, 2005.

[100] F. H. Attix. *Introduction to radiological physics and radiation dosimetry*. Wiley-Vch, 1987.

[101] R. F. Saavedra and M. Valente. Convergent photon and electron beam generator device, 2014. US Patent App. 14/112,429.

[102] R. G. Figueroa and M. Valente. Feasibility and dosimetric characterization of single convergent beam teletherapy RTHC. *Physica Medica*, 30:e73, 2014.

[103] R. G. Figueroa and M. Valente. Physical characterization of single convergent beam device for teletherapy: theoretical and monte carlo approach. *Physics in Medicine and Biology*, 60(18):7191, 2015.

[104] Dip. N. Mahato and C. A. MacDonald. Potential for focused beam orthovoltage therapy. *Proc. SPIE*, 7806:78060F–78060F–7, 2010.

[105] H. Abbas, Dip N. Mahato, J. Satti, and MacDonald C. A. Measurements and simulations of focused beam for orthovoltage therapy. *Medical Physics*, 41:041702, 2014.

[106] C. A. MacDonald. Focusing polycapillary optics and their applications. *X-Ray Optics and Instrumentation*, 2010:867049, 2010.

[107] L.A. Medina, B.I. Herrera-Penilla, M.A. Castro-Morales, P. Garcia-Lopez, R. Jurado, E. Perez-Cardenas, J. Chanona-Vilchis, and M.E. Brandan. Use of an orthovoltage x-ray treatment unit as a radiation research system in a small-animal cancer model. *Journal of Experimental & Clinical Cancer Research*, 27(1), 2008.

[108] Z. Burshtein, A. Bar-David, and Z. Harel. System for x-ray irradiation of target volume, 2013. US Patent App. 13/817,562.

[109] P. Arce, J. I. Lagares, L. Harkness, D. Perez-Astudillo, M. Canadas, P. Rato, M. De Prado, Y. Abreu, G. De Lorenzo, M. Kolstein, and A. Diaz. Gamos: A framework to do Geant4 simulations in different physics fields with an user-friendly interface. *Nuclear Instruments and Methods in Physics Research Section A: Accelerators, Spectrometers, Detectors and Associated Equipment*, 735(0):304 – 313, 2014.

[110] S. Agostinelli, J. Allison, K. Amako, J. Apostolakis, H. Araujo, P. Arce, M. Asai, D. Axen, S. Banerjee, G. Barrand, F. Behner, L. Bellagamba, J. Boudreau, L. Broglia, A. Brunengo, H. Burkhardt, S. Chauvie, J. Chuma, R. Chytracek, G. Cooperman, G. Cosmo, P. Degtyarenko, A. Dell'Acqua, G. Depaola, D. Dietrich, R. Enami, A. Feliciello, C. Ferguson, H. Fesefeldt, G. Folger, F. Foppiano, A. Forti, S. Garelli, S. Giani, R. Giannitrapani, D. Gibin, J.J. Gomez Cadenas, I. Gonzalez, G. Gracia Abril, G. Greeniaus, W. Greiner, V. Grichine, A. Grossheim, S. Guatelli, P. Gumplinger, R. Hamatsu, K. Hashimoto, H. Hasui, A. Heikkinen, A. Howard, V. Ivanchenko, A. Johnson, F.W. Jones, J. Kallenbach, N. Kanaya, M. Kawabata, Y. Kawabata, M. Kawaguti, S. Kelner, P. Kent, A. Kimura, T. Kodama, R. Kokoulin, M. Kossov, H. Kurashige, E. Lamanna, T. Lampen, V. Lara, V. Lefebure, F. Lei, M. Liendl, W. Lockman, F. Longo, S. Magni, M. Maire, E. Medernach, K. Minamimoto, P. Mora de Freitas, Y. Morita, K. Murakami, M. Nagamatu, R. Nartallo, P. Nieminen, T. Nishimura, K. Ohtsubo, M. Okamura, S. O'Neale, Y. Oohata, K. Paech, J. Perl, A. Pfeiffer, M.G. Pia, F. Ranjard, A. Rybin, S. Sadilov, E. Di Salvo, G. Santin, T. Sasaki, N. Savvas, Y. Sawada, S. Scherer, S. Sei, V. Sirotenko, D. Smith, N. Starkov, H. Stoecker, J. Sulkimo, M. Takahata, S. Tanaka, E. Tcherniaev, E. Safai Tehrani, M. Tropeano, P. Truscott, H. Uno, L. Urban, P. Urban, M. Verderi, A. Walkden, W. Wander, H. Weber, J.P. Wellisch, T. Wenaus, D.C. Williams, D. Wright, T. Yamada, H. Yoshida, and D. Zschiesche. Geant4 - a simulation toolkit. *Nuclear Instruments and Methods in Physics Research Section A: Accelerators, Spectrometers, Detectors and Associated Equipment*, 506(3):250 – 303, 2003.

[111] N. Barrière, J. Rousselle, P. von Ballmoos, N. V. Abrosimov, P. Courtois, P. Bastie, T. Camus, M. Jentschel, V. N. Kurlov, L. Natalucci, G. Roudil, N. Frisch Brejnholt, and D. Serre. Experimental and theoretical study of the diffraction properties of various crystals for the realization of a soft gamma-ray Laue lens. *J. of App. Cryst.*, 42(5):834–845, 2009.

[112] G. G. Poludniowski, G. Landry, F. DeBlois, Evans P. M., and F. Verhaegen. Spekcalc: a program to calculate photon spectra from tungsten anode x-ray tubes. *Phys. Med. Biol.*, 54:N433, 2009.

[113] J. Allison, K. Amako, J. Apostolakis, H. Araujo, P.A. Dubois, M. Asai, G. Barrand, R. Capra, S. Chauvie, R. Chytracek, G.A.P. Cirrone, G. Cooperman, G. Cosmo, G. Cuttone, G.G. Daquino, M. Donszelmann, M. Dressel, G. Folger, F. Foppiano, J. Generowicz, V. Grichine, S. Guatelli, P. Gumplinger, A. Heikkinen, I. Hrivnacova, A. Howard, S. Incerti, V. Ivanchenko, T. Johnson, F. Jones, T. Koi, R. Kokoulin, M. Kossov, H. Kurashige, V. Lara, S. Larsson, F. Lei, O. Link, F. Longo, M. Maire, A. Mantero, B. Mascialino, I. McLaren, P.M. Lorenzo, K. Minamimoto, K. Murakami, P. Nieminen, L. Pandola, S. Parlati, L. Peralta, J. Perl, A. Pfeiffer, M.G. Pia, A. Ribon, P. Rodrigues, G. Russo, S. Sadilov, G. Santin, T. Sasaki, D. Smith, N. Starkov, S. Tanaka, E. Tcherniaev, B. Tome, A. Trindade, P. Truscott, L. Urban, M. Verderi, A. Walkden, J.P. Wellisch, D.C. Williams, D. Wright, and H. Yoshida. Geant4 developments and applications. *Nuclear Science, IEEE Transactions on*, 53(1):270–278, Feb 2006.

[114] J. Baro, J. Sempau, J. M. Fernandez-Varea, and F. Salvat. Penelope: An algorithm for monte carlo simulation of the penetration and energy loss of electrons and positrons in matter. *Nucl. Instrum. Meth. B*, 100:31–46, 1995.

[115] J. Sempau, E. Acosta, J. Baro, J. M. Fernandez-Varea, and F. Salvat. An algorithm for monte carlo simulation of coupled electron-photon transport. *Nucl. Instrum. Meth. B*, 132:377–390, 1997.

[116] Yu. V. Milman, I. V. Gridneva, and A. A. Golubenko. Construction of stess-strain curves for brittle materials by indentation in a wide temperature range. *Science of Sintering*, 39:67–75, 2007.

[117] S. G. Lekhnitskii. *Theory of elasticity of an anisotropic body*. Mir Publishers, Moscow, 1981.

[118] L. Lanzoni, A. Mazzolari, V. Guidi, A. Tralli, and G. Martinelli. On the mechanical behaviour of a crystalline undulator. *Int. J. Eng. Sci.*, 46:917–928, 2008.

Acknowledgments

I am grateful to Emilia-Romagna region and INFN for financial support through the SPINNER and LOGOS project respectively.

Moreover, I would like to thank professor Vincenzo Guidi for his scientific guide and all my friend and colleagues at Physics and Earth Science Department of Ferrara for making me feel at home.